Novel Amorphous Iron-Dysprosium-Terbium-Oxide Thin Films: Synthesis, Properties, and Application

A Dissertation Presented for the

Doctor of Philosophy

Degree

The University of Tennessee, Knoxville

Humaira Taz

May 2018

Dedicated to my parents Sk. Md. Nurtaz Ali and Shadhina Khatun.

Acknowledgments

First and foremost, I would like to thank my advisors Dr. Ramki Kalyanaraman and Dr. Gerd Duscher. This thesis would not have been possible without Dr. Ramki's constant support and Dr. Duscher's critical eye. It was a pleasure working under the supervision of Dr. Ramki for the last five years. He was always willing to listen with an open mind to ideas and suggestions that helped me develop confidence in my research skills. His guidance has been phenomenal even when he was not available on-site. Thanks to Dr. Ramki, I was able to form invaluable collaborations and friendships at the University of California-Berkeley during my stay there for a year. I am grateful to Dr. Duscher for his mentorship and immense help with TEM measurements and their analysis.

I would also like to thank my other committee members Dr. Jagjit Nanda and Dr. Syed K. Islam. I am very grateful to both of them for their time, commitment, and critiques and suggestions to my thesis; and especially thankful to Dr. Jagjit Nanda for sponsoring me at Oak Ridge National Lab for the first four years of my graduate program.

This brings me to all the people I have collaborated with at various institutions who have helped me accomplish my research goals. I am thankful to Dr. Ramamoorthy Ramesh and Dr. Lane Martin at the University of California-Berkeley for letting me work with their group there for a year, and for providing valuable insight on my work. I would like to express my gratitude to all the people I worked with at UC-Berkeley: Dr. Bhagwati Prasad, Dr. Nikita Gaur, Dr. Zuhuang Chen, Dr. Jeremy Turcaud, Dr. Vishal Thakare, Dr. Yen-Lin Huang, Dr. Chalres-Henri Lambert, Dr. Anoop Damodaran, Dr. Ajay Yadav, Dr. Sujit Das, Liv Dedon, Margaret McCarter, Shang-Lin Hsu, Joshua Douglas, Ruijuan Xu, Sahar Saremi, Gabriel Velarde, Eduardo Lupi, Ran Gao, and Shishir Pandya. Special thanks to Dr. Bhagwati Prasad for always being so optimistic about my thesis material, helping me design experiments, measurements, and analyze data. A second special thanks to Dr. Nikita Gaur for not only helping with lab work, but also being a good friend in a new city. In addition, I would like to mention each of my collaborators all over the US for their cooperation in this journey:

- Dr. Tamil Sakthivel and Dr. Sudipta Seal at the University of Central Florida
- Dr. Ashutosh Tiwari and Kun Tian at the University of Utah
- Dr. Hernando Garcia at the Southern Illinois University-Edwardsville
- Dr. Tatiana Allen and her students at the University of Tennessee-Chattanooga

- Jonas Kapraun, Mark Hettick, Dr. James Bullock, and Dr. Ali Javey at the University of California-Berkeley
- Dr. Dhananjay Kumar and his group at the North Calorina A&T University
- Dr. Rose Ruther and Dr. Michael Naguib at Oak Ridge National Lab

My work in Knoxville was made easier with help from my past and present labmates, who were always there as friends and colleagues. I would like to thank Abhinav Malasi, Sagar Yadavali, Prasad Sandireddy, Krishna Koirala, Chenze Liu, Annette Farah, Jingxuan Ge, Mikayla Ehrsam, Michelle Lames, and Connor Carr. I would like to especially thank John Dunlap for training me on the instruments at SERF and JIAM, and always helping out with a smile. I would also like to acknowledge the support and welcome I received from the administrative folks at the Bredesen Center (Wanda Davis, Tracey Bucher, Erin Favier, and Jessica Garner), at the Materials Science and Engineering Department (Carla Lawrence, Tony Brewer, Frank Holiway and Randy Stooksbury), and at the Department of Chemical and Biomolecular Engineering (Rita Gray and Amber Tipton).

My experience in Knoxville was made more pleasant by all my friends: Katie who was my constant coffee-buddy; Nina who was a precious roommate and friend; Emilio and Akinola. This list would be incomplete without mentioning the Bangladeshi community in Knoxville, especially the families who have fed me and checked on me from time to time as if I were a member of their family.

Finally, I would like to thank my family for always supporting me through the hard and easy times, even when they were on the other side of the world. My parents' encouragement and spirits gave me all the motivation I needed to finish this journey. I am extremely grateful to my mother for her selfless love and care, and to my father for his hard work - they are the reason I am who I am today. I cannot forget the role my siblings played in this journey. My younger sister and brother were always there for me to offer laughter, comfort and joy to my life.

Lastly, I cannot thank enough the man who has been through everything with me - my husband. Even though he has been miles and miles away across the border in Canada throughout my entire grad school journey, he brought color, cheers and happiness to my life during some of the toughest times.

Of course, above all, I thank and praise God for blessing me with everything in my life, and carrying me through all forms of hardship.

Abstract

Amorphous oxides which are transparent and conducting find use in display devices and as top electrodes in energy applications, while those which are conducting and magnetic have the potential to be used in spintronics. With the fast approaching limit of Moore's law, new materials are needed where the spin and polarization of the electrons are coupled. Despite progress in transparent conductors, materials selection is limited by the need to have wide optical bandgap and conduction via s-orbital. In contrast, search for new spintronics materials has picked up only in the last decade. Here we report the synthesis, characterization, and application of a new oxide made from Fe, Tb, and Dy - elements that do not conduct via the s-orbital. Thin films (<100 nm) of this oxide were synthesized by pulsed laser deposition (PLD) as a function of varying oxygen pressure, and by electron-beam evaporation as a function of the cation composition, and then annealed under different conditions. Films deposited at $5x10^{-8}$ Torr exhibited high optical transparency (>90%) and conductivity (~10^4 S/m). Films deposited at O_2 pressures below $1x10^{-5}$ Torr were conductive (~10^4 S/m), magnetic (up to 480 emu/cc), and optically transparent, while the ones above $1x10^{-5}$ Torr were optically transparent but insulating and non-magnetic. Changes in the cation stoichiometry showed the films' transition from being metallic to semiconducting with decreasing Fe content relative to the Lanthanides. However, when a very iron-rich film was annealed through several heating and cooling cycles in low vacuum, the film evolved into a semiconductor that was stable in ambient conditions and showed very high conductivity ($2.8x10^5$ S/m) and room temperature magnetism (380 emu/cc). The PLD deposited films were utilized as the ferromagnetic layer for magneto-electric coupling with bismuth ferrite as well as a top electrode for bismuth ferrite capacitors. A giant magneto-resistance (GMR) device made from the Fe-Tb-Dy-oxide and bismuth ferrite showed evidence of magneto-electric coupling at room temperature. The discovery of this oxide not only introduces new materials physics that could be explored and exploited to engineer new multifunctional materials, but the oxide itself proves to be very promising for spintronics device applications.

Table of Contents

1 Introduction **1**

1.1 Motivation . . . 1

1.1.1 Materials with multifunctional properties . . . 1

1.1.2 Applications of multifunctional amorphous oxides (AOx) . . . 3

1.2 Current knowledge and challenges . . . 5

1.2.1 Transparency, conductivity, and magnetism in amorphous oxide semiconductors (AOSs) . . . 5

1.2.1.1 *Band structure and conduction mechanisms in amorphous semiconductors* . . . 5

1.2.1.2 *Hosono's Rule for transparent amorphous oxide semiconductors (TAOS)* . . . 7

1.2.1.3 *Magnetism in amorphous oxides and semiconductors* . . . 9

1.2.1.4 *Oxides of iron, terbium, and dysprosium* . . . 11

1.2.2 Spintronics . . . 12

1.2.2.1 *Magneto-electric (ME) coupling for memory devices* . . . 12

1.3 Goals of thesis . . . 14

2 Methods and techniques **15**

2.1 Synthesis and annealing techniques . . . 15

2.1.1 Substrate selection and preparation . . . 15

2.1.2 Pulsed laser deposition . . . 15

2.1.3 Electron-beam evaporation . . . 18

2.1.4 Capacitors and GMR device fabrication . . . 19

2.1.4.1 *Capacitor fabrication* . . . 19

2.1.4.2 *Giant-magnetoresistance (GMR) device fabrication* . . . 19

2.1.5 Annealing . . . 20

2.1.5.1 *Furnace annealing* . . . 20

2.1.5.2 *Cyclic annealing* . . . 21

2.2 Characterization techniques . . . 22

2.2.1 Physical properties . . . 22

2.2.1.1 *Microstructure & surface morphology* . . . 22

2.2.1.2 *Chemical composition* . . . 23
2.2.2 Optical properties . . . 24
2.2.3 Transport properties . . . 24
2.2.3.1 *Van der Pauw measurements* . . . 24
2.2.3.2 *Low temperature resistance* . . . 25
2.2.3.3 *High temperature resistance and hall mobility* . . . 26
2.2.3.4 *Photoconductivity* . . . 26
2.2.4 Magnetic Properties . . . 26
2.2.4.1 *Superconducting quantum interference device (SQUID)* . . . 26
2.2.4.2 *Magnetoresistance (MR)* . . . 27
2.2.4.3 *Surface magneto-optic Kerr effect (SMOKE)* . . . 28
2.2.5 Ferroelectric hysteresis and fatigue test . . . 28
2.3 Acknowledgments . . . 29

3 Discovery of a novel, amorphous Fe-Dy-Tb-oxide (FDTO) with high optical transparency, conductivity, and mobility 30
3.1 Summary . . . 30
3.2 Methods . . . 30
3.3 Results . . . 31
3.4 Discussion and conclusion . . . 37
3.5 Acknowledgments . . . 38
3.6 Author contributions statement . . . 38

4 Transparent ferromagnetic and semiconducting behavior in Fe- Dy-Tb based amorphous oxide films 39
4.1 Summary . . . 39
4.2 Methods . . . 40
4.3 Results . . . 40
4.4 Discussion and conclusion . . . 46
4.5 Acknowledgments . . . 47
4.6 Author contributions statement . . . 48

5 High conductivity and magnetism in $Fe_{21}Dy_{0.81}Tb_{0.19}$ oxide thin film from cyclic annealing and oxidation 49
5.1 Summary . . . 49
5.2 Methods . . . 49
5.3 Results . . . 50
5.4 Discussion and conclusion . . . 58
5.5 Acknowledgments . . . 59

6 Effect of oxygen growth pressure on transport, magnetism, and optical properties of amorphous $Fe_{0.66}Dy_{0.24}Tb_{0.1}$-oxide **60**
6.1 Summary . . . 60
6.2 Methods . . . 60
6.3 Results . . . 61
6.3.1 Chemical composition and microstructure . . . 61
6.3.2 Transport and magnetism . . . 63
6.3.3 Optical properties and bandgap . . . 67
6.4 Discussion and conclusion . . . 69
6.5 Acknowledgments . . . 69

7 Magneto-electric coupling of FDTO/BFO heterostructures for memory device applications **71**
7.1 Summary . . . 71
7.2 Methods . . . 71
7.3 Results . . . 72
7.3.1 Evidence of magnetic coupling . . . 72
7.3.2 Ferroelectric hysteresis and fatigue of FDTO/BFO capacitors . . . 73
7.3.3 Magneto-electric (ME) coupling in GMR heterostructure . . . 74
7.4 Discussion and conclusion . . . 75
7.5 Acknowledgments . . . 76

8 Conclusions and future work **77**
8.1 Conclusions . . . 77
8.2 Future work . . . 79

Bibliography **81**

Vita **94**

List of Tables

1.1 *Bandgap, resistivity, and magnetic moment of iron, terbium, and dysprosium oxides.* 11

2.1 *List of PLD parameters* 17
2.2 *List of PLD parameters for BFO and SRO* 18

4.1 *Cation composition of the various metals measured by XPS for three Fe:(Tb+Dy) ratios* . . . 42

List of Figures

1.1 *Simplified band structure of metals, insulators, and semiconductors [24]* 2
1.2 *Applications of multifunctional amorphous oxides.* 4
1.3 *(a) Effect of disorder on an s-band [11] (b) Band structure of a typical amorphous material [53] (c) Band structure of n-type a-Si:H [11]* 5
1.4 *(a) Hosono's proposed model showing ns orbital of the heavy metals overlapping with each other while the O-2p orbitals form the valence bands. (b) List of cations proposed by Hosono for synthesizing AOS exhibiting high mobility, conductivity, and optical transparency. (c) Electron effective mass of most cations found by ab initio calculations.* 8
1.5 *(a) Band structure of a-IGZO [30] (b) Earth abundance of elements [65]* 9
1.6 *(a) Mn-doped GeTe showing Curie temperature close to 200 K [69] (b) Curie temperature as a function of Mn-doped GaAs (c) Fe nanoclusters observed in Fe-doped GaN (d) Mn nanoclusters observed in Mn-doped GaN* [68] 10
1.7 *(a) Single phase multiferroic materials [95] (b) Room temperature ME coupling in CoFe/BFO structure [101]* 13

2.1 *Schematic of PLD mechanism* 16
2.2 *(a) Schematic of B-field assisted PLD growth (b) Photo of PLD plume during B-field assisted growth* 18
2.3 *Schematic of co-deposition by e-beam evaporation* 19
2.4 *Schematic of capacitor fabrication* 20
2.5 *(a) Schematic of the FDTO/BFO GMR device cross-section (b) Top view of GMR device* . . . 21
2.6 *Flowchart of one cycle of anneal in 5 mTorr* 21
2.7 *Plot of typical step height measurement in AFM* 22
2.8 *Schematic of phase-sensitive photoconductivity set-up.* 27
2.9 *Schematic showing SMOKE setup* 28

3.1 *(a) SEM image of O_2 -annealed film. (b) Tauc plot analysis for AP films of different thicknesses. (c) AFM surface roughness profile of as-deposited films.* 32

3.2 *(a) Optical photograph showing large optical transparency of 25 nm thick films in as-prepared and annealed states (b) Optical energy dependent transmission of as-prepared and annealed films. (c-d) SEM (c) and AFM (d) information from a 25 nm as-prepared film respectively. (d) Tauc plot showing band gap of as-prepared and annealed films.* 33
3.3 *(a) TEM image and diffraction pattern of as-prepared film. (b-c) EELS analysis of the as-prepared and O_2-annealed films. (d-g) XPS measurements showing the various detected cations in the as-prepared vs O_2-annealed films.* 34
3.4 *(a) XRD of the Terfenol-D target. (b) GIXRD scans of as-prepared, N_2-annealed, and O_2-annealed films of 25 nm thickness. (c) TEM image of O_2-annealed film. (d) XPS survey scan to determine the elements present in the AP and O_2-annealed films.* 35
3.5 *Transport properties of the as-prepared (a-c) and annealed films (d-f).* 36
3.6 *(a) Plot of hall voltage vs magnetic field for 74 nm thick as-prepared film. (b) Kerr rotation measurements of as-prepared and annealed films* 37

4.1 *Plots showing quantified atomic percentages of Fe, Tb, and Dy from five EDS point spectra for (a) R = 0.60, (b) R = 11.9, and (c) R = 21* 40
4.2 *(a) Typical EDS point spectrum of R-0.6 film (b) Plot of atomic percentage of the metals vs R (Fe:Tb+Dy) (c) GIXRD plots for films of different R values* 41
4.3 *XPS plots showing (a, b, c) Fe 2p, and (d, e, f) Tb and Dy 4d for all three R values* 42
4.4 *Plots of (a) metal and cation relative concentrations and (b) the ratio of metal to their cation states and Fe^{3+}/Fe^{2+} ratio* 43
4.5 *XPS plots showing O1s spectra for all three R values* 44
4.6 *(a) XPS spectra showing valence band maxima of all R values (b)Plot of % transmission vs wavelength for all R values* 45
4.7 *Plots of (a) resistivity and (b) mobility and carrier concentration as a function of R values* . 46
4.8 *(a) Plot of magnetic moment as a function of magnetic field for all three R values (b) Plot of coercivity as a function of R values (c) Plot of SMOKE measurement for all the R values* . . 46

5.1 *(a)-(e) HR-TEM cross-section and diffraction patterns of R21-oxide on the SiO_2/Si substrate. (f) GIXRD of R21-oxide.* 52
5.2 *(a) - (c) Z-contrast image of R21-oxide film with O^{2-}, Fe^{3+}, and Dy^{3+} distribution. (d) EELS spectrum from an oxygen-deficient region. (e) (f) XPS peaks for Fe 2p and Tb and Dy 4d respectively from the R21-oxide film.* 53
5.3 *(a) Evolution of resistivity with different annealing cycles for FDTO film with R = 21; (b) Room temperature resistivity vs number of heating cycles (c) Resistivity of the post-annealed film from 10 K to 700 K* 54
5.4 *(a) Hall mobility as a function of temperature (b) Carrier concentration as a function of temperature (c) Plot of conductivity vs temperature for the low temperature (200 K-300 K) and high temperature (300 K-700 K) regimes* 55

5.5 *(a) Photoconductivity and absorbance for the R21-oxide film (b) Valence band maximum from XPS of the R21-oxide film (c) Absorbance and Tauc plot analysis for furnace-annealed film.* . . . 57
5.6 *(a) Magnetization vs magnetic field plots for the as-prepared and R21-oxide films (b) Magnetoresistance of the R21-oxide film with field both IP and OOP (c) Kerr measurement (longitudinal) for as-prepared and R21-oxide films* . . . 58

6.1 *Plot of density and film thickness as a function of O_2 pressure.* . . . 62
6.2 *Figure panel showing XPS peaks obtained from FDTO films deposited at pressures from $5x10^{-6}$ Torr to $1.5x10^{-6}$ Torr* . . . 64
6.3 *(a) HR-TEM cross-section image, nano-diffraction patterns, and elemental distribution from EELS of FDTO film deposited at $1.5x10^{-6}$ Torr. (b),(c) Plots of relative percentage of the different cation peaks, Fe^{3+}/Fe^{2+} and $Dy^{3+}/(Tb^{3+},Tb^{4+})$ obtained from XPS as a function of O_2 pressure* . . . 65
6.4 *(a) Plot of magnetic hysteresis loops for FDTO films deposited at different O_2 pressures. (b) Magnetoresistance (%) plotted for FDTO films deposited at $2x10^{-6}$ Torr and at $4x10^{-6}$ Torr.* . . . 65
6.5 *(a) Plot of room temperature magnetic moment and resistivity of FDTO thin films on quartz as a function of O_2 pressure. (b) XAS and XMCD of FDTO film deposited at $2x10^{-5}$ Torr (c) Resistivity vs temperature (from 8 K to 300 K) for FDTO films deposited at $5x10^{-5}$ Torr and $1.5x10^{-5}$ Torr (d) Plot of variable resistance hopping (VRH) fits to the data in (c)* . . . 66
6.6 *Direct and indirect Tauc plots for FDTO films deposited at different pressures* . . . 67
6.7 *(a) Plot of optical transmission as a function of wavelength for all FDTO films. (b) Plot of direct and indirect bandgap for the FDTO films as a function of O_2 pressure. (c) Plot showing work function of two FDTO films deposited at different pressures. (d) Valence band maximum edge for two FDTO films deposited at different O_2 pressures.* . . . 68

7.1 *Magnetic hysteresis loop of FDTO/BFO and FDTO/quartz* . . . 72
7.2 *(a) HR-TEM image of FDTO/BFO interface in as-prepared state (b) XRD of BFO film* . . . 73
7.3 *(a) Ferroelectric hysteresis loop, and (b) ferroelectric fatigue measurement of FDTO/BFO capacitors* . . . 74
7.4 *(a) Magnetic hysteresis and %GMR plot for the FDTO/BFO GMR device (b) Plot of %GMR showing electric field modulation at room temperature (c) HRTEM image of the cross-section of the GMR device* . . . 75

8.1 *Figure showing extraordinary optical and electrical properties of FDTO* . . . 77
8.2 *Figure showing high conductivity and magnetism in FDTO films of different cation stoichiometry* . . . 78
8.3 *Figure showing the effect of cyclic anneal on the resistivity, microstructure, and magnetic property of iron-rich FDTO film.* . . . 78

8.4 *Figure showing microstructure and chemical composition, resistivity and magnetism, and bandgap (from left to right respectively) of FDTO films deposited as a function of O_2 pressure.* 79
8.5 *From top-left corner in clockwise direction: TEM image of clean FDTO/BFO interface, good ferroelectric hysteresis, and robust fatigue test for FDTO/BFO capacitors. TEM image of GMR device structure, room temperature ME coupling in GMR device, magnetic hysteresis showing magnetic coupling between FDTO/BFO films.* 80

Chapter 1

Introduction

1.1 Motivation

The overall goal of this thesis is to synthesize and investigate the electrical, optical, and magnetic properties of novel amorphous Fe-Tb-Dy-oxide (FDTO) thin films that have potential applications in electronic, memory, and energy devices. The oxide was a serendipitous discovery by our group when thin films less than 100 nm of a well known metal alloy (Terfenol-D) was deposited and characterized [1]. However, there was significant interest to further pursue and investigate this material since it not only presents new materials physics, but also has important implications in the electronics industry as a new class of amorphous oxide semiconductor (AOS).

The more specific incentive for this thesis is to investigate thin films of amorphous, semiconducting ternary oxides composed of Fe-Tb-Dy (FDTO) in order to understand the origin of their optical and electrical properties. The research is motivated by the high conductivity, room-temperature magnetism, and transparency that this iron-based oxide demonstrates, a phenomenon that has not been observed before in such ternary amorphous metal oxide systems [2–10]. Prior to the discovery of this transition metal-rare earth oxide system, only post-transition metal oxides composed of cations having electronic configuration of (n-1)d^{10} ns^0 have shown a combination of transparency and high conductivity, and it has been attributed to the large s-character of conduction [11–16]. The additional presence of magnetism in FDTO [17] makes it an even more intriguing system to explore. Such oxides not only have applications in solar cells and display systems [13, 15, 18–20], but also in memory devices for data storage [21–23]. Some of the applications of amorphous transparent conducting oxides (a-TCOs) that make them so desirable are summarized below.

1.1.1 Materials with multifunctional properties

In terms of electrical properties, solid-state materials can be classified into three major categories: metals, semiconductors, and insulators. Simplified band diagrams for all three categories are shown in Fig. 1.1 [24], where the red areas are allowed bands, the blue ones are forbidden bands, the dotted line represents the Fermi energy level, the small white cups represent states that can be occupied (or are occupied) by electrons, the green circles represent electrons, and the green arrows represent the spin on the electrons. The Fermi

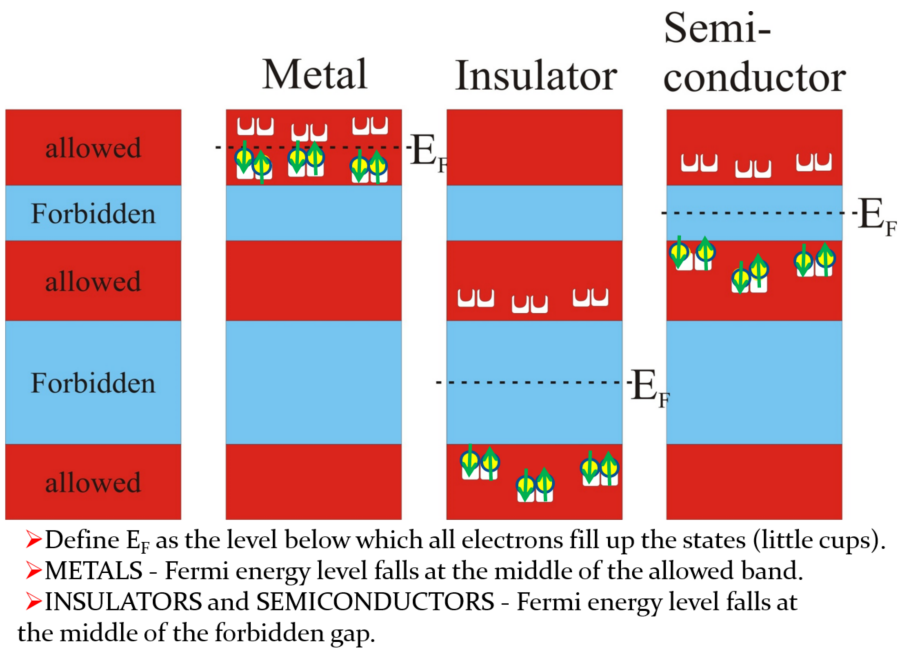


Figure 1.1: *Simplified band structure of metals, insulators, and semiconductors (from left to right). Electrons are denoted by green circles, their spins shown as green arrows, and their states shown as little white cups. For conduction to happen, electrons must get excited to an empty state . In metals the Fermi level is inside an allowed band and intraband electron excitations take place. In insulators and semiconductors, the Fermi level lies in the middle of a forbidden gap, so electrons must traverse the forbidden gap and reach an empty state for conduction to take place: this gap is also known as the bandgap. This gap is higher in insulators than in semiconductors, and so conduction is higher in semiconductors as compared to insulators. [24]*

level is the maximum energy at which all electrons sit in a material at 0 K. Any energy level above the Fermi level can be thought of as the conduction band, i.e. the band that has empty states, and into which, electrons can get excited and thereby conduct electricity. In case of metals, the Fermi level lies inside an allowed band, and therefore, it takes very little energy for exciting the electrons from the filled states to the empty states across the Fermi level, resulting primarily in intraband transitions. This is why metals are very good conductors since there is enough energy at room temperature to excite the electrons to states above the Fermi level. In case of insulators and semiconductors, the Fermi level lies in the middle of a forbidden band, so the allowed filled band below the Fermi level is the valence band (VB) and the allowed empty band above the Fermi level is the conduction band (CB). Therefore in these systems, the electrons must go through interband transitions for conduction to take place. The energy between the CB and VB (also known as the bandgap, E_g) in insulators is very high, so they do not conduct. For semiconductors, the E_g is smaller than in insulators, such that if the electrons gain energy from external heating, or from photons, they can get excited to the CB.

Optical transparency arises when the material does not absorb energy in the visible spectrum (1.65 - 3.1 eV) or below it. . Insulators typically have very high bandgap (> 4 eV), for example thermally grown amorphous SiO_2 was measured to have bandgap of 9.3 eV [25]. Optical transparency is most commonly found in insulators. In contrast, electrons in metals can accept energy from photons of all energies because

of the very small energy needed for intraband transitions. In addition, when the electrons relax back to the lower energy states, they emit that energy - therefore not only are metals opaque, but they are also very reflective. Hence the co-existence of transparency and high conductivity at room temperature is not a common occurrence in typical materials. Semiconductors, however, can be either transparent or opaque. Cadmium sulfide (CdS), an n-type semiconductor, is yellow in color and has a bandgap of 2.42 eV [26], while tin oxide (SnO_2), also an n-type semiconductor, is transparent and has a bandgap of 3.6 eV [11]. SnO_2 is also conductive at room temperature, and only a few such semiconductors exist that are transparent conducting oxides (TCOs) [11, 13, 27–30]- the origin of this unusual combination of optical transparency and room temperature conductivity will be discussed in the next section.

When the addition of magnetism, a property that is dependent on electron spins, is brought into the picture, materials exhibiting conductivity, optical transparency, *and* room temperature magnetism are even rarer to find. Magnetism arises in materials due to unpaired electrons in the outer orbital. These are typically the elements that fall in the middle of the transition metals (such as Fe, Mn, Co, Ni) and lanthanides in the periodic table. Magnetite (Fe_3O_4) is one of the most well-known naturally occurring oxide that is ferrimagnetic at room temperature and exhibits low resistivity (~10 mohm-cm) due to its half-metallic behavior [7, 8, 31, 32]. A new field of research has evolved where well-known conducting oxides are doped with magnetic atoms to obtain dilute magnetic oxides [33], or typical III-V semiconductors such as gallium arsenide (GaAs) are doped with magnetic atoms to produce dilute magnetic semiconductors [34, 35]. Both of these classes of materials, and reservations about them, will be discussed in more details in the next section.

Most of the aforementioned multifunctional oxides (that combine either transparency and magnetism, or conductivity and magnetism) are crystalline in nature. Introduction of disorder in a system often leads to deterioration of electrical and magnetic properties. Disorder introduces localized states in the band which leads to reduced conductivity and mobility, while disorder tends to create anti-ferromagnetic grain boundaries which degrade magnetism in the material - this is often the case for thin films of Fe_3O_4 [7, 36]. Only the oxides whose CB is made of s-orbitals tend to be unaffected with loss of crystallinity [11, 12], and this will also be discussed in further detail in the next section. However, amorphous oxides are very low-maintenance: they do not require precise control of high temperature during deposition, and so can be more energy efficient to deposit in large scale. Therefore, a multifunctional amorphous oxide would not only have a significant impact in the electronics industry, but also open up new understanding of material physics.

1.1.2 Applications of multifunctional amorphous oxides (AOx)

Based on the particular electrical, magnetic, and optical properties of amorphous oxides, they have a wide range of applications, some of which are demonstrated in Fig.1.2. Amorphous oxide semiconductors (AOSs) are most commonly used as channel layers in transistors that are subsequently used for various electronic devices. For example, amorphous tin oxide has been used for pH sensors [37], tungsten oxide for ammonia [38] and sub-parts-per-million nitrogen dioxide [39] gas sensors, zinc-tin-oxide for oxygen sensors [40], and indium-gallium-zinc oxide for temperature sensors [**?**]. In addition, amorphous gadolinium oxide has been tested for non-volatile memory applications [41] while amorphous zinc-doped silicon oxide has been used for resistive switching memory [42]. Manganese dioxide has been utilized for electrochemical

capacitors [43], and when doped with vanadium, it has been applied towards supercapacitors [44]. The AOSs that display optical transparency find applications in thin film transistors (TFTs) specifically used for active matrix (AM) flat panel displays such as AM liquid crystal display (AMLCD) and AM organic light emitting diode (AM-OLED) (Fig. 1.2(a)) [13, 45], applications which have been traditionally dominated by amorphous hydrogenated silicon (a-Si:H) [45]. In the review paper by Kamiya et al. on applications of transparent AOSs, the authors mentioned electronic-paper (both black-and-white and colored) as being revolutionary applications for flexible interactive displays that make use of transparent AOS [13]. The main advantage of using amorphous materials for such applications is the low processing cost in terms of scalability [45]. Transparent AOx also find vital applications in renewable energy as transparent conducting oxide (TCO) for thin film solar cells (Fig.1.2(b)). One of the best known TCO is indium-tin-oxide (ITO) that is not only used as a top layer for solar cells [27, 41], but is also frequently used as a transparent electrode for photocatalysis [29, 46, 47]. Amorphous ITO is enabling the production of flexible solar cells and flat panel displays [19, 41] that are becoming more and more popular for wearable and versatile source of renewable energy. Amorphous vanadium oxide has been reported to be used as an electrode for rechargeable aluminum batteries [48], while a tin-based amorphous oxide has been reported as a high capacity lithium-ion storage material for applications in lithium-ion batteries [49]. Amorphous oxides with high refractive index, such as a-SiO_2 and a-TiO_2, are used as dielectric layers in devices (Fig. 1.2(c)). One of the more emergent applications of amorphous semiconductors is in the field of spintronics, where the material has to be magnetic (preferably with a Curie temperature above 300 K) in addition to being a semiconductor. One such application is shown in Fig. 1.2(d), where a spin filter device was fabricated using the perovskite lanthanum strontium manganite (LSMO); although the device showed about 40% magnetoresistance signal, the measurement was done at 11K since the Curie temperature of magnetic semiconductors are typically lower than 300 K. These materials and their applications will be discussed in more detail in the next section.

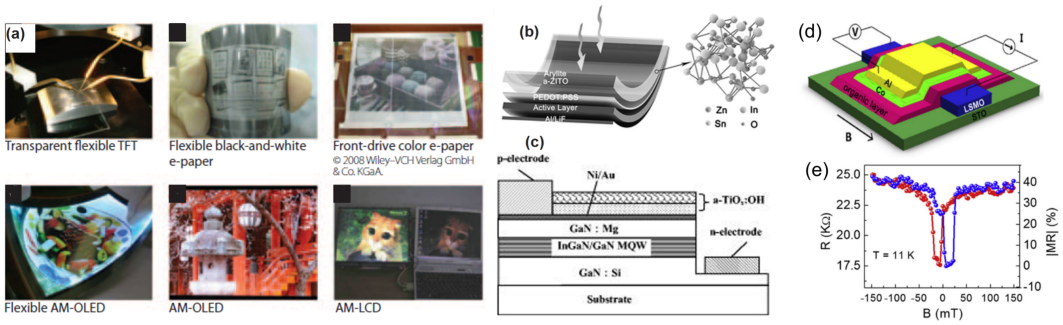


Figure 1.2: *Some applications of amorphous oxides. (a) Channel layer in thin film transistors for display [13] (b) Transparent conducting oxide in flexible solar cell [50] (c) High refractive index layer for LED [51] (d) Schematic of a spin valve device made using ferromagnetic conductor and (e) showing its magnetoresistance behavior at 11 K [52]*

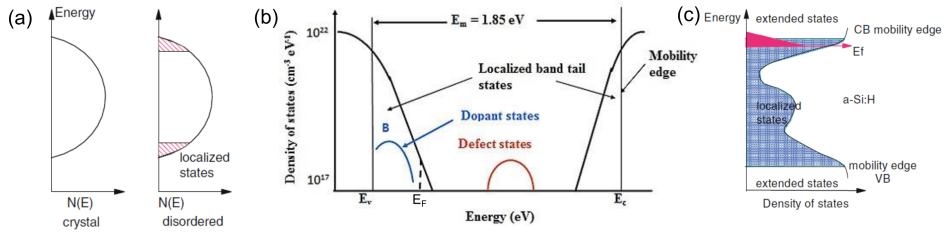


Figure 1.3: *(a) Figure showing effect of disorder on an s-band, where the left panel shows s-band in a crystal, and the right panel shows localized states (shaded red line) appearing and propagating into the band [11]. (b) Band structure of a typical semiconductor showing the mobility edge, localized tail states, states caused by dopants, and defect states that act as charge trap centers. The states in the CB above mobility edge and those in VB below mobility edge are the extended states [53]. (c) Band structure of n-type a-Si:H showing a large tail state from the VB and a smaller tail state from the CB, all of which is localized. The tail state from the VB also affects the Fermi level [11].*

1.2 Current knowledge and challenges

This section will focus on what is known about thin films of AOSs, the origin of their electrical, optical and magnetic properties. It will also give a review of the current status in multiferroic materials and using them for spintronic devices.

1.2.1 Transparency, conductivity, and magnetism in amorphous oxide semiconductors (AOSs)

1.2.1.1 *Band structure and conduction mechanisms in amorphous semiconductors*

Unlike crystalline materials, amorphous systems have a large degree of disorder. This disorder results in defects, dangling bonds, voids, microvoids, and impurities, which in turn give rise to localized trap states between the valence band and the conduction band [53, 54]. Oxygen vacancies and oxygen excess form donor and acceptor trap states respectively in oxide semiconductors [30]. These trap states are electrically-active because they are capable of trapping charge carriers, thus affecting their freedom of motion, and hence the conductivity of the system. In addition to these trap states, Anderson showed that disorder also leads to localization of electron states in the band structure [11, 55]. Mott later explained that disorder first localizes the states at the band edges, resulting in an energy known as the mobility edge, where the transition happens from the localized tail states to the extended states [11, 56–58]. As disorder in the system increases, the localized states move further into the band as seen in Fig. 1.3(a) which shows the effect of disorder on an s-band [11]. Quantum mechanical tunneling between these localized states can cause electrical transport, but the conductivity resulting from this tunneling is not very high [54]. A generalized band picture of amorphous materials that includes defect states and localized tail states is demonstrated in Fig. 1.3(b) [53].

One of the most thoroughly studied amorphous semiconductor is amorphous-hydrogenated silicon (a-Si:H), a non-degenerate doped semiconductor, whose band structure is shown in Fig. 1.3(c). Due to the distortion of the Si-Si bond angle and dihedral angle of the p-orbitals making up the VB, a tail state arises at the CB and an even larger tail state arises near the VB respectively; all these tail states are localized [11]. In this system, conduction can take place through the extended states in the CB (for n-type a-Si:H), VB (for

p-type a-Si:H), and through the localized tail states in the mobility gap. At relatively high temperatures (i.e. near room temperature) conduction takes place through the extended states in the CB. This results in the activation-type dependence of the conductivity, σ on temperature, given by [54]

$$\sigma = \sigma_0 exp(-\Delta E/kT) \tag{1.1}$$

where $\Delta E = E_c - E_F$, the difference between the mobility edge and the Fermi energy known as the activation energy. The pre-exponential factor is given by

$$\sigma_0 = \sigma_{00} exp(\Delta E/E_{MN}) \tag{1.2}$$

where σ_{00} is a constant and E_{MN} is called the Meyer-Nedel characteristic energy. The implication of the Meyer-Nedel energy is that the plots of σ vs 1/T for the same material but doped with different dopant concentrations will converge at the conductivity value σ_{00} and focal temperature given by $T_C = E_{MN}/k$, where k is the Boltzmann constant.

At low temperatures, the number of carriers increase in the tail states, and so conduction moves from the extended states to the localized tail states that are in the vicinity of the Fermi energy level [53, 54]. In this case, charge carriers hop either between localized trap states or between nearest neighbor atoms, all having binding energy in the vicinity of the Fermi energy level. The probability of an electron tunneling from one localized state to another at a higher energy depends on the following three factors [53, 58]: (i) the attempt frequency $\nu(ph)$ which is of the order of 10^{12}-10^{13}s-^{1}, (ii) the wave function of the electron, and (iii) the probability of finding a phonon with excitation energy, (ω) large enough for the tunneling to occur. This probability, P, is given by

$$P = \nu(ph) e^{-2\alpha R} e^{-\omega/kT} \tag{1.3}$$

where $\xi = 1/\alpha$ is the decay length of the localized wave function, R is the spatial distance between the two hopping sites, ω is the energy difference between the two states, and k is the Boltzmann constant. The product αR determines whether conduction will take place by nearest neighbor hopping (NNH) or variable range hopping (VRH). NNH conduction is expected if the average distance to the nearest neighbor, R_0, is much larger than the decay length of the localized wavefunction (i.e. $R_0/\xi >> 1$). NNH is also more probable when the electron is localized on a weak bond in the conduction tail state [54]. The temperature dependence of conductivity for NNH is similar to that for thermal activation.

VRH is expected if $R_0/\xi \leq 1$, which means the decay length of the wavefunction is either equal to or greater than the nearest neighbor distance. In this case the electrons hop between localized states near the Fermi level. Einstein's relation describes the mobility as

$$\mu = \frac{eD}{kT} \tag{1.4}$$

where $\mu = \frac{PR^2}{6}$. This results in the following expression for conductivity, which is given by $ne\mu$, as

$$\sigma = (1/6)e^2R^2\nu_{ph}N(E_F)exp(-2\alpha R)exp(-W/kT) \tag{1.5}$$

As temperature decreases, energetic phonons become less available, and so the electrons will try to hop larger spatial distances, which might be energetically closer to them, than the nearest neighbors. This results in a variable range in the hopping distance between the localized traps, where the exponential term $exp(-2\alpha R - W/kT)$ will not have a maximum value for the nearest neighbor distance. Mott [58] used an optimization procedure to obtain the most probable jump distance, given by

$$R = \{\frac{9}{8\pi\alpha N(E_F)kT}\}^{0.25} \tag{1.6}$$

Using this expression for R, the conductivity can be written as

$$\sigma = \sigma_0 e^{-(T_0/T)^{1/4}} \tag{1.7}$$

where σ_0 is the pre-exponential factor and T_0 is the characteristic temperature. Although the exponent of 1/4 is found to fit many systems in a certain temperature range, it is not always found to be the case for all range of temperatures [54]. In general, the DC conductivity can be described by [54]

$$\sigma_{DC} = \sigma_0 e^{-(T_0/T)^{\gamma}} \tag{1.8}$$

where $1/4 \leq \gamma \leq 1$. Because the hopping conduction occurs in the localized states in the vicinity of the Fermi level, the details of the DOS around the Fermi level is important. Mott considered a constant DOS and obtained the exponent of 1/4 for a 3-D system. However, Efros and Skhlovskii considered the Coulomb interaction, and found that the DOS becomes zero at the Fermi level, a feature known as the Coulomb gap. In such a case, the exponent has a value of 1/2. In general, $\gamma = \frac{1}{d+1}$, where d is the space dimension. Singh and Shimakawa [54]also mentioned that the exponent can be less than 1 if the fractal nature of disordered systems is taken into account.

1.2.1.2 *Hosono's Rule for transparent amorphous oxide semiconductors (TAOS)*

In 1996, Hosono [14] proposed the first hypothesis for the formation of transparent AOS (TAOS) possessing high hall mobility and conductivity. Wide bandgaps necessary to achieve transparency are obtained by the low energy of the oxygen (O) 2p orbital forming the top of the valence band. In addition, a high carrier mobility can be achieved by a large width of the conduction band, the magnitude of which should be independent of the structure of the atom to maintain the amorphous criteria. Thus, the cations fulfilling all these criteria are the heavy metal cations possessing an electronic configuration of (n-1)d^{10} ns^0. When the ns orbital forms the bottom of the conduction band, the large overlap between the s orbitals of the neighboring cations allow for electron paths that give rise to high conductivity and high mobility, as shown in Fig. 1.4(a). Any other orbital, e.g. p-p or d-p have high spatial orientation that causes a reduced hall mobility value in the amorphous microstructure. In addition, because the s orbitals are spherical, disorder in the material does not give rise to localized states that typically cause conductivity to drop [11]. In a review article in 2006,

Hosono also compared these ionic TAOS (ITAOS) with covalent ones and glassy semiconductors [59]. The conduction mechanism is widely different between the ITAOS and the glassy semiconductors: in the former the conduction path is constituted by the overlap of the neighboring metal cations, whereas in the latter the conduction mechanism is VRH, and according to the discussion in the previous section, hopping conduction leads to very low mobility. The overlap between orbitals of the neighboring metal cations is in fact a criteria for TCOs such as In_2O_3, SnO_2, ZnO. Too much overlap in certain cases even leads to degenerate states in the material where the carrier concentration is of the order of 10^{20} cm^{-3}.

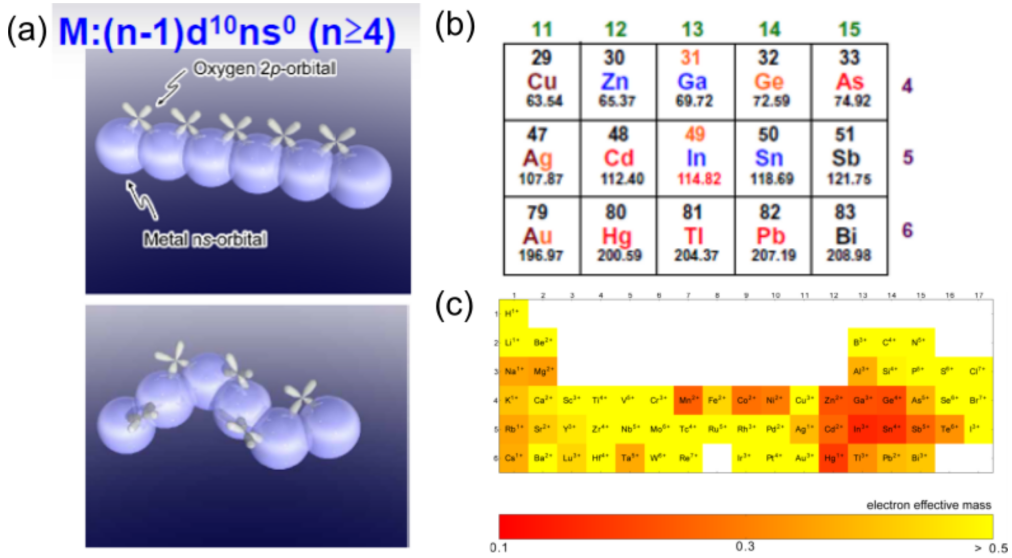
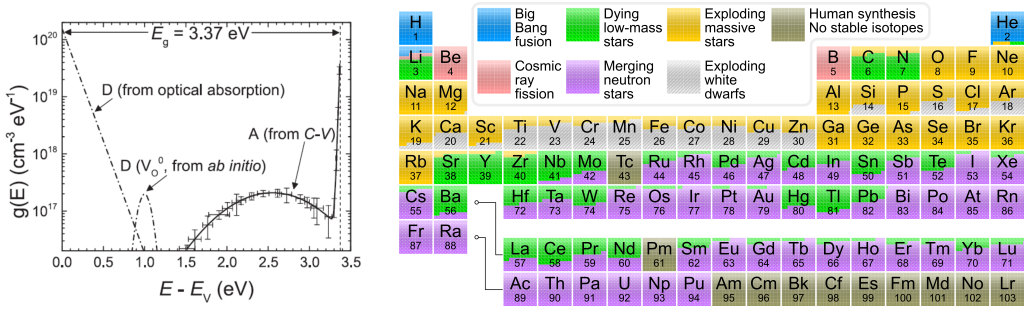


Figure 1.4: *(a) Hosono's proposed model showing ns orbital of the heavy metals overlapping with each other while the O-2p orbitals form the valence bands; the orientation of the atoms can change, as in an amorphous material, without compromising carrier mobility [14]. (b) List of cations proposed by Hosono for synthesizing AOS exhibiting high mobility, conductivity, and optical transparency [45] (c) Electron effective mass of most cations found by ab initio calculations [60]; the lowest effective mass cations overlap with the list of cations proposed by Hosono in (b) .*

Based on the relative earth availability and toxicity of the short-listed heavy metal cations shown in Fig. 1.4(b), only a few can be employed for widespread use in electronic devices. These elements, shown in blue in Fig. 1.4(b), are indium, tin, gallium, and zinc. The red elements are generally avoided due to their high toxicity, the brown elements can be used for designing p-type semiconductors, the orange ones are expensive and thus not suitable for large scale production, and the black elements have not been validated yet as being useful for AOS. For the application of AOS as TCO or transparent electrodes where high conductivity is required, the most successful materials are indium and fluorine doped-tin oxide as well as undoped tin oxide (ITO, FTO and SnO_2) [18, 61–63], and aluminum and gallium doped zinc oxide [62, 64]. It should be emphasized that while In is critical to such conducting oxides, it is a precious metal and alternate materials need to be designed and/or discovered. These materials can also be categorized to be under Hosono's hypothesis. In fact, Hautier et al mentioned in their paper [60] that upon carrying out "ab initio computing" [60] to scan through 4000 binary and ternary oxides, the metal cations highlighted by Hosono turned out to have the least electron effective mass as shown in fig. 1.4(c). The electron effective mass, mobility, and



(a) (b)

Figure 1.5: *(a) Band structure of a-IGZO [30](b) Earth abundance of elements [65]*

conductivity are related by the following equations:

$$\mu = \frac{e}{m};\ \ \sigma = ne\mu$$

where μ is the carrier mobility, m is the electron effective mass, e is the charge on an electron, σ is the conductivity, and n is the carrier concentration. From this it is evident that a lower effective mass leads to higher conductivity.

The band structure of one of the most well known TAOS, a-In-Ga-Zn-oxide (a-IGZO), has been thoroughly studied by multiple groups [16, 30, 66, 67]. The resulting picture, shown in Fig. 1.5(a), illustrates that there exists exponential tail states below the CB overlapping with deep gap states from the s orbitals. About 1 eV above the VB, there are fully occupied donor states originating from oxygen vacancy, and there is also a large tail above the VB. So far, the AOs mentioned in this section are the only amorphous oxides that have shown very high conductivity, high optical transparency at room temperature. However, the options are limited, and considering earth abundancy of these materials (shown in Fig. 1.5(b)), including the small concentration of In on the earth's crust (Fig. 1.5(b)), new options would be welcome in the materials community.

1.2.1.3 *Magnetism in amorphous oxides and semiconductors*

Magnetism originates from two sources - orbital motion of electrons, and the spin of the electrons. Atoms exhibit magnetism when they have unpaired electrons in the outer orbital. Elements in the middle of the transition metals and lanthanides have unpaired electrons, including their cations that have unpaired electrons too. However, simply the presence of unpaired electrons is not sufficient to sustain magnetism at room temperature. In many materials having unpaired electrons, the spins point haphazardly in all directions, and only align when a magnetic field is applied. Once the field is removed, the spins go back to their misaligned states- these are paramagnetic materials. In materials that are magnetic at room temperature, the spins are all aligned because that is the structure that allows the system to sit at minimum energy. However, if the material is heated, the system gains thermal energy causing the spins to slowly get misaligned. The temperature at which the spins are completely misaligned (and hence the magnetic moment is zero) is called the Curie temperature (and Neel temperature for anti-ferromagnets). Once the system is cooled down again, the

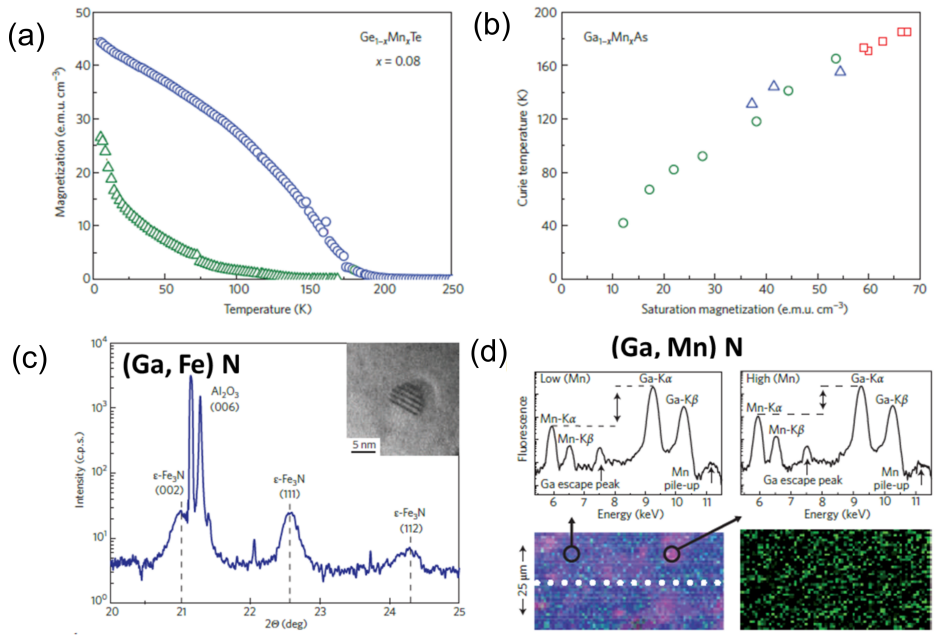


Figure 1.6: *(a) Mn-doped GeTe showing Curie temperature close to 200 K [69] (b) Curie temperature as a function of Mn-doped GaAs (c) Fe nanoclusters observed in Fe-doped GaN (d) Mn nanoclusters observed in Mn-doped GaN* [68]

spins will align once more, but will not return to their initial aligned state. In the case where all the spins are aligned in one direction, the material is ferromagnetic. If the spins are aligned in opposite directions, the material is antiferromagnetic. There are some cases where the spins are aligned in opposite directions, but the magnitude of the spins in one direction is higher than that in the opposite direction - these are ferrimagnetic materials e.g. magnetite (Fe_3O_4). There are also canted anti-ferromagnets where the spins are aligned opposite to each other but at an angle. Magnetism can possibly be introduced into any system - amorphous or crystalline - by the addition of atoms carrying a magnetic moment [33, 68–72]. The aim, of course, is to achieve multifunctional materials that are magnetic semiconductors, and possibly transparent.

Traditional III-V, and II-VI semiconductors (e.g. GaAs, GaN, GeTe) have been doped with magnetic atoms such as Mn, Co, Fe, and Ni [68, 73–75]. The resulting films, known as dilute magnetic semiconductors (DMS) have semiconducting and magnetic behavior, however the highest Curie temperature was 190 K as seen in Fig.1.6 (a) and (b), way below 300 K and the operating temperature of most devices [68, 74, 76]. Some of the well-investigated systems that observed Curie temperature above or equal to 300 K discovered clusters of magnetic atoms non-homogeneously distributed, as seen in Fig. 1.6 (c) and (d).

Traditional TCOs such as SnO_2, ZnO etc. have also been doped with magnetic atoms such as above [70, 76, 77] - these materials are known as dilute magnetic oxides (DMO), and they already have been observed to exhibit Curie temperatures above 300 K [33, 35, 68]. The surprising part about these materials is that doping concentration with the magnetic atom is less than the percolation threshold, a phenomenon that goes against conventional understanding of magnetic systems. In his comments article [33], Coey expressed several reservations about these magnetic oxides. He provided a set of criteria that must be fulfilled for

Table 1.1: *Bandgap, resistivity, and magnetic moment of iron, terbium, and dysprosium oxides.*

Material	Bandgap, E_g (eV)	Resistivity (ohm-cm)	Magnetic moment (emu/cc)
$\alpha - Fe_2O_3$	2.1 [78, 80]	100 [5, 6, 78, 81]	non-magnetic
$\gamma - Fe_2O_3$	2,4 [82]	0.25 [83]	294 [2]
Fe_3O_4	0.45 [84] (for dominant spin direction)	0.01 [7, 31, 32, 85]	480 [7, 31, 32, 85]
Tb_2O_3	3.8 [86]	insulating [9]	non-magnetic
Dy_2O_3	4.9 [86]	insulating [10]	non-magnetic [87]

an oxide to be considered a magnetic semiconductor. One of those criteria was the observance of x-ray magnetic circular dichroism signal from the L-edge of the magnetic dopant, the other was the observance of a magnetoresistance to show the carriers are related to the origin of magnetism. However, the magnetic oxides reported in the article had failed to meet all the criteria, and so doubt remained on the validity of their applications in devices. However, these were perfect for magneto-optic applications where the charge carriers do not play a significant role.

1.2.1.4 *Oxides of iron, terbium, and dysprosium*

Table 1.1 provides a quick summary of the naturally found oxides of Fe, Tb, and Dy.

Iron oxides exist mainly in two forms - hematite (Fe_2O_3) and magnetite (Fe_3O_4). Hematite has three different phases, $\alpha - Fe_2O_3$, $\beta - Fe_2O_3$, and $\gamma - Fe_2O_3$. Out of these three, $\gamma - Fe_2O_3$has a spinel structure, while the rest are cubic [78]. Hematite is desirable for water splitting applications due to its band-gap of 2.1 eV and good alignment of its CB and VB with the oxidation and reduction potential of water. [4, 78–80], but because of its poor conductivity, it cannot be used effectively as an electrode. Studies have been done to dope hematite to increase its conductivity, but the highest conductivity is still of the order of 10^{-2} S/m and conduction happens via VRH [5, 6, 78, 81]. The α-phase of hematite is weakly antiferromagnetic at room temperature. The γ-phase is ferromagnetic at room temperature with a magnetic moment of 294 emu/cc with resistivity of around 250 mohm-cm [2] and bandgap of about 2.4 eV [82]. This is summarized in Table 1.1.

Magnetite has a spinel structure and exhibits half-metallicity [78], meaning that the DOS for one spin state overlaps with the Fermi level. As such, the conductivity of magnetite is of the order of 10 mohm-cm [7, 8, 31, 32, 78]. It is also ferrimagnetic, with a magnetic moment of about 480 emu/cc in the epitaxial films [7, 8, 31, 32, 78]. However, the presence of disorder and grain boundaries in the material give rise to anti-phase boundaries that deteriorate the magnetic properties of magnetite [36].

Terbium oxide can exist in two forms - Tb (III) oxide (Tb_2O_3), and Tb (III, IV) oxide (Tb_4O_7). Both the forms are insulating because of a combination of a large bandgap and heavy effective mass of conduction electrons resulting from the small curvature of the f-orbitals. The bandgap of terbium oxide is around 3.8 eV. Although terbium oxide is not ferromagnetic at room temperature, Tb^{3+} cations carry a large magnetic moment due to unpaired electrons in the outer orbitals; a recent study has reported the improvement in the

magnetic properties of bismuth ferrite upon doping with terbium cations [9, 88, 89]. Like terbium oxide, dysprosium oxide is also known for its dielectric properties with a bandgap of about 4.9 eV. It exists mostly as Dy_2O_3, and is also insulating due to large bandgap and f-orbital derived conduction bands [10]; Dy_2O_3 is non-magnetic at room-temperature and has a Neel temperature of 1.2 K [87].

Given that none of these oxide materials (except for magnetite) exhibit high conductivity and magnetism at room temperature, it would be difficult to predict how the ternary oxide composed of all three of these metals can be conducting and ferromagnetic at room temperature. *Chapters 3 and 6 describe the study of the effects of cation composition and of oxygen pressure on these properties in Fe-Tb-Dy-oxide and offers possible hypothesis on the origin of these properties.*

1.2.2 Spintronics

Spintronics is the field of electronics where the spin of the electron can be controlled and manipulated in addition to its charge. In electronics there are two main categories of devices - switching devices and memory devices. Switching devices, which are mainly made of transistors, use a gate voltage to manipulate the current passing through the device (current high typically is ON state, current low is OFF state), and hence require semiconductor materials in which the charge carriers are easy to manipulate. Memory devices make use of room temperature ferromagnets, where the spin of the electron can be modulated to store data. As technology progresses, there is a need to store larger amounts of data in smaller spaces, creating the need to further reduce device sizes. This leads to the problem of approaching the limit predicted by Moore's law, where the device size cannot be reduced any further because of heat generation and breakdown of potential barriers in the different layers [90–92].

Data is stored on a magnetic drive by passing a current through coils on the write-head, which generates a magnetic field that is capable of flipping the spin of the magnetic layer. Researchers have been working on introducing dynamic memory drives such as random-access memory (i.e. RAM) that uses spin to store data instead of current, as in the conventional design. This would make them not only faster, but also energy efficient since the spin information can be stored without having to pass a constant current. Other spintronic devices are spin filters, tunnel junction devices, and even light-emitting diodes (LEDs) that can be modulated with a magnetic field [22, 23, 52, 93]. For this purpose, new materials are needed that combine magnetism and semiconduction. Some of the candidates are the DMOs and DMSs described in the last section. However, as described in that section, material optimization is still an ongoing process in that area.

A second way to achieve the modulation of spin in devices without having to apply a magnetic field like in memory drive write-heads, is through magneto-electric coupling, which is described in the following section.

1.2.2.1 *Magneto-electric (ME) coupling for memory devices*

Magneto-electric (ME) coupling is one of the branches of multiferroics, where two ferroic properties of materials are coupled. In simple terms, ME coupling allows the control of the magnetic property (spin) of a ferromagnetic material through controlling the electrical property (polarization) of a ferroelectric material

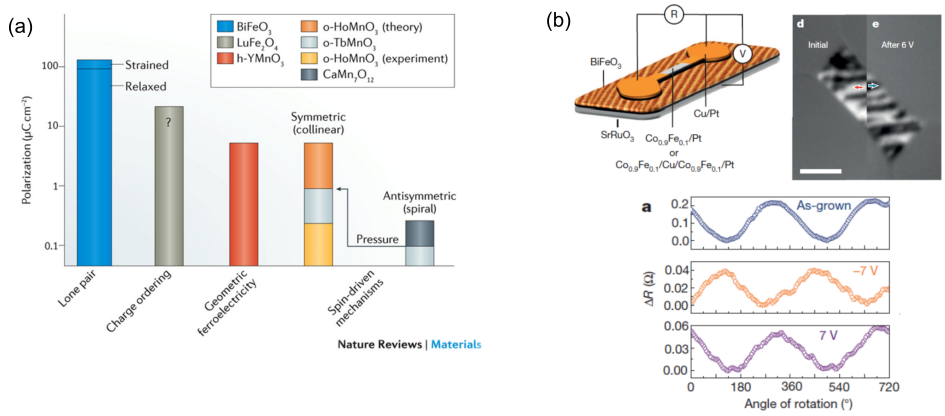


Figure 1.7: *(a) Single phase multiferroic materials [95] (b) Room temperature ME coupling in CoFe/BFO structure [101]*

[94]. ME coupling can be observed in two ways - (i) a single phase material that exhibits both ferroelectric and ferromagnetic properties, and (ii) composite multiferroics where ME coupling takes place between a ferromagnetic and a ferroelectric layer. Single phase ME coupling is difficult because the criteria for ferromagnetism and ferroelectricity to appear naturally in a material are mutually exclusive. One of the points of contradiction is that ferroelectricity requires empty d orbital whereas ferromagnetism requires a partially filled one [95, 96]. Existing single phase multiferroic materials (such as $BiMnO_3$, $LaMnO_3$, and $BiFeO_3$) are typically perovskite structures, which work around the problem by having the off-centered transition metal cation as the source of ferroelectricity [97]. Studies have been also done on synthesizing multiferroic composites that have a ferromagnetic material dispersed in a ferroelectric matrix, e.g. cobalt ferrite-barium titanate [98, 99]. However, most of the materials that have been engineered to show both properties (Fig. 1.7 (a)) are not functional at room temperature, which limits their practical applications in spintronics based memory devices. One recent study has reported the observation of room temperature ME coupling in a single phase chromium-doped barium titanate [100] but no functioning devices have been shown using this material.

Therefore, focus has shifted towards multiphase/composite multiferroics. Typical ferroelectric materials used for this purpose are $BaTiO_3$ (BTO) and $BiFeO_3$ (BFO). The choice of a magnetic layer is the most difficult part. Successful ME coupling at room temperature has been demonstrated in Co_xFe_{1-x}(CoFe)/BFO heterostructures [101]. This is shown in Fig.1.7 (b), where a spin valve structure was made from the two layers (top-left image). The top right image shows x-ray magnetic circular dichroism coupled to photoelectron emission microscopy (XMCD-PEEM) measurements, where the spin in CoFe is seen to switch upon application of a +6 V and -6 V potential. Finally, the bottom image shows the anisotropic magnetoresistance (AMR) signal of CoFe layer completely switching when a negative voltage is applied. However, the problem with this heterostructure was the CoFe/BFO interface was not stable, and device performance degraded only after about 3 switching cycles.

One way to overcome this issue is to use an oxide ferromagnetic layer for coupling. This is where the DMOs discussed earlier can play an important role. There have been recent studies on using perovskite

structures (such as LSMO) [102] as the magnetic layer to achieve ME coupling, but there has not been a breakthrough discovery yet for room temperature multiphase ME coupling. *In chapter 7, we present evidence of room temperature ME coupling of amorphous FDTO with BFO.*

1.3 Goals of thesis

Prior to the start of this research, the only known amorphous conducting oxides all followed Hosono's rule, and very little exploration was performed on materials not falling within the Hosono rule. This has created a gap in the understanding of amorphous oxide semiconductors established in literature. To obtain a better understanding, the conduction, optical, and magnetic studies were conducted of the FDTO amorphous oxide materials, as elaborated in chapters 3, 4, 5 and 6.

In this thesis we synthesized thin films of amorphous Fe-Tb-Dy-oxide and characterized their electrical, optical and magnetic properties as a function of cation stoichiometry, and oxygen content, to gain better understanding of the conduction mechanism in this new class of oxide materials. Building on previous work on magneto-electric coupling for multiferroic devices, we have investigated the application of this novel Fe-Tb-Dy-oxide for magneto-electric coupling with bismuth ferrite for use in memory device. The bulleted list summarizing the remainder of the thesis content is provided here.

- Chapter 2 details the various experimental methods and characterization techniques used throughout this thesis
- Chapter 3 summarizes the discovery of this material in 2015, which has been already published in Scientific Reports
- Chapter 4 discusses the effects of varying Fe:Tb+Dy ratio on the electrical, optical, and magnetic properties of the thin films
- Chapter 5 describes results of a cyclic annealing study on a thin film of FDTO having Fe:Tb+Dy value of 21
- Chapter 6 describes the effects of varying oxygen content on the electrical, optical, and magnetic properties of the FDTO thin films
- Chapter 7 describes investigation of using FDTO for magneto-electric coupling with BFO
- Chapter 8 summarizes the thesis and highlights further studies that need to be done on FDTO

Chapter 2

Methods and techniques

The various experimental techniques used to synthesize the FDTO thin films, and the characterization techniques used to investigate its chemical composition, microstructure, transport, optical, and magnetic properties are detailed in this chapter.

2.1 Synthesis and annealing techniques

2.1.1 Substrate selection and preparation

Substrates were selected keeping in mind that transport, optical, and magnetic measurements need to be done on the samples. Therefore quartz was the preferred substrate, followed by SiO_2 (400 nm, thermally grown)/ Si for reduced charging in scanning electron microscope (SEM) and energy dispersive spectroscopy (EDS). The substrates were cleaned by sonicating in acetone, isopropanol, and DI, then dried with N_2 air gun. They were typically mounted on sample holder prior to deposition using double-sided carbon tape or regular tape.

For the ME coupling work, substrates were $SrTiO_3$ (STO) (001) on which epitaxial $SrRuO_3$ (SRO) (20-30 nm) and $BiFeO_3$ (BFO) (50-100 nm) were deposited. STO is typically the preferred substrate for growing BFO films due to the match of their lattice parameters. SRO is needed as a bottom electrode for applying a voltage bias across BFO in devices. These samples were also cleaned using above protocol.

2.1.2 Pulsed laser deposition

Pulsed laser deposition (PLD) has been used to grow stoichiometric thin films of materials from solid sources (or targets) to the substrates. The technique dates back to 1965 where thin films of semiconductors and dielectric materials were deposited using a ruby laser [103]. Between 1969 to 1987, stoichiometric thin films of STO, $BaTiO_3$, Ni_3Mn, $ReBe_{22}$, and other superconducting materials were successfully grown [103]. Since then PLD has been used to deposit thin films of several oxides, metals, superconductors, semiconductors, and dielectric materials. A summary of the PLD technique and mechanism is described below; however, a more in-depth discussion of this deposition method can be found in the review article by Boyd [104] and progress article by Christen and Eres [103].

The technique of pulsed laser deposition is quite simple, and is demonstrated in the schematic in Fig. 2.1. A laser beam repeatedly hits a target material that is mounted on a rotating holder - this makes sure the beam does not hit the target at the same spot all the time, as that would eventually change the surface stoichiometry in addition to causing a significant surface deformation that will change the deposition uniformity. When the first laser pulse hits the target, the energy from the laser pulse excites the electrons on the surface of the target. The electrons then relax in the order of pico-seconds, releasing energy into the lattice in the same time scale. This is followed by heat diffusion into the lattice, which is much slower in the order of micro-seconds. However, melting happens at the surface at a much faster rate (in the order of nano-seconds), followed by evaporation of species into the plume in micro-seconds and consequent resolidification of the surface. The much faster surface melting compared to the heat diffusion into the lattice enables the formation of the plume that maintains stoichiometry. As soon as the surface resolidifies, the second laser pulse hits the target surface, starting this process all over again.

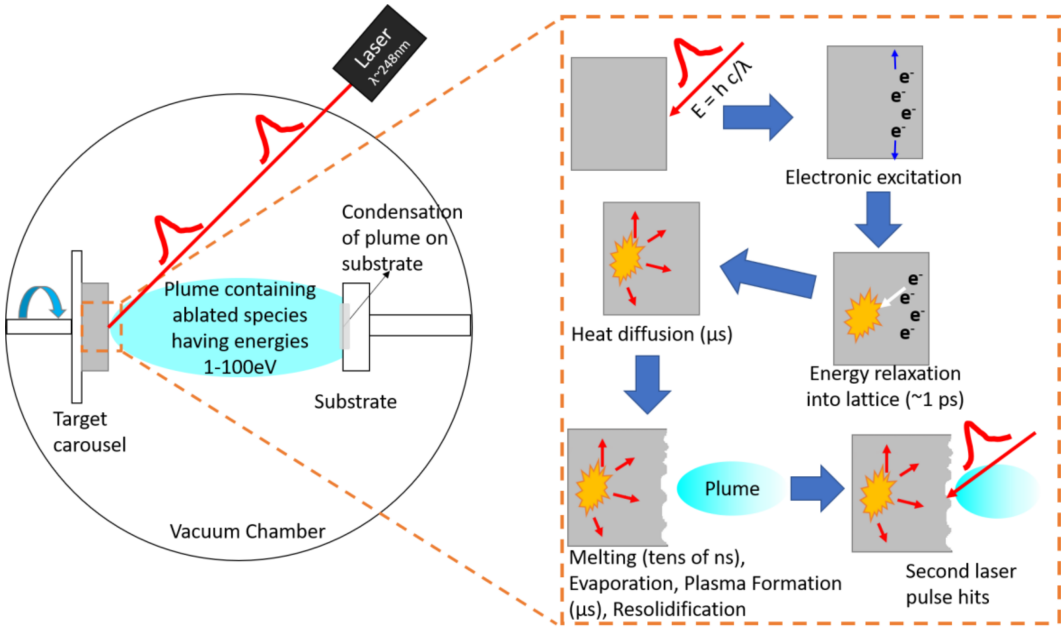


Figure 2.1: *Schematic showing the mechanism of thin film deposition by PLD.*

The plume, which contains species having energy from 1-100 eV, travels to the substrate where material gets deposited by condensation. The shape of the plume can vary depending on the pressure inside the chamber. This is explained nicely by Boyd in his review article [104] - when the pressure is high, the plume is prevented from expanding too much, leading to a pressure front, plasma attenuation, and reactive collisions; in contrast, when the pressure is low, the plume is able to undergo 3-D expansion with very little attenuation.

The temperature of the substrate plays an important role in the microstructure of the resulting thin film, and the phases that it contains, because it determines the adatoms' surface diffusion ability. At high substrate temperatures, the adatoms in the plume have higher surface diffusion ability, and so they can rearrange to form a more ordered structure. On the other hand, if the substrate is at room temperature, the adatoms have

lower diffusivities and lead to films with a higher degree of disorder, including the enhanced possibility to form amorphous films. Therefore to obtain high quality crystalline films, the substrates are typically kept at elevated temperatures.

One of the main constraints of PLD is that due to the elliptical shape of the plume, uniform deposition takes place only on a very small area that is close to the plume center. This is typically not more than a square of 1 cm^2 in a lab PLD system. However, companies such as Neocera have managed to develop techniques to increase the uniform deposition area to circles of 200 mm in diameter [105].

In this thesis, two PLD deposition systems were used - (i) at University of Tennessee-Knoxville (UTK) for the initial discovery of FDTO (ii) at University of California-Berkeley (UCB) for systematic study of FDTO as a function of varying oxygen pressure during growth. In both systems the target materials were kept the same, i.e., commercially available Terfenol-D (TD) target [106], which is a metal alloy target composed of 66% Fe, 24% Dy, and 10% Tb. While the target at UTK was a disc having thickness of about 5 mm, and diameter of about 1 cm, the target used at UCB was a disc of 1 inch diameter and 0.25 inch in thickness. The second difference is that prior to each deposition, the target at UCB was polished using sandpaper to create a smooth surface - this was not done at UTK. The laser specifications and deposition parameters used for PLD growth for both systems are listed in Table 2.1. All depositions were done by keeping the substrate at room temperature.

Table 2.1: *List of PLD parameters*

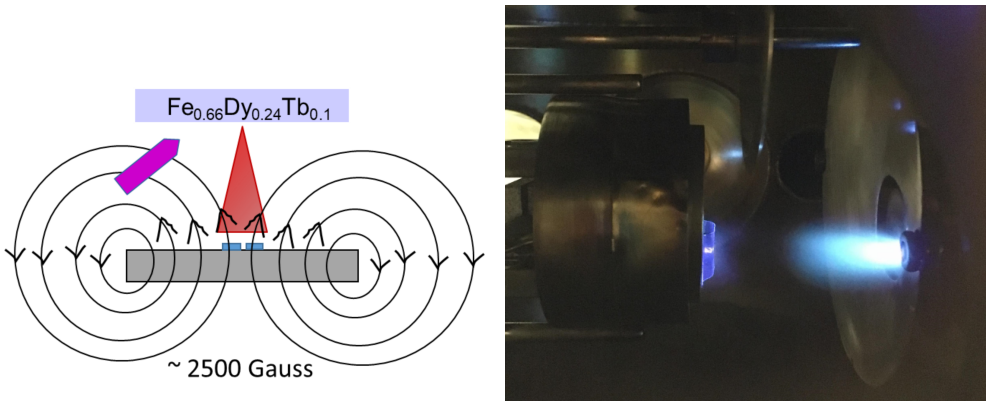
	Laser type, wavelength, energy density	Repetition Rate	Oxygen pressure during growth
Initial discovery (at UTK)	Nd:YAG, 266 nm, 0.56 J/cm^2	50 Hz	$5x10^{-8}$ Torr
Systematic study (at UCB)	KrF excimer, 248 nm, 1 J/cm^2	10 Hz	$5x10^{-7}$ to $1x10^{-3}$ Torr

Details of results obtained at UTK are discussed in chapter 3 and those obtained from films grown at UCB are discussed in chapter 6.

B-field assisted PLD growth

The final part of this thesis was to achieve magneto-electric (ME) coupling of FDTO with BFO. Initially thin films (3 - 7 nm) of FDTO were deposited on BFO and checked for magnetic coupling, which is evident by an enhanced coercive field of the FDTO on BFO compared to on quartz. However, it proved difficult to get repeated coupling behavior. To optimize magnetic coupling of FTDO to BFO, B-field assisted PLD was carried out, where substrates were placed on top of a small permanent magnet with out-of-plane (OOP) magnetic field of about 2500 Oe. Everything else in the PLD process was kept the same. The schematic of this process and a photo showing plume shape in the presence of B-field is shown in Fig. 2.2

The substrates used for ME coupling were BFO/SRO/STO. The BFO and SRO layers were deposited by collaborators at UCB. The laser parameters used for that growth are summarized in table 2.2.



(a) (b)

Figure 2.2: *(a) Schematic of B-field assisted PLD growth showing substrates on top of a permanent magnet, the out-of-plane magnetic field lines, the laser hitting the Terfenol-D target, and the resulting plume depositing on top the substrates. (b) Photo of the PLD plume (blue) from Terfenol-D target getting deposited on quartz substrate mounted on top of permanent magnet with double-sided tape.*

Table 2.2: *List of PLD parameters for PLD growth of BFO and SRO*

	Laser type, wavelength, laser energy density	Repetition Rate	Oxygen pressure during growth, Substrate temperature
BFO	KrF excimer, 248 nm, 100mJ	5 Hz	$1x10^{-3}$ Torr, $900°C$
SRO	KrF excimer, 248 nm, 90mJ	15 Hz	$1x10^{-3}$ Torr, $900°C$

2.1.3 Electron-beam evaporation

Electron-beam (e-beam) evaporation is used to deposit dense, high purity thin films. In this technique, current is passed through a tungsten filament which leads to joule heating and emission of electrons. By applying a high voltage between the filament and the hearth, the emitted electrons are directed towards a crucible holding solid nuggets or ingots of the material to be deposited. When the electrons reach the material inside the crucible, their energy is transferred to the material, causing the material to evaporate (or sublimate). The evaporated material then travels through the vacuum and gets deposited on the substrate. More elaborate details of this technique can be found on the website of Angstrom Engineering [107], and in the book chapter by Wang and Zhang [108].

In this thesis, a Mantis QUAD-EV-HP e-beam source was used for deposition of (i) FDTO films of different ratio, R, of Fe: (Tb+Dy), and (ii) Ag films to be used as contacts for electrical measurements. For the FDTO films, crucibles containing Fe and TD were evaporated simultaneously. Prior to co-evaporation, the deposition rates of both targets were calibrated using thickness measurements made using MFP-3D Atomic Force Microscope from Asylum Research. The different R values were obtained by changing the

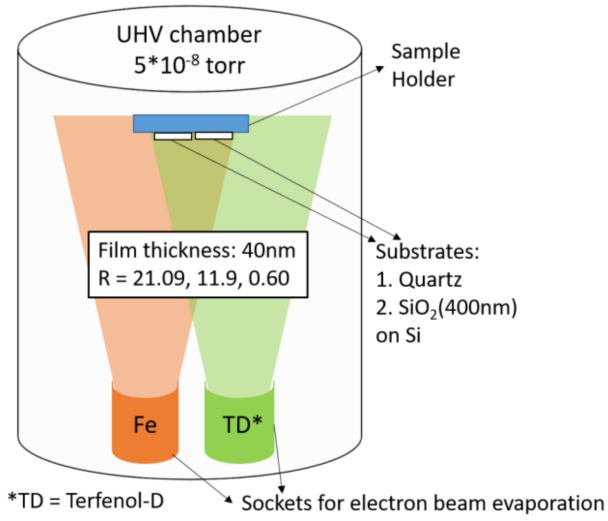


Figure 2.3: *Schematic of co-deposition by e-beam evaporation.*

deposition rates of the two targets. The schematic of co-deposition from two targets is shown in Fig. 2.3.

For Ag contact deposition, the substrates were first masked using aluminum foil and then about 60 nm of Ag was deposited using the e-beam. All depositions were done at pressures of 2×10^{-8} to 6×10^{-8} Torr.

Results of the as-prepared samples deposited by e-beam evaporation are discussed in chapter 4.

2.1.4 Capacitors and GMR device fabrication

2.1.4.1 *Capacitor fabrication*

For the FDTO/BFO work, capacitors needed to be fabricated to investigate the robustness of using FDTO as a a top electrode for BFO. Capacitors were fabricated by first depositing a uniform layer of ~60 nm Pt by RF magnetron sputtering. After that a mask of an array of circular capacitors having diameter of 8, 16, 32, and 64 μm were created using photoresist. After the photoresist was developed, the layers of Pt and FDTO were removed using ion milling, resulting in array of capacitor devices. This process is demonstrated in Fig. 2.4

2.1.4.2 *Giant-magnetoresistance (GMR) device fabrication*

GMR devices were fabricated on the FDTO/BFO samples to show evidence of ME coupling between FDTO and BFO. A GMR device has two ferromagnetic (FM) layers and a non-magnetic (NM) conductor sandwiched between the two FM layers. When the spin of the top FM layer is opposite to the spin of the bottom FM layer, there is going to be an increase in the resistance of the device - this is seen as the GMR signal. Therefore, to be able to see a GMR signal, the coercive field of the bottom FM layer must be different from the top FM layer.

The first hypothesis was making a GMR device with the following layers (from top to bottom): CoFe/ Cu/ FDTO/ BFO/ SRO/ STO. CoFe has a coercive field of about 20 Oe [109], and FDTO coupled to BFO was found to have coercive field of >100 Oe. Therefore a GMR signal should be evident in this heterostructure.

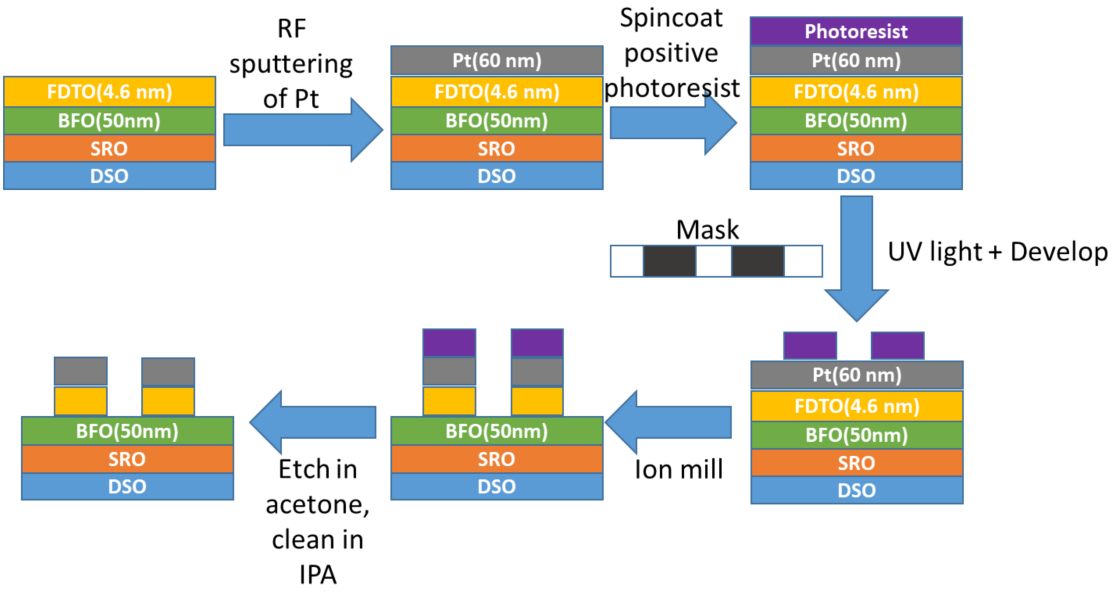


Figure 2.4: *Schematic showing the fabrication of FDTO/BFO capacitors.*

However, the conductivity of CoFe and Cu layers are three orders of magnitude higher than the FDTO layer, and therefore would short the device.

Therefore the final heterostructure was designed to be: Pt(60 nm)/ CoFe (2.5 nm)/ Cu(5 nm)/ CoFe(2.5 nm)/ FDTO(4 nm)/ BFO(100 nm)/ SRO(25 nm)/ STO. The bottom CoFe should be able to couple to the FDTO and the resulting coercive field of the bottom CoFe should be increased to >100 Oe as well. In this way the GMR signal can be measured resulting from magnetic coupling of the FDTO/BFO layers without having the device shorted.

The GMR devices were fabricated by Dr. Bhagwati Prasad at UCB using a combination of photolithography, RF sputtering of the Pt, CoFe, and Cu layers, and ion milling. The lateral dimension of the device was about 100 μm, while the device width was about 20 μm. Contacts were made by careful wirebonding to the Pt contact pads. The schematic of a GMR device is shown in Fig. 2.5

2.1.5 Annealing

2.1.5.1 *Furnace annealing*

FDTO films deposited by PLD at UTK were annealed inside a furnace from MTI corporation (model no.: OTF-1200X) at 500°C for 2 hours in ambient atmosphere and in nitrogen (99.9% purity of N_2 gas supplied by Airgas Inc., Knoxville, USA) to investigate crystallization and effects of annealing on the electrical and optical properties of the film. *The results of this annealing study are discussed in chapter 3* .

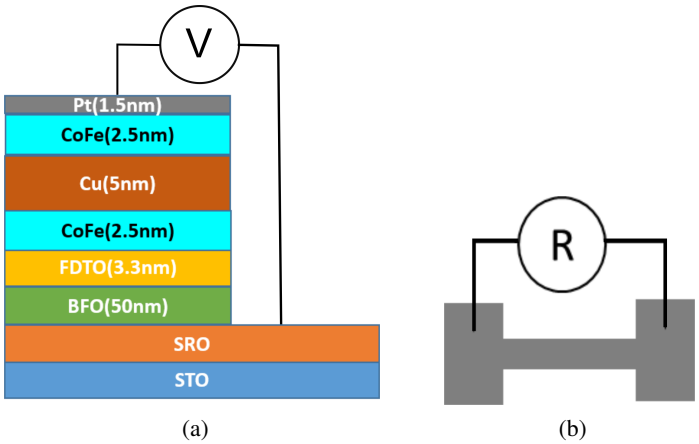


Figure 2.5: *(a) Schematic of the cross-section of FDTO/BFO GMR device (b) Top view of the GMR device.*

2.1.5.2 *Cyclic annealing*

FDTO film of R=21 was annealed through thermal cycles while measuring in-situ resistivity of the film. This processing step was performed by Prof. Tatiana Allen at University of Tennessee-Chattanooga using programmable Hall Measurement System from MMR Technologies, Inc. A flowchart of each anneal cycle is shown in Fig. 2.6: the sample was heated from 300 K to 700 K at 5 mTorr at a rate of about 3 K per minute. At each temperature value, the resistivity of the sample was measured using the Van der Pauw technique, described in the next section. Once the sample reached 700 K, it was cooled down to 300 K at the same rate of ~3 K per minute. This was repeated till such time that the resistivity stabilized, in this case 14 cycles. During the 14th cycle, Hall mobility and carrier concentration were also measured. *Results of this annealing cycle process are discussed in chapter 4.*

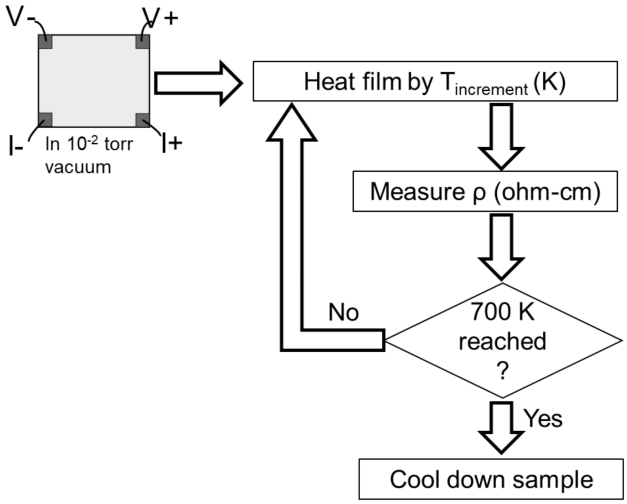


Figure 2.6: *Flowchart showing one cycle of annealing of the sample with R = 21 in 5 mTorr; 14 such cycles were performed on the sample.*

2.2 Characterization techniques

2.2.1 Physical properties

2.2.1.1 *Microstructure & surface morphology*

- **Scanning electron microscopy (SEM)**: After deposition of the thin films using PLD and e-beam evaporation, they were characterized for their surface morphology and particulate density using SEM. Zeiss Merlin SEM was used for this purpose - EHT voltage of 10 kV was used on more conductive films, while EHT of 3 kV was used for more resistive films and those that were deposited on quartz substrates to avoid charging. Both in lens and secondary electron detectors were used.

- **Atomic force microscopy (AFM)**: AFM was used for two purposes - (i) to characterize the thickness and roughness of the films deposited by PLD and by e-beam evaporation, and (ii) to calibrate the deposition rate for the different e-beam targets. An MFP-3D AFM by Asylum Research was used for all measurements, and was operated in non-contact mode. For thickness measurements, a step was typically created from the substrate to the top of the film by masking a portion of the substrate during film growth. A line profile across the step gave the thickness of the film. Fig. 2.7 shows a typical step height measurement obtained for a 7 nm FDTO film deposited by PLD at UTK.

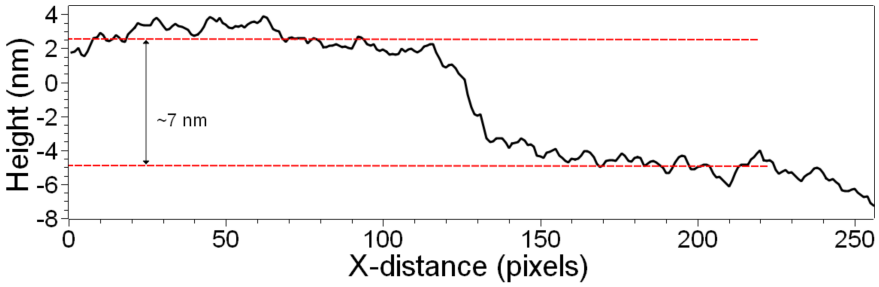


Figure 2.7: *Plot showing a typical step height measurement obtained using AFM for measuring film thickness.*

- **Grazing incidence X-ray diffraction (GIXRD):** As-deposited and annealed films of FDTO, deposited both by PLD and e-beam evaporation, were characterized by GIXRD to investigate whether the films were amorphous or crystalline. A Panalytical X'Pert3 MRD X-ray diffractometer equipped with Cu Kα source (1.54059 Å) radiation and a Xe-proportional detector was used for these measurement (same instrument was used both at UTK and at UCB). The GIXRD patterns were recorded in a 2θ scanning mode using a parallel beam mirror on the incident beam side and a parallel plate collimator of 0.27 divergence on the diffracted beam side. A combination of beam mask and divergence slits was selected to illuminate the sample surface without illuminating the sample holder. The GIXRD patterns were collected in the 2θ range between 10-90° with a step size of 0.02° and step time of 7 sec/step using an omega value of 0.5.

- **X-ray reflectivity (XRR):** XRR was performed on the films deposited by PLD at UCB using the same Panalytical X'Pert3 MRD X-ray diffractometer in order to measure the thickness and density of the FDTO films. A slit of 1/16 was used on the beam side to optimize reflectivity signals. Fitting of the XRR fringes were done using the reflectivity software that came with the instrument.

- **Transmission electron microscopy (TEM):** The microstructure of the as-deposited and annealed FDTO films were further investigated in TEM to look for the presence/absence of any nanoclusters. High resolution TEM images and diffraction patterns were taken in a Zeiss Libra 200MC at an acceleration voltage of 200 kV, while the Z-contrast images and EELS spectra were taken with an aberration corrected (Nion, Inc.) dedicated STEM VG 501 UX operated at 100 kV. This instrument is equipped with a cold field emission electron source and a Gatan Enfina EELS spectrometer. In addition, Ultra-STEM 200 at the Center for Nanophase Materials Science at Oak Ridge National Lab was also used for imaging and EELS analysis.

2.2.1.2 *Chemical composition*

- **Scanning TEM (STEM):** The chemical composition and distribution of the various cations at an atomic level were investigated using STEM. This was done in a Zeiss Libra 200MC, where Z-contrast images and EELS spectra can be taken using an aberration corrected (Nion, Inc.) dedicated STEM VG 501 UX operated at 100 kV. The instrument also has a cold field emission electron source and a Gatan Enfina EELS spectrometer. For some of the films, low loss EELS spectra were obtained to look at the bandgap edge in order to get more insight into the transport behavior of the films. In addition, Ultra-STEM 200 at the Center for Nanophase Materials Science at Oak Ridge National Lab was also used for imaging and EELS analysis.

- **Energy dispersive X-ray spectroscopy (EDS):** EDS was used to quantify the ratio of Fe:Tb+Dy in the films prepared by e-beam evaporation and having different elemental compositions. The EDS detector by Bruker was available with the Zeiss Merlin SEM, and the Bruker software was used to quantify the spectra.

- **X-ray photoelectron spectroscopy (XPS)**: The as-prepared and annealed FDTO films were characterized by XPS to look at the cation states near the surface of the film. However, two different XPS systems were used for this. For the films deposited by PLD at UTK, XPS measurements were done by Dr. Arthur Baddorf at Oak Ridge National Laboratory using a SPECS Focus 500 monochromated Al Kα X-ray source operated at 380 W and a SPECS PHOIBOS-150 hemispherical electron analyzer at normal emission and 40 eV pass energy. Relative atomic concentrations were taken from comparison of Dy 3d, Tb $3d_{5/2}$, O 1s, and Fe $2p_{3/2}$ core levels, analyzed and corrected for sensitivity and transmission factors in CasaXPS software. For all other films, XPS measurements were done by Dr. Tamil S. Sakthivel, our collaborator at University of Central Florida, who measured the spectra at room temperature in an ion-pumped chamber (evacuated to 2×10^{-9} Torr) of an PE-PHI5400 spectrometer, employing Al-Kα radiation (BE = 1486.6 eV) of about 4 mm spot size. The binding energy (BE) for

the samples was calibrated by setting the measured BE of C 1 s to 284.6 eV. Peakfit software was further used to identify the chemical state of multifaceted Fe 2p, Dy Tb 4d and O1s spectra according to the previous reports. XPS measurements were also done at UCB by Mark Hettick to measure the work function of the as-prepared films deposited at UCB. The system was a Kratos AXIS Ultra system which has a monochromatic Al K-alpha source, with a hemispherical analyzer. A charge correction to C 1s peak was applied during data fitting.

2.2.2 Optical properties

Ultra-violet-Visible (UV-Vis) transmission spectra were obtained for all thin films deposited on quartz using an Ocean Optics spectrometer with a He-Ne light source that allowed measurements to be made between 300 nm to 900 nm, with integration time of 1 ms and 100 scans to average. The beam spot size had a diameter of 1 mm. Transmission spectra were acquired at five different locations of each sample to ensure homogeneity of the film thickness. Tauc plots for were generated by first converting the transmission values (% T) to absorbance using Beer-Lambert's law and then dividing by the film thickness to get the absorption coefficient as a function of the probing wavelength. The relevant equations are given below:

$$Abs = ln\left(\frac{100}{T\%}\right) \tag{2.1}$$

where Abs is the absorption and T% is the percentage transmission.

$$\alpha = \frac{Abs}{t} \tag{2.2}$$

where α is the absorption coefficient.

The Tauc plot was made with y-axis as $(\alpha h\nu)^{1/m}$ as a function of $h\nu$ (the wavelength in energy units). A tangent was drawn at the region of the plot with sharp increase, which was then extrapolated to cut the x-axis at the band-gap value; m = 1/2 was used to obtain a direct band gap value and m = 2 was used to obtain indirect bandgap value assuming bands are parabolic.

2.2.3 Transport properties

2.2.3.1 *Van der Pauw measurements*

(taken from "Methods" section of Malasi et al. [1] because it was written by H.T.)

For measuring the electrical properties, silver pads were deposited on the four corners of the sample using e-beam evaporation, as described previously. Gold wires were then attached to the silver pads using silver epoxy paste. A Keithley 2400 sourcemeter was used to measure the sheet resistance and the hall mobility of the deposited amorphous oxide. Sheet resistance was measured using the Van der Pauw method, where probe contacts are made at the four corners of the sample. Current was supplied at two adjacent contact points while voltage was measured at the two remaining contact points, i.e. if the four contacts were numbered 1, 2, 3, and 4, current was supplied between 1 and 2 (I_{12}), while voltage was measured between 4 and 3 (V_{43}) to get resistance $R_{12,43}$. In this way, the current direction was changed to cover all four sides,

making sure to reverse the current direction on each side, resulting in eight total measurements. The four-probe resistance was measured by the Keithley sourcemeter working in 4-wire sensing mode. A LabVIEW code was written to collect data from the Keithley for 1 minute and then display the average value. This method of data collection ensured noise-compensated resistance values. After all the eight resistance values were measured ($R_{12,43}$; $R_{21,34}$; $R_{34,21}$; $R_{43,12}$; $R_{41,32}$; $R_{14,23}$; $R_{23,14}$; $R_{32,41}$), the following formula was used to calculate the sheet resistance:

$$\exp(-\pi R_A/R_S) + \exp(-\pi R_B/R_S) = 1 \tag{2.3}$$

where R_A = ($R_{12,43}$ + $R_{21,34}$ + $R_{34,21}$ + $R_{43,12}$)/4, R_B = ($R_{41,32}$ + $R_{14,23}$ + $R_{23,14}$ + $R_{32,41}$)/4, and R_S is the sheet resistance. The resistivity was calculated as the product of the sheet resistance and the film thickness.

Hall measurements were made by supplying current along the contacts 3 and 1, and measuring the voltage between 4 and 2. For each value of current, the magnetic field was varied and the corresponding Hall voltages were measured. Just like for sheet resistance measurements, a LabVIEW program was used to collect data to compensate for noise and drift. A plot was then made of Hall voltage vs applied magnetic field and a straight line fit was applied to it to obtain the slope of the plot. The hall mobility, μ, was then calculated using:

$$\mu = (\frac{dV}{dB})\frac{1}{IR_S} \tag{2.4}$$

where I is the current supplied and R_S is the sheet resistance. The process was repeated with at least three different current values to obtain reliable Hall mobilities. The carrier concentration, n, was calculated as

$$n = \frac{1}{e\mu\rho} \tag{2.5}$$

where e is the charge on an electron, and ρ is the resistivity.

Sheet resistance was also measured as a function of temperature for the PLD films deposited at UTK using Keithley 2400 sourcemeter. Although the same 4-wire sensing mode was used as for sheet resistance measurement, the contacts for current supply and voltage measurement were fixed to one configuration so as to not disturb the system while the film was being heated with an IR lamp. The temperature was measured periodically using a laser temperature sensor and the corresponding resistance value was noted from the sourcemeter.

2.2.3.2 *Low temperature resistance*

Resistance of the films from 3 K to 300 K were measured using PPMS systems. Two PPMS systems were used, one at UTK and the other one by the group of Prof. A. Tiwari, a collaborator at the University of Utah.

The temperature dependence of resistance and magneto-resistance measurements were performed at the University of Utah in a helium cooling cryostat. The sample was mounted in the cryostat which is connected to a temperature controller (Lakeshore 335), a current source (Keithley 6220) and nanovoltmeter (Keithley 2182A). The electromagnet was powered by KEPCO bipolar optional power supply. The measurements

were operated by LabVIEW program which controlled the current input, voltage measurement, the applied magnetic field, and temperature setting.

Temperature and field dependent resistivity and hall effect measurements at UTK were made with the help of Dr. Rupam Mukherjee using a Quantum Design Physical Property System. High purity silver epoxy from SPI Supplies and gold wires of 25 μm diameter were used as contact electrodes and wiring respectively. Measurements were made using the Van der Pauw configuration as described above to eliminate contact resistance at the sample-electrode interface, at intervals of 5 K. Hall mobility of the films were measured up to 5 Tesla to look for anomalous hall effect.

2.2.3.3 *High temperature resistance and hall mobility*

Resistance of the film with R=21 was measured in-situ as a function of temperature from 300 K to 700 K in 5 mTorr pressure using the Hall measurement system by MMR technologies, as described in section 2.1.5.2.

2.2.3.4 *Photoconductivity*

Photoconductivity measurements were made by Dr. Hernando Garcia at the Southern Illinois University-Edwardsville to probe conduction mechanism and electrical bandgap. The photoconductivity setup was designed to study the photoconductance response of the sample as sample is illuminated with monochromatic light. A phase sensitive technique was used that permitted the detection of very small currents. The experimental setup is shown in Fig. 2.8. The light from a CERMAX Xenon fiber optics light source is passed through a CM110 1/8m monochromator that is controlled through a RS-232 port, using a computer running LabVIEW. The program scanned wavelengths from 300 nm-900 nm. Light was first passed through the monochromator, then was modulated with a chopper from Stanford Research, at a frequency of 100 Hz. The output signal of the chopper was used as the reference signal for a Stanford Research SR830 look-in amplifier. The lock-in amplifier served a number of purposes: first, it used the reference frequency created by the optical chopper to reduce the effects of AC noise; second, it amplified the signal from a resistor to a range of 0 to 10 V, even if the signal was in the microvolt range. Finally, the lock-in amplifier contained an ADC (analog-to-digital converter) that allowed it to transfer the measured signal to the computer. It is worth mentioning that the signal out of the lock-in amplifier contained a DC-component, and an AC component with the same modulation frequency as the chopper. By mixing the signal through the local oscillator in the SR830, the DC component and other sources of noise were eliminated. Finally the light was focused with a microscope objective of 20X and focused on the sample. The sample was connected to a battery and a load 20 kΩ resistor, the voltage across the resistor is fed into the input port of the lock-in amplifier.

2.2.4 Magnetic Properties

2.2.4.1 *Superconducting quantum interference device (SQUID)*

SQUID was used mainly to measure magnetic moment as a function of magnetic field, with field both in-plane (IP) and out-of-plane (OOP) with respect to the plane of the sample. The system used was a Quantum Design Magnetic Property Measurement System using brass as a sample holder at UTK, and plastic drinking

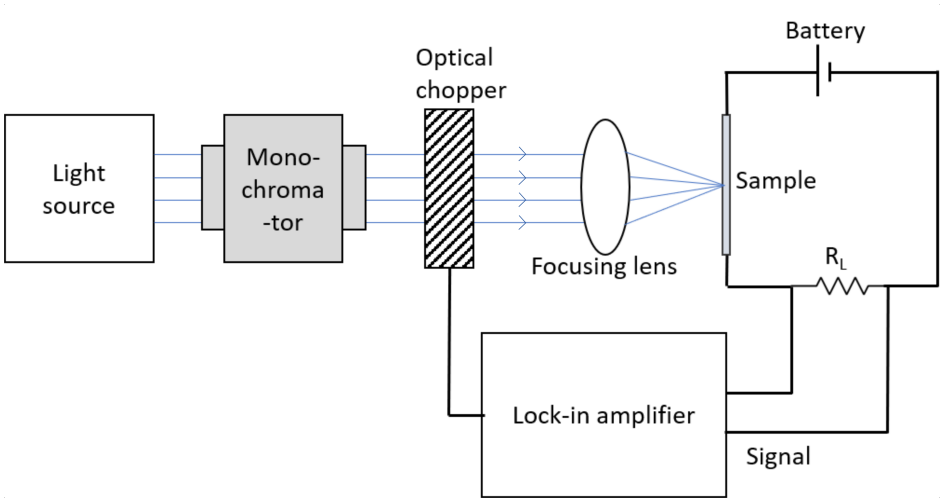


Figure 2.8: *Schematic of phase-sensitive photoconductivity set-up.*

straw as sample holder at UCB. Magnetic fields of up to 5 Tesla were supplied for these measurements. Samples on quartz typically contributed to a diamagnetic background signal, which was subtracted to get the saturation magnetization for the FDTO films.

Magnetic moment as a function of temperature were also measured for the as-prepared films having different R values using a vibrating sample magnetometer by our collaborator at North Carolina A&T State University.

All samples for magnetic measurement were handled using non-magnetic, teflon tip tweezers to prevent magnetic impurities.

2.2.4.2 *Magnetoresistance (MR)*

- **Normal MR:** MR of as-prepared and annealed thin films deposited by e-beam evaporation were measured by Dr. Tiwari's group at the University of Utah, in the Van der Pauw configuration, using the same system that was used for low temperature resistance measurement. In addition, MR of thin films deposited by PLD at UCB were measured using a home-built measurement system at UCB. The system used an electro-magnet that was capable of going up to 6000 Oe, a Keithley 6221 for supplying AC current, and a Stanford SR865A lock-in amplifier to measure the voltage. A LabVIEW program was developed to interface with all the instruments, and collect, plot and save data. The contacts were made by wirebonding Ag contact pads on the samples to contact pads on a chip holder that was used to mount the sample at the center of the magnetic field. The magnetic field was supplied IP to the plane of the sample for this measurement.

- **Anomalous MR (AMR):** AMR was measured using at UCB the same measurement system as described above. The only difference is that a servo motor was used to rotate the stage for measuring MR at different angles. A LabVIEW program was also developed to control the servo motor and specify the angle of rotation of the stage. A constant magnetic field was supplied IP for this measurement.

- **Giant MR (GMR):** GMR signal of the devices described in section 2.1.4.2 were measured using the same home-built system at UCB as described in the normal MR section. Magnetic field was supplied IP with respect to the plane of the sample. In addition, a Tektronix signal generator was used to customize pulse voltages to be supplied as bias across the BFO thin film. A Keithley 6517a was also used for this purpose to supply a constant DC voltage when needed.

2.2.4.3 *Surface magneto-optic Kerr effect (SMOKE)*

SMOKE measurements were performed on as-prepared and annealed films deposited at UTK by PLD and by e-beam evaporation to check for room temperature magnetism in the films. The SMOKE system is home-built, and the schematic of the system is shown in Fig. The measurements were made in longitudinal mode using a s-polarized laser beam of 633 nm wavelength making 12.6° angle of incidence with the normal to the substrate plane. However, it was later discovered that there is a limit to the sensitivity of the system as some of the films did not show any SMOKE signal but exhibited weak room temperature magnetism in SQUID.

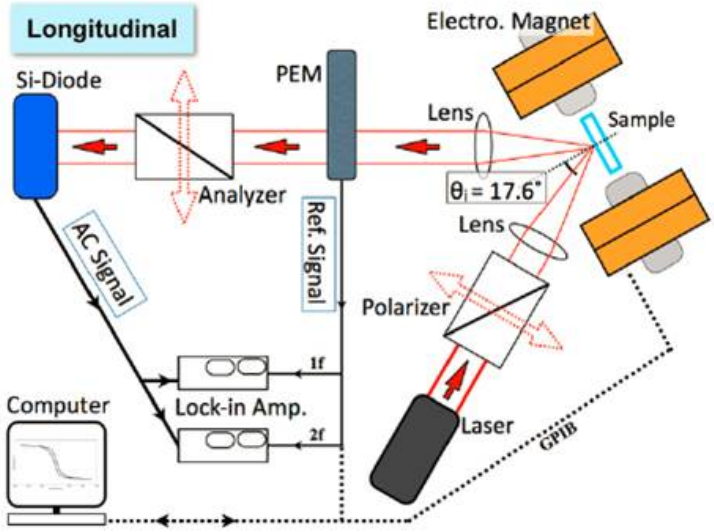


Figure 2.9: *Schematic showing the SMOKE setup for making longitudinal measurements on the FDTO thin films [110].*

2.2.5 Ferroelectric hysteresis and fatigue test

Ferroelectric hysteresis measurements were made on the FDTO/BFO capacitor devices described in section 2.1.4.1. Ferroelectric measurement system supplied by Radiant Technologies Inc. at UCB was used for this purpose. The top and bottom electrode contacts were made using a probe station. Drive voltage of upto 10 V was supplied at 200 kHz to make the measurements. This system was also used for doing fatigue testing on the capacitors, where upto 10^8 cumulative switching cycles were applied to the devices, and the polarization was measured after every certain number of cycles.

2.3 Acknowledgments

TEM work at UTK was done by Dr. Gerd Duscher and Chenze Liu at UTK, and Shang-Lin Hsu at UCB. XPS work was done initially by Dr. Arthur Baddorf at Center for Nanophase Materials Science (CNMS) at Oak Ridge National Lab (ORNL, TN, USA), and later mostly by Dr. Tamil S. Sakthivel at University of Central Florida; some XPS and work function measurements were done by Dr. James Bullock and Mark Hettick at UCB. Photoconductivity measurements were made by Dr. Hernando Garcia at Southern Illinois University-Edwardsville. GMR device fabrication was done by Dr. Bhagwati Prasad at UCB, and ion milling for capacitors was done by Dr. Charles Henri-Lambert at UCB. There was assistance from Dr. Rupam Mukherjee and Krishna Koirala for PPMS and SQUID measurement at UTK. SQUID at UCB was done by Dr. Bhagwati Prasad and Dr. Vishal Thakare. Ruijuan Xu helped with ferroelectric measurements at UCB. Low temperature resistance and some MR measurements were done by Kun Tian and Dr. Ashutosh Tiwari at the University of Utah. Nana K. Yamoah from North Carolina A&T State University did some of the magnetic measurements.

Chapter 3

Discovery of a novel, amorphous Fe-Dy-Tb-oxide (FDTO) with high optical transparency, conductivity, and mobility

(Modified with permission from Abhinav Malasi, Humaira Taz, Annette Farah, Maulik Patel, Benjamin Lawrie, Raphael Pooser, Arthur Baddorf, Gerd Duscher and Ramki Kalyanaraman, *Scientific Reports*, **2015**, accepted. Copyright 2015 Nature Publishing Group)

3.1 Summary

In this chapter, we report the discovery of Fe-Tb-Dy-oxide, an amorphous ternary oxide of the form Me_2O_3 (where Me = 66% Fe, 24% Dy, and 10% Tb), that showed unexpected functional properties. The amorphous microstructure and homogeneous cation distribution were confirmed by GIXRD and TEM, and EELS measurements respectively, which were stable upto 500^{o}C. The thin films were found to be optically transparent with a bandgap of ~2.85 eV. Transport measurements revealed the films to have very high conductivity (>5x10^4 S/m) and hall mobility (~30 cm^2/V-s) in ambient conditions. Since this material shows significantly different transport behavior from its constituent oxides, which are insulating in ambient conditions, it could point to a new class of oxide materials made from elements with unfilled d and f-orbitals that exhibit transport and optical properties desirable for applications in electronic devices. This discovery was the beginning of the investigations on various properties and potential applications of FDTO to be pursued in this thesis.

3.2 Methods

Details of PLD growth of the FDTO thin films and characterization techniques can be found in chapter 2. The characterization methods used in this chapter are listed below:

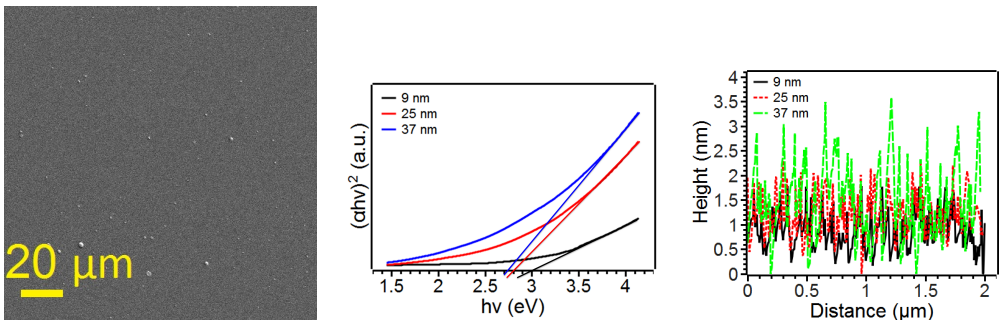
- SEM and AFM for surface characterization

- TEM (including EELS), XPS, and XRD for material characterization
- UV-Vis transmission spectroscopy and Tauc plot analysis for optical properties
- SMOKE measurement for magnetic properties
- Van der Pauw sheet resistance and hall mobility measurement at room temperature; resistance as a function of temperature from 300 K to 500 K using IR lamp

3.3 Results

Interest in the well-known magnetostrictive, commercially available material Terfenol-D (TD; metal composition of 66% Fe, 24% Dy, and 10% Tb) stemmed from its potential magneto-optic applications. Thin films (9 nm - 75 nm) of TD were deposited on quartz and SiO_2/Si substrates by PLD using the metal alloy TD target (purchased from Etrema [106]). Details of the PLD deposition parameters can be found in chapter 2.

Upon examining the as-prepared (AP) thin films, they appeared optically transparent to the naked eye as can be seen in Fig. 3.2(a) for the sample marked AP. To investigate the optical properties further, UV-Vis transmission spectra were obtained for the AP films for a range of thicknesses, as shown in Fig. 3.2(b). All the films were found to have greater than 50% transmission in the UV to NIR range (i.e. 1.5 to 4eV), with the 9 nm film exhibiting >90% transmission in that range. To confirm that the transparency was not a result of discontinuous film structure, SEM and AFM measurements were performed on the 25 nm film. Fig. 3.2 (c) and (d) show the results of those measurements respectively - both measurements showed a continuous film morphology. PLD particulates, a typical by-product of this deposition process, can be seen in the SEM image, while the RMS value from the AFM measurement showed the surface roughness to be of the order of 1 nm as seen in z-axis label in Fig. 3.2(d). Line profiles from the AFM measurements of all three films are also shown in Fig. 3.1(c), where it can be seen once again that the roughness is between 1-2 nm. The hypothesis for the optical transparency then had to be the bandgap of the films. Therefore Tauc plot analysis (details of which can be found in chapter 2 was performed on the as-prepared films of all three thicknesses, as shown in Fig. 3.1(b). An exponent of 2 on the y-axis of the Tauc plot gave the best fit to the linear regime of the absorption data, and so the direct bandgap obtained from this analysis was found to be ~3 eV for the 9 nm film, ~2.8 eV for the 25 nm film, and ~2.7 eV for the 35 nm film. These values are plotted as a function of thickness in the inset of Fig. 3.2(e) using open circles. All of these values are representative of a semiconductor rather than a metal film.



(a) (b) (c)

Figure 3.1: *(a) SEM image of O_2 annealed film. (b) Tauc plot analysis for AP films of different thicknesses. (c) Surface roughness profile of as-deposited films measured using AFM.*

These preliminary results from optical measurements done on the as-prepared films indicated that the metals from the PLD target were rapidly getting oxidized either during the deposition process itself or as soon as they were exposed to the atmosphere. To investigate the changes in the optical properties of the films upon further oxidation, the 25 nm film was annealed at 500 ºC for two hours in ambient atmosphere (i.e. O_2 anneal), and in nitrogen-rich atmosphere (i.e. N_2 anneal). Both the annealed films became visibly different from the AP state, as seen clearly in Fig. 3.2(a), samples labeled N_2 and O_2. Optical transmission of these films showed an increase in percentage transmission from their AP state between 1.5 eV to 3 eV; however, both annealing environments produced very similar optical behavior. Tauc plot analysis of the annealed films showed the bandgap to be about the same value of 2.8-2.85 eV as compared to the AP film. This is shown in Fig. 3.2(e) and in its inset as cross from O_2 annealed film, and open triangle for N_2 annealed film. Fig. 3.1(a) shows the SEM image of the O_2 annealed film, where the PLD particulate density was found to be less than that for the AP film.

In order to understand the origin of the bandgap, TEM, XPS and GIXRD studies of the AP and annealed films of 25 nm were performed, which would shed light on the chemical composition and stoichiometry of the films, as well as provide insight into the microstructure. Fig. 3.3(a) shows the HR-TEM image of the 25 nm AP film. There is no evident crystallinity from the image, which is further confirmed by the diffraction pattern presented in the inset, showing diffused rings which are characteristic of amorphous films. TEM image of the O_2 annealed film is shown in Fig. 3.4(c), which shows similar amorphous microstructure in the annealed state too. This finding is further consolidated by GIXRD data presented in Fig. 3.4(a) and (b) - (a) shows the XRD peaks obtained from the Terfenol-D target where the peaks align perfectly with those found in database for this material, while (b) shows GIXRD plots for AP, O_2 annealed and N_2 annealed films. The plots show features typically seen in amorphous films - no sharp peaks and a broad hump present near 30 degrees. The only peak that was observed in the samples originated from the SiO_2 substrate, as can be seen in the figure.

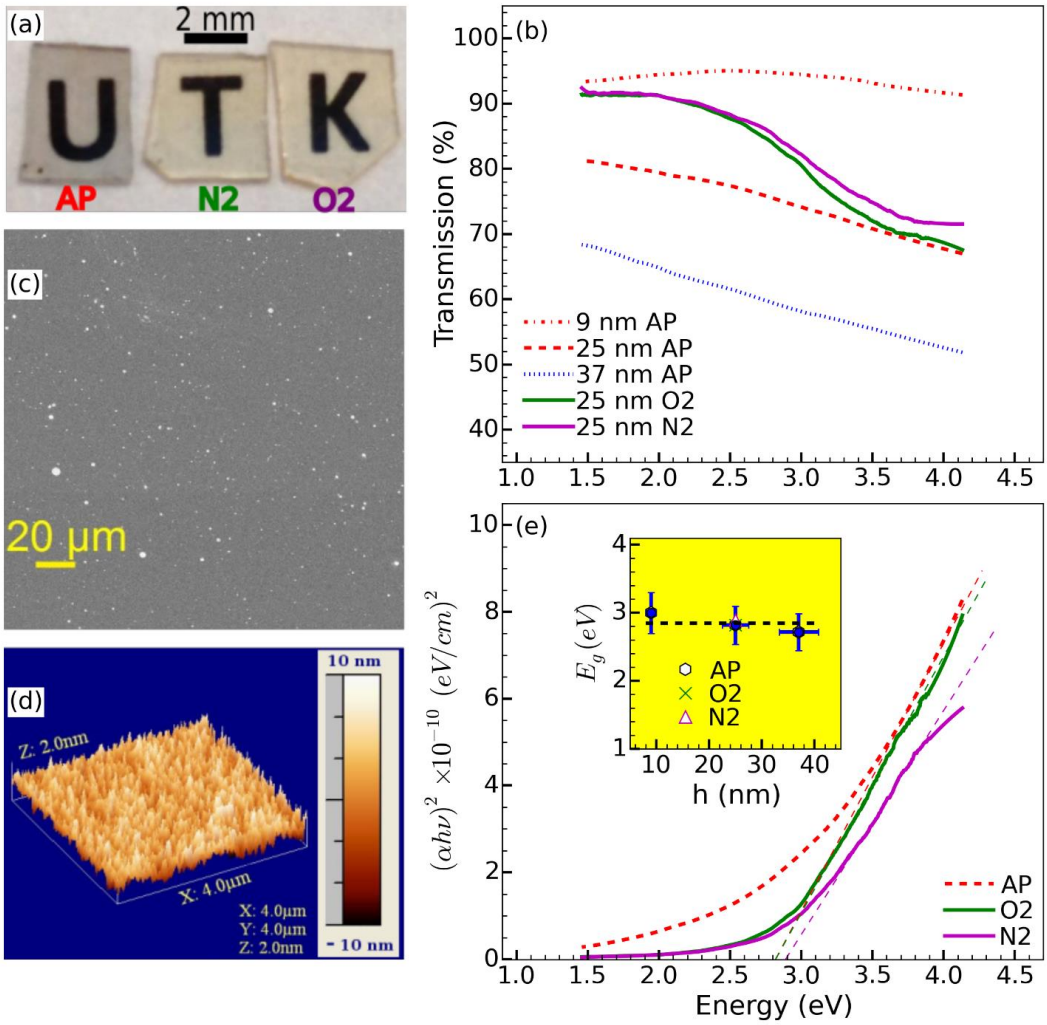


Figure 3.2: *(a) Optical photograph of lettered blocks showing the large transparency of 25 nm thick films in as-prepared state (marked as AP), and following annealing in nitrogen (marked as N2) and oxygen (marked as O2) at 500°C for 2 hrs. (b) Optical energy (and wavelength) dependent transmission of as-prepared films with thickness between 9 to 37 nm (dashed curves) and following annealing of the 25 nm film solid curves). (c-d) SEM (c) and AFM (d) information from a 25 nm as-prepared film respectively. (d) Tauc plot comparing the direct optical absorption in 25 nm films (as prepared is dashed line while annealed are solid lines. The extrapolations from the strongly absorbing linear regimes are shown and were used to estimate the band gap. Inset shows the Tauc direct band gap values as a function of thickness of the as-prepared films and following annealing of the 25 nm film. A line corresponding to the average band gap value from measurements of various as-prepared films is also shown in the inset.*

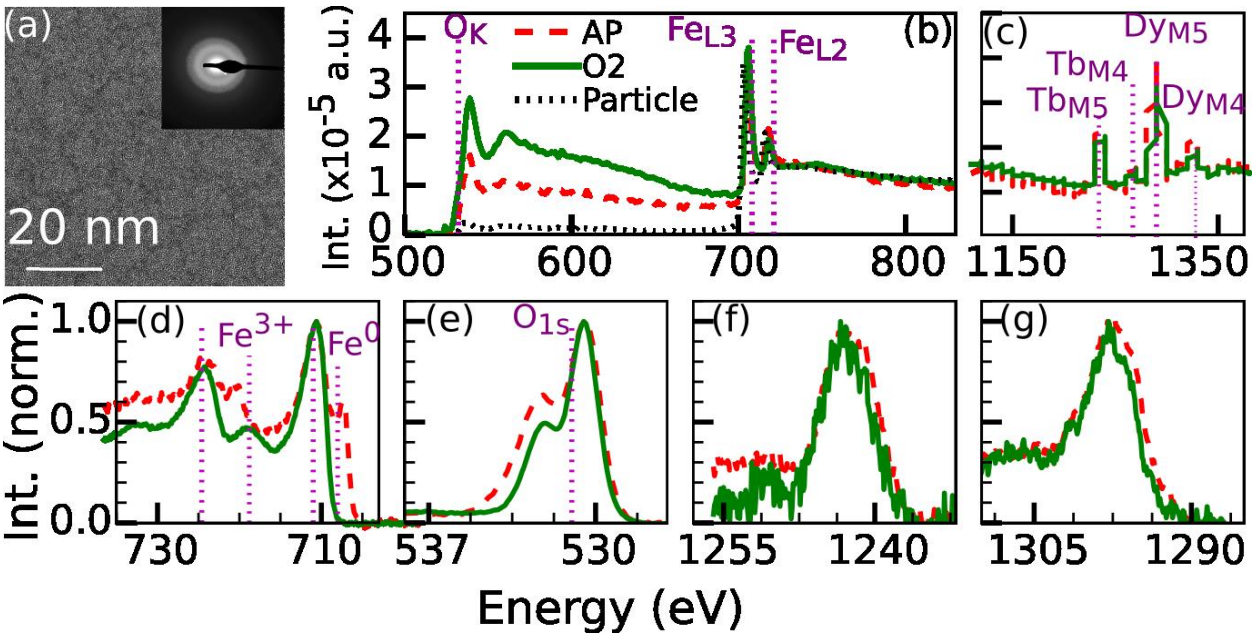


Figure 3.3: *(a) Amorphous microstructure of the as-prepared films was evidenced by TEM imaging and selected area diffraction (inset). (b-c) EELS analysis of the as-prepared and O_2 annealed films only detected Fe, and O (Fig. c) and Tb and Dy (Fig. d). In Fig. (b) the EELS spectrum from a PLD nanoparticle is also shown by dotted curve. (d-g) XPS measurements showing the various detected components in the as-prepared vs O_2 annealed films. (d) Fe 2p signal (e) O 1s signal. (f) Tb 3d 5/2 signal, (g) Dy 3d 5/2 signal. In figures b-g, the as-prepared (AP) films are shown by dashed curves while the O_2 (O2) annealed films are shown by solid curves. The vertical dotted lines mark the position of the various absorption edges (EELS) and peaks (XPS) as indicated. The additional vertical lines in Fig. (d) correspond to the additional Fe_{3d} absorption peaks found in the hematite and magnetite form or iron oxides.*

Fig. 3.3(b) and (c) show core loss EELS spectra for the AP (dashed red lines) and O_2 annealed (solid green line) samples showing volume averaged peaks for O, Fe, and Tb and Dy respectively. Analysis of the EELS spectra revealed the AP and O_2 annealed states to be very similar, with all the elements completely oxidized in both cases. Quantification of the EELS spectra resulted in the metal to oxygen ratio being 2:3, with an inherent error of 10%. Therefore the stoichiometry of the AP state could be stated as Me_2O_{3-x}, where Me = 66% Fe, 24% Dy, and 10% Tb. The Fe peak from the O_2 annealed film matched exactly with that for Fe_2O_3 found in database. This indicated that although the Fe cation changed during anneal, there was no change to the Tb and Dy cations. The stoichiometry of the O_2 annealed film was found to be Me_2O_3, which is more oxidized than the AP state. No evidence of cation segregation was observed from TEM, concluding that the films had homogeneous distribution of the metal cations. XPS measurements were carried out to look at the chemical composition on the surface of the film. The XPS survey scans of the AP and O_2 annealed films, shown in Fig. 3.4(d), revealed peaks from the expected metals, oxygen, and carbon. The carbon peak can be attributed to hydrocarbons on the surface from the atmosphere. Panels (d) to (g) in Fig. 3.3 show the XPS peaks for Fe 2p, O 1s, Tb 4d and Dy 4d respectively. Comparing the peak positions to those present in standard database, Fe^{3+} was identified in both the AP and O_2 annealed films by the presence of a satellite peak near 718.8 eV. However, the satellite peak was slightly shifted to a lower

energy, providing evidence for the presence of some Fe^{2+} as well. In addition, the AP sample showed a small peak at 707.4 eV that indicates Fe^0. However, it was concluded that the peak must have been from PLD particulates on the surface since no Fe^0 peak was observed in the EELS spectra. To confirm this hypothesis, EELS spectrum was taken from a particulate, as shown by the dotted black line in Fig. 3.3(b). There was no O peak visible for this spectrum, so the Fe peak in this case must have been from Fe^0. The formation of an oxide layer of about 10-30 nm in thickness has been reported by multiple groups [111, 112], where it was observed that the top oxide layer forms rapidly while the remaining bottom layers undergo slow oxidation. The amorphous microstructure is also not unexpected since the substrate was at room temperature - typically substrate heating is an important factor to grow crystalline films.

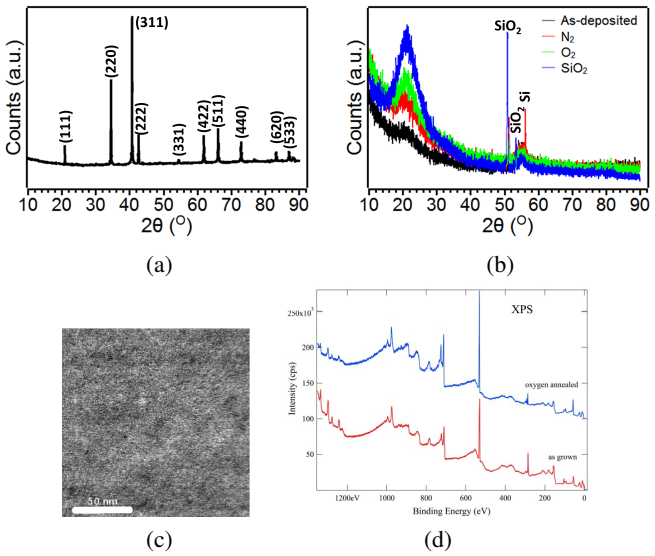


Figure 3.4: *(a) Shows the XRD of the Terfenol-D target. Indexing of the various peaks showed that the target was consistent with the original Terfenol-D composition. (b) Comparison of GIXRD scans of as-prepared, nitrogen annealed, and oxygen annealed films of 25 nm thickness as well as the underlying substrate which was SiO_2(400 nm)/Si. The only features evident from the films were the underlying substrate features, as indicated on the figure. This confirmed that the films were amorphous. (c) TEM image of O_2 annealed film (d) XPS survey scan to determine the elements present in the AP and annealed films.*

Since optically transparent oxides that are conductors/semiconductors are desirable for applications in electronic and display devices, the transport properties (i.e. conductivity and hall mobility) of the AP and annealed films were measured using the Van der Pauw technique, detailed in chapter 2. To determine whether the films were metallic or semiconducting, temperature dependent conductivity was measured, as shown in the inset of Fig. 3.5(a). Since the conductivity was seen to increase with increasing temperature, the as-prepared film was concluded to be semiconducting. Fig. 3.5 (a) shows the conductivity of the AP films decreasing with increasing thickness between 9 nm to 74 nm. The conductivity values were measured to be in the range between $5x10^3$ and $5x10^4$ S/m, which are exceptionally high when compared to the constituent oxides [6, 113]. Since the conductivity and hall mobility, μ_H, are related by the equation $\sigma = \mu_H ne$, where n is the carrier concentration, the hall mobility was measured for AP films of various thicknesses too. A

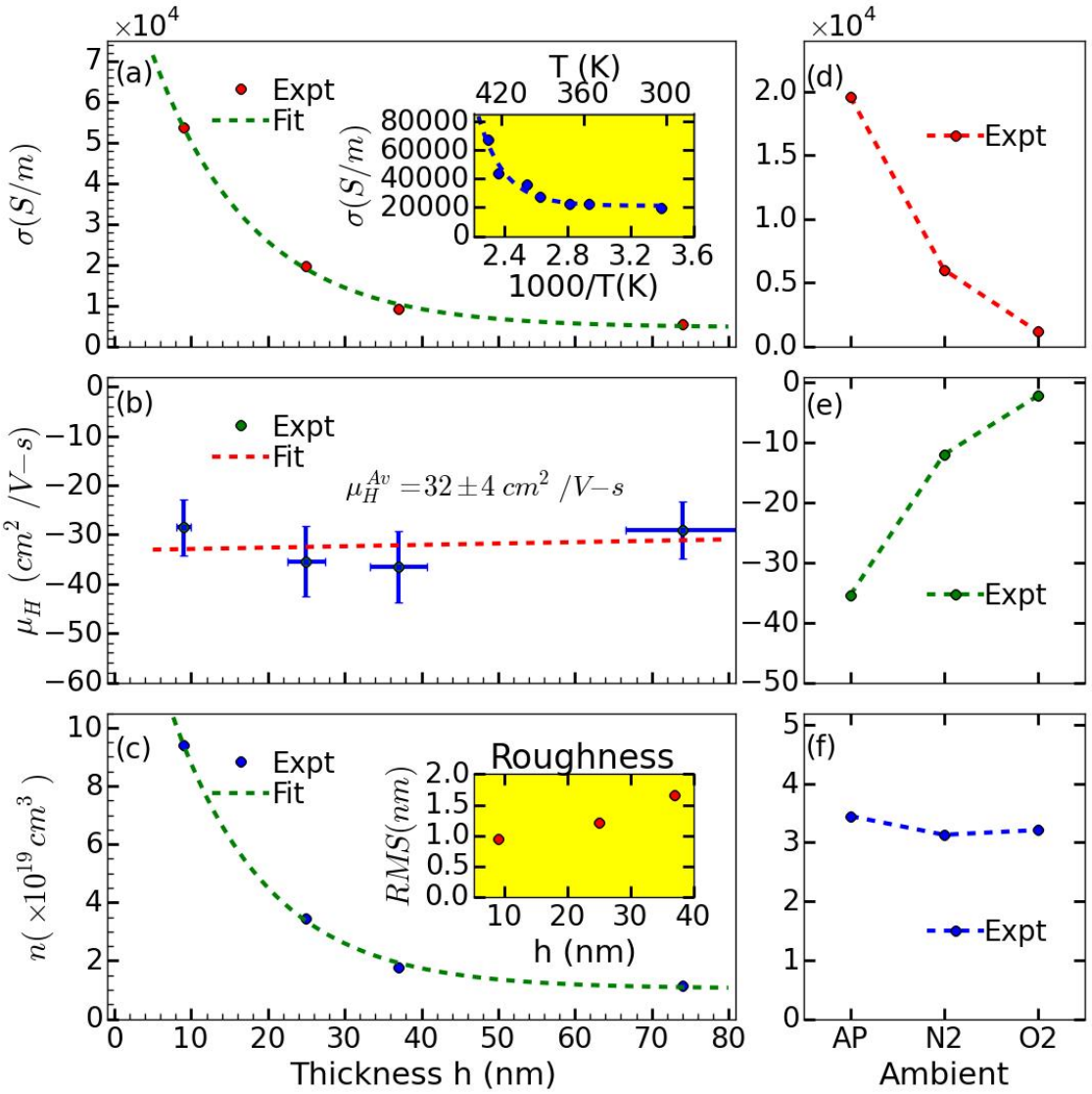
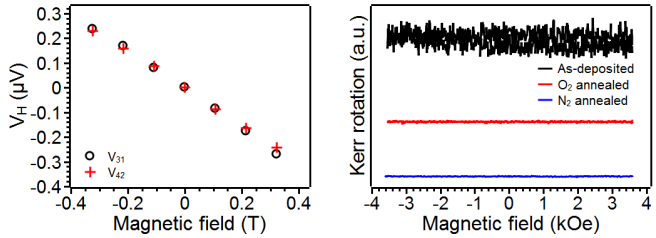


Figure 3.5: *Transport properties of the as-prepared (a-c) and annealed films (d-f). (a) Dependence of conductivity on thickness of as-prepared films. Inset shows that the conductivity σ increased exponentially with temperature for a 25 nm as-prepared film. (b) The mobility of the as-prepared films showed n-type conductivity and its magnitude was relatively unchanged with thickness yielding an average value of 32±4 cm^2/V-s. (c) The electron carrier concentration in the as-prepared films decreased exponentially with increasing film thickness. This correlated with an increased surface roughness of the films (inset). (d) Conductivity change for 25 nm films following annealing in nitrogen (N_2) or oxygen (O_2) at 500°C for 2 hrs. (e) Mobility change with annealing. (f) Carrier concentration remained relatively unchanged following annealing. In figures d-f, the as-prepared films are indicated as AP while the O_2 and N_2 annealed films are marked as O2 and N2 respectively. The dashed lines in (a-c) correspond to best fits to the experimental data. The dashed lines in (d-f) correspond to guides to the eye.*

typical hall voltage vs magnetic field plot is shown in Fig. 3.6(a), where the slope of the plot was used to calculate the hall mobility. The negative slope also was a sign of n-type carriers responsible for conduction in the material. Although the mobility was seen to be quite constant around 32 cm^2/V-s with the changing thickness, and thus could not explain the change in the conductivity, the value of the mobility was very high for a system containing oxides of Fe, Tb, and Dy. To rule out the presence of anomalous hall effect, magnetism in the AP films were probed using SMOKE measurements, shown in Fig. 3.6(b). No magnetism was detected in the AP film (black line), and so the hall mobility values were confirmed to be due to the ordinary hall effect and not the anomalous hall effect. Calculation of carrier concentration from the mobility and conductivity values showed the carrier concentration to decrease with increasing thickness. Although this phenomena has been observed in ultrathin semiconducting films [114], in the studied system it could be a result of increasing surface roughness, as demonstrated in the inset of Fig. 3.5(c). The carrier concentration values were also very high compared to doped semiconductors used as channel layers for thin film transistors, thus the AP films were indicative more of a degenerate semiconductor.

Transport properties of the O_2 and N_2 annealed films were also measured, as seen in Fig. 3.5(d)-(f). Both conductivity and hall mobility were seen to decrease with higher level of oxygen incorporation in the films, while the carrier concentration remained fairly unchanged. Regardless, the lowest mobility value of 2.2 cm^2/V-s obtained for the O_2 annealed film was higher than the constituent oxides. SMOKE measurement of the annealed films, shown in Fig. 3.6(b) also confirm the absence of magnetism, and hence of anomalous hall effect, in the annealed films. The annealing result could provide insight into controlling the transport properties of the films for future applications.



(a) (b)

Figure 3.6: *(a) Plot of Hall voltage as a function of applied magnetic field for a 74 nm thick as-prepared film studied for two different voltage configurations for an applied current of 100 μA. (b) Kerr rotation measurements of as-prepared and annealed films.*

3.4 Discussion and conclusion

Combination of high optical transparency, high conductivity, and high mobility has been observed in only a select few systems that have cations with the outer orbital having electronic configuration of $(n\text{-}1)d^{10}ns^0$ [14, 59]. This leads to the s orbitals being responsible for the conduction band, while the valence band is formed by the oxygen 2p orbital leading to a large band gap and subsequent transparency in the visible spectrum. Conduction in such systems is high because of the huge overlap between the s-orbitals, and the high mobility originates due to the high curvature of these orbitals too. In addition, the second feature in such

systems is that the hall mobility and conductivity of the ternary oxide cannot exceed that of its constituent oxides [13, 115].

The FDTO system has none of these attributes. The constituent oxides (Fe_2O_3, Tb_2O_3, and Dy_2O_3) are well known for their low conductivity, the latter two being used mostly as dielectric materials. In Fe_2O_3, the conduction band is made of Fe 3d-orbital and the valence band from O 2p orbital. The d-orbital is relatively flat, and hence mobility is low in these systems (<0.001 cm^2/V-s) [116]. Similar situation exists in the oxides of the lanthanides where the 4f orbital from Tb and Dy form the conduction band and the O 2p orbital forms the valence band. The f-orbitals are even flatter compared to the d-orbitals, and hence the lanthanide oxides are insulators [9, 113]. However, the Tb and Dy 4f orbitals have the ability to introduce filled or empty states inside the optical bandgap [117]. Therefore, in the Fe-Dy-Tb-oxide system, it is very likely that the f and d-orbitals make the conduction bands instead of the s-subshells of these cations [118]. Despite this, we observed conductivity and hall mobility to be several orders of magnitude higher than what is traditionally expected in this system. This could lead to completely new physics of understanding how conduction takes place in ternary oxides. The conductivity could be a result of interaction between the 4f and 3d orbitals that have not been investigated before. Understanding the origin of these properties could introduce new options for materials to be used for electronic and energy applications. The remaining chapters of the thesis aim to understand the origin of these properties by changing the cation ratio in the system, performing controlled annealing studies, changing the oxygen content of the films during the growth process, and finally finding an application for this material.

3.5 Acknowledgments

This work was primarily supported by ARO grant W911NF-13-1-0428, and a Science Alliance JDRD grant U013960010. One of the students was partly supported by NSF TNSCORE grant EPS-1004083 while XPS and SEM characterization was conducted through proposals CNMS2013-284 and CNMS2014-327 at the Center for Nanophase Materials Sciences, which is a DOE Office of Science User Facility. Some of the authors would also like to thank Prof. K. Islam at UT Knoxville for access to critical equipment for transport property measurements. The GIXRD experiments were performed using the instruments that were procured through the general infrastructure grant of DOE-Nuclear Energy University Program (DE-NE0000693). A portion of this work were performed at Oak Ridge National Laboratory, operated by UT-Battelle for the U.S. Department of energy under contract no. DE-AC05-00OR22725. RCP and BL acknowledge support from the Lab Directed Research and Development Program at ORNL.

3.6 Author contributions statement

AM, HT, AF, GD, AB, and MP performed the materials synthesis and various characterization tasks. RK and AM designed the materials synthesis experiments and RK wrote the main manuscript text. RCP and BL, along with the other co-authors were involved in analyzing the data and concluding the results. All authors reviewed the manuscript.

Chapter 4

Transparent ferromagnetic and semiconducting behavior in Fe- Dy-Tb based amorphous oxide films

(Reproduced with permission from Humaira Taz, Tamil Sakthivel, Nana K. Yamoah, Connor Carr, Dhananjay Kumar, Sudipta Seal, and Ramki Kalyanaraman, *Scientific Reports*, **2016**, accepted. Copyright 2016 Nature Publishing Group)

4.1 Summary

In this chapter we report the transport, optical, and magnetic properties of amorphous thin films of FDTO having different compositions of metals Fe, Tb, and Dy that show unique combination of functional properties. Films were deposited with different atomic weight ratio (R) of Fe to Lanthanide (Dy + Tb) using electron beam co-evaporation at room temperature. The films were found to be amorphous, with grazing incidence x-ray diffraction and x-ray photoelectron spectroscopy studies indicating that the films were largely oxidized with a majority of the metal being in higher oxidation states. Films with R = 0.6 were semiconducting with visible light transmission due to a direct optical band-gap (2.49 eV), had low resistivity and sheet resistance (7.15×10^{-4} Ω-cm and ~200 Ω/sq respectively), and showed room temperature ferromagnetism. A metal to semiconductor transition with composition (for R < 11.9) also correlated well with the absence of any metallic Fe^0 oxidation state in the R = 0.6 case as well as a significantly higher fraction of oxidized Dy. The combination of amorphous microstructure and room temperature electronic and magnetic properties could lead to the use of the material in multiple applications, including as a transparent conductor, active material in thin film transistors for display devices, and in spin-dependent electronics.

4.2 Methods

The material synthesis by e-beam evaporation is described in chapter 2. The characterization techniques used are listed below:

- SEM and AFM were used for surface morphology
- UV-Vis transmission spectroscopy were used for optical properties
- XPS, XRD, and EDS were used for material characterization
- SMOKE and VSM were used for magnetic characterization
- Van der Pauw sheet resistance and hall measurements were made at room temperature; resistance was measured from 3 K to 300 K as well.

4.3 Results

Our investigations were motivated by the role of metal composition in the FDTO system with the hypothesis that since Fe is the largest component of the metal in the original Terfenol-D alloy, its ratio with respect to the lanthanides could shed important clues about the electronic, optical and magnetic properties of this material. For this reason, we have prepared films with Fe to lanthanide metal (Tb+Dy) atomic weight ratio R varying between 0.60 to ~21.

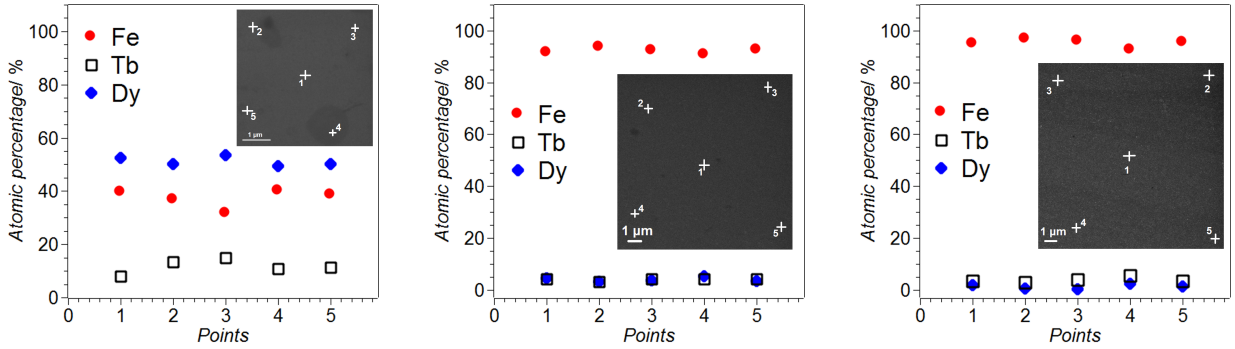


Figure 4.1: *Plots showing quantified atomic percentages of Fe, Tb and Dy from the five EDS point spectra for (a) R = 0.60, (b) R = 11.9, and (c) R = 21. The inset in each plot shows the SEM image of the film with the respective R value, with regions marked by white plus signs (numbered) to show the locations where the EDS spectra were obtained from.*

The morphology and composition (as well as composition uniformity) for the different films were analyzed using scanning electron microscopy (SEM) and energy dispersive x-ray analysis in the SEM, respectively. SEM images for each of the samples showed a featureless film, as evident in the insets of the plots in Fig. 4.1(a,b,c). EDS point spectra were obtained from 5 locations (each $57\,nm \times 57\,nm$), which were subsequently quantified to obtain atomic percentages of Fe, Tb and Dy. Fig. 4.1(a,b,c) show the atomic

percentages from all five locations for films with R = 0.60, 11.9 and 21 respectively, confirming a homogeneous distribution of the three elements. Fig. 4.2(a) inset shows another SEM micrograph of the film with R=0.60. Once again, a featureless morphology reflecting the generally smooth films was evident; the dark spots present in the SEM image arises from ambient, organic contamination. The SEM images for the remaining two films can be found in the supplement. In Fig. 4.2(a) is the typical EDS point spectrum from a $57\,nm \times 57\,nm$ sized area on the film. Quantitative analysis of the various peaks yielded the atomic % of each metal. The uniformity of the composition across the film was evaluated by performing similar EDS analysis at 5 random locations. We determined that all the films investigated were highly uniform in their spatial composition, consistent with deposition by the e-beam evaporation process which normally yields good spatial uniformity.

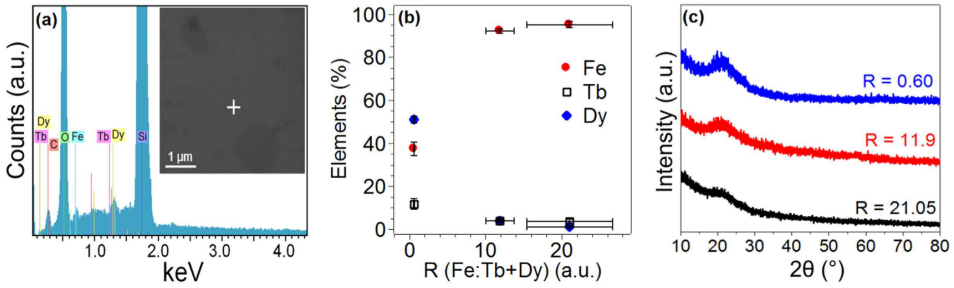


Figure 4.2: *(a) Typical EDS point spectrum from the film with R = 0.60. Inset shows the SEM micrograph of the film and the plus sign marks the spot from where the point spectrum was obtained (b) Plot showing the atomic percentage of Fe, Tb and Dy in the three samples as a function of R (Fe: Tb+Dy) (c) GIXRD plots for typical films from the different R values.*

In Fig. 4.2(b), the cumulative results of the atomic % of the metallic elements present for the films prepared under the three different co-evaporation conditions is shown as a function of the atomic concentration ratio R defined as the atomic % of Fe to the atomic % of the lanthanides (Tb + Dy). The primary change among the three films was in the concentration of Fe and Dy, while the concentration of Tb remained relatively unchanged. The three films had R of 0.60 ± 0.083, 11.9 ± 1.84 and 21.05 ± 5.62 respectively, and several films (up to 3 each) with these compositions with a fixed total thickness of 40 nm (calculated from pre-calibrated deposition rates of the targets in e-beam) were systematically investigated for various physical properties. In Fig. 4.2(c) the GIXRD scan from each of the compositions is shown. No evidence for crystalline scattering was evident and on a broad peak centered around a 2θ of ~$22^{o}$was observed in each case. Such featureless x-ray spectra with a single broad peak at low angles are generally evidence for lack of any long range order, [119, 120] thus implying that all the films compositions deposited here were amorphous.

Knowing the oxidizing nature of the individual metals in this film, we next performed detailed investigations of the metal cation state (and oxygen content, which is presented in the supplement) in the films through XPS analysis. Fig. 4.3(a, b, c) show the Fe 2p peaks for the three cases as well as deconvoluted spectrum obtained by peak fitting using Peakfit software [121]. The deconvoluted peaks help identify the different cation states present. In films with R = 21.05 and R = 11.9, a peak at 706.2 eV and a satellite peak at 719.8 eV indicated the presence of Fe^{0}, which is the metallic Fe; however for films with R = 0.60, these two peaks were missing. The predominant state of Fe in all three samples was Fe^{3+}, with peaks centered

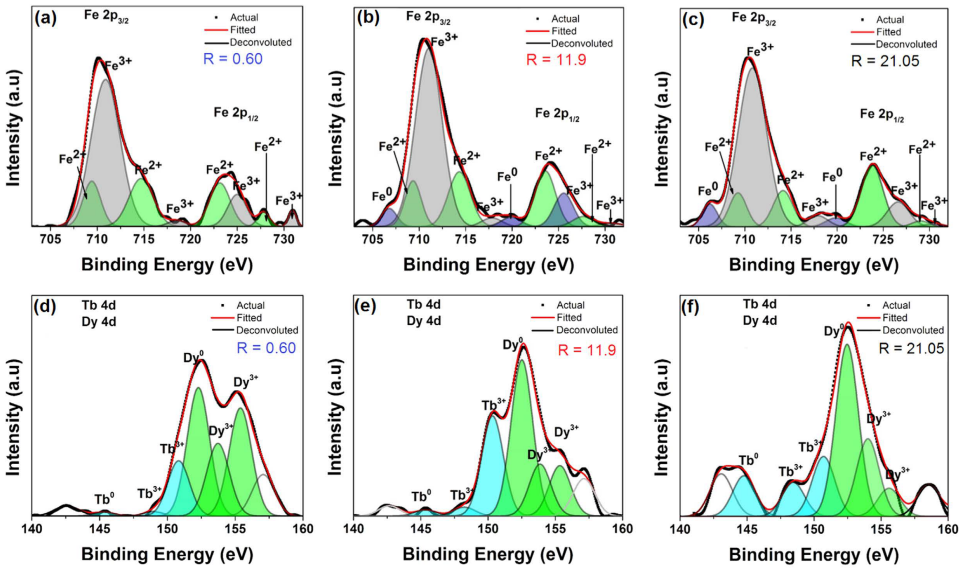


Figure 4.3: *XPS plots showing (a, b, c) Fe 2p, and (d, e, f) Tb and Dy 4d for all three R values.*

at 710.82 eV, 711.09 eV, and 710.62 eV, and satellite peaks centered at 717.93 eV, 717.82 eV, and 718.54 eV for samples R=21.05, 11.9 and 0.60 respectively. The samples also contained some Fe^{2+} that had peaks centered at 709 eV and satellite peaks centered at 714 eV for all three samples [122]. The relative concentration of each cation state was calculated using $[Fe^x = \sum\text{IA of Fe}^x / \sum\text{IA of Fe}]$, where Fe^x is the Fe atomic concentration of the cation state x, IA of Fe^x is the integrated area of the corresponding state x, and IA of Fe is the total integrated area of Fe peaks. Upon quantifying the percentage of the three Fe states from the XPS spectra, it was found that the percentage of Fe^0, Fe^{2+} and Fe^{3+}, respectively, were 8.21%, 28.12% and 63.67% for R = 21.05, 5.11%, 30.86% and 64.03% for R = 11.9, and 0%, 35.13% and 64.87% for R = 0.60. These values are tabulated in Table 4.1.

Table 4.1: *Cation composition of the various metals measured by XPS for the three composition ratios investigated.*

Cation	Composition ratio		
	R=0.60	*11.9*	*21.05*
Fe^0	0	5.11	8.21
Fe^{2+}	35.13	30.86	28.12
Fe^{3+}	64.87	64.03	63.67
Tb^0	5.09	7.48	30.52
Tb^{3+}	94.91	92.52	69.48
Dy^0	41.38	60.40	61.87
Dy^{3+}	58.61	41.38	38.13

A similar analysis was performed for the lanthanide metals. In Fig. 4.3(d, e, f)), the 4d peaks for both Tb and Dy are presented. The Tb^0 peak was centered around 145 eV for all three samples, while the two peaks observed for Tb^{3+} were centered around 148 eV and 150 eV for the various composition. Similar results were observed for Dy where the Dy^0 peak was centered around 152 eV and Dy^{3+} peaks were centered around

154 eV and 155 eV. The deconvoluted Tb and Dy peaks were also quantified. The relative concentration of Tb^0 and Tb^{3+} for each of the samples is shown in Table 4.1. For the case of Tb, as composition changed from R = 0.60 to R = 21.05, the concentration of metal Tb, i.e. Tb^0 increased with concomitant decrease in that of Tb^{3+}. A similar behavior was observed for the Dy, with the relative concentrations of Dy^0 increasing and Dy^{3+} decreasing with increasing ratio R. Fig. 4.4(a) demonstrates the trend in the relative concentration of Fe metal and of all the cations as R increases. The relative concentrations of all the metal cation percentages decrease with increasing value of R, and remarkably there is no metallic Fe for R = 0.60. Fig. 4.4(b) (right y-axis) shows the ratio of Fe^{3+} to Fe^{2+} as a function of R as well, and it shows almost a linearly increasing trend with increasing R. More importantly, for R = 0.60, the value of the ratio is 1.84, which has further significance as discussed later in the paper. In Fig. 4.4(b, left y-axis) the total metal ($M^0 = Fe^0 + Dy^0 + Tb^0$) to metal cation ($M^{n+} = Fe^{2+} + Fe^{3+} + Dy^{3+} + Tb^{3+}$) ratio is shown as a function of the composition ratio R (open circular symbols). From this it was evident that for compositions 0.60 and 11.9 more than 75% (84.5% and 76.3% respectively) of the metal was in oxidized state, while for the R =21.05 case 66.5% was oxidized.

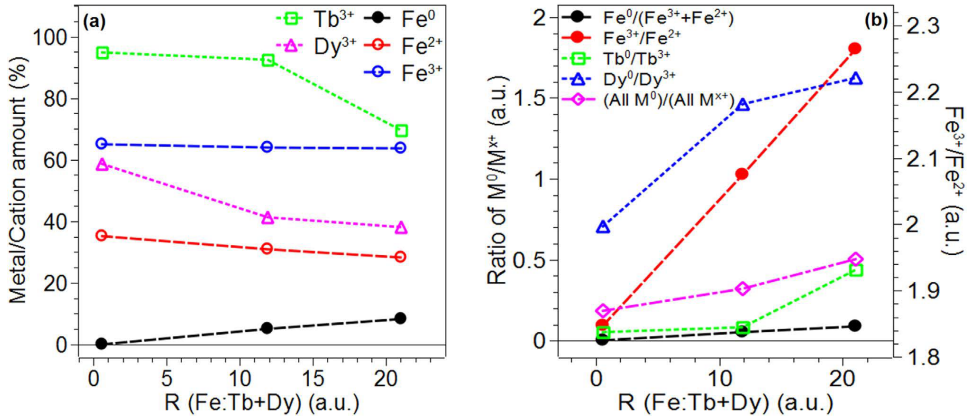
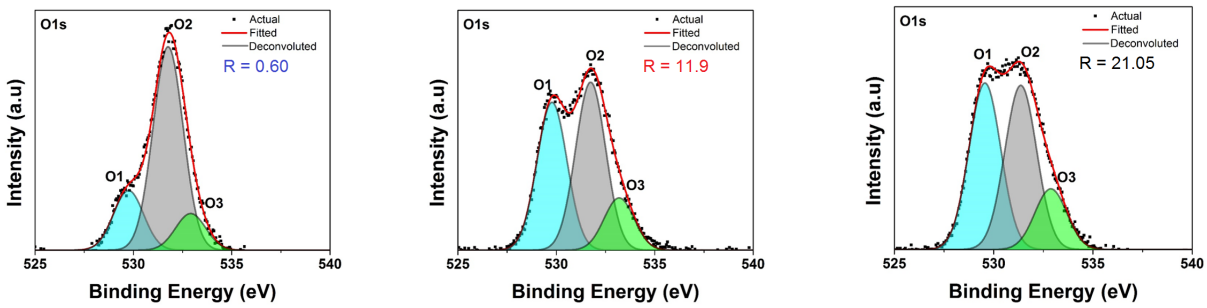


Figure 4.4: *Plots of (a) metal and cation relative concentrations and (b) the ratio of metal to their cation states (left y-axis, black, green and blue data points), and the ratio of Fe^{3+} to Fe^{2+} (right y-axis, red closed circles) as a function of R (Fe:Tb+Dy)*

The XPS peaks corresponding to oxygen in such oxide systems, i.e. O1s peaks, are generally known to be broad with multiple overlapping components [123, 124]. In 4.5(c), the O1 peak centered at 529.6 eV was seen in all three compositions and is generally attributed to the Fe metal oxide, but, according to literature, can also correspond to the oxides from Tb and Dy [123, 125]. The O2 peak marked and centered around 531.7eV may be attributed to the OH^- species that are mostly present on the surface. The formation of the hydroxide could be due to the reduction of the oxygen in the air to hydroxide at the metal surface by the moisture in the air. The metal is thus oxidized to cations and the corresponding metal hydroxide also forms very rapidly. The high binding energy peak centered at around 533 eV belongs to the adsorbed moisture on the surface. According to literature, this peak also belongs to SiO_2; however it is not a plausible explanation in our case because the deposited film thickness is about 40 nm. Overall, the integrated area of the O1 and the O2 peaks was seen to increase with the decreasing R value, thus supporting the changing metal oxide

content with composition ratio R.



(a) (b) (c)

Figure 4.5: *XPS plots (a), (b), (c) showing O1s spectra for all three R values.*

XPS spectra can provide very useful information on the position of the valence band edge with respect to the Fermi level, which, in turn, could help correlate the composition with physical properties. In Fig. 4.6(a) the valence band edge analysis was performed for all three compositions to ascertain the location of the valence band maximum (VBM) with respect to the position of the Fermi level [which corresponds to 0 eV binding energy on Fig. 4.6(a)]. From the figure, it can be seen the VBM was quite different for the various compositions. The R = 11.9 and 21.05 cases had a VBM at -0.6 eV and -1.2 eV respectively, implying that the Fermi level was lower than the VBM, a behavior generally observed in metallic systems. On the other hand, the R = 0.60 composition had a VBM at 2.2 eV, implying that the VBM was below the Fermi level, a scenario typically seen in insulating or semiconducting material. To further establish the validity of this XPS findings, the broadband optical transmission spectra for the various compositions was analyzed and is shown in Fig 4.6(b). The compositions of R = 11.9 and 21.05 had an extremely low transmission over the wavelength range investigated (which included the visible optical range between 300 and 800 nm), while the R = 0.60 case showed a significantly higher transmission of > 45% throughout the range. This transparency measurement generally supported the XPS analysis of Fig. 4.6(a), i.e. the transmission of R = 11.9 and 21.05 were more consistent with a metallic system while R = 0.60 was more consistent with a semiconductor. To establish the nature and magnitude of the band-gap in R =0.60, the Tauc plot was generated, and is shown in the inset of Fig. 4.6(b). From this plot, the direct band-gap of ~2.4 eV was estimated from the intercept, as shown on the figure. Therefore, by combining the measurement from the XPS (VBM is at 2.2 eV) and the optical bandgap value, the conduction band energy was ~0.2 eV above the Fermi level, implying that R = 0.60 should behave like an n-type semiconductor.

To further understand (and differentiate) the various compositions, the room temperature electrical properties were measured using four probe technique. Fig. 4.7(a) shows the resistivity ρ of the films, while the inset shows the sheet resistance R_s, as a function of composition ratio R. From this it was evident that a dramatic decrease in resistivity occurred in going from R = 0.60 ($\rho = 7.15 \times 10^{-4} \Omega - cm$) to R = 11.9, and subsequently the resistivity was relatively unchanged ($\rho \sim 9 \times 10^{-5} \Omega - cm$). This resistivity behavior was generally consistent with the results of XPS and optical transmission suggesting that R = 11.9 and 21.05 were likely metallic (low resistivity) while R =0.60 was semiconducting (higher resistivity). In fact, the

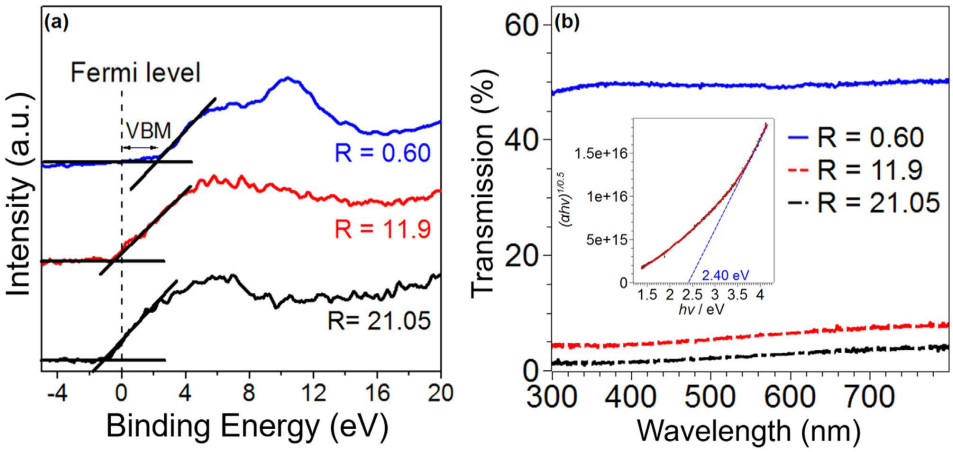


Figure 4.6: *(a) XPS spectra for R = 0.60 (blue), 11.9 (red), and 21.05 (black) showing the valence band maximum. (b) Plot of percentage transmission vs the probing wavelength for all three samples; inset shows the Tauc plot for R = 0.60 generated from its transmission data using m = 1/2 for calculating a direct bandgap.*

resistivity for the optically transparent film (having R = 0.60) is comparable to the reported resistivity for amorphous ITO films of similar thickness ($5.93 \times 10^{-4} \Omega - cm$ for a 97 nm thick film) [28]. The resistivity could be further related to some fundamental quantities of the material through $\rho = 1/\mu_H ne$, where μ_H is the Hall mobility, n is the carrier concentration and e is the electron charge. An independent measurement of the Hall voltage was used to extract the carrier concentration (with knowledge of the ρ) and the type of charge carriers (i.e. n- vs p-type). In Fig. 4.7(b), the measured Hall mobility is shown (open symbols) as a function of the composition. The sign of the mobility was negative ($-ve$) for all compositions, implying n-type carriers, and the mobility value for the semiconductor film (R =0.6) was >300 cm^2/V-s, while those for the two metallic films were 73 cm^2/V-s (R = 11.9) and 65 cm^2/V-s (R = 21.05). This finding was not surprising since metals are known to have lower hall mobility values than semiconductors [126]. From the measured ρ and μ_H values, the carrier concentration was estimated, and, as shown in Fig. 4.7(b, closed symbols) the carrier concentration dropped by approximately two orders of magnitude from the R = 11.9 and 21.05 compositions ($n \sim 10^{21} cm^{-3}$) to the R = 0.60 case ($n \sim 10^{19} cm^{-3}$), again supporting the semiconducting nature of R = 0.60.

Given the high concentration of iron in these films, we also measured the magnetic response as a function of composition. Fig. 4.8(a) compares the room temperature hysteresis behavior of the three compositions measured using a PPMS instrument. All three compositions showed clear evidence for a saturation field as well as evidence for hysteresis with a small coercive field suggesting soft ferromagnetic behavior at room temperature. In Fig. 4.8(b), the saturation field and the coercivity values are shown as a function of composition. Both quantities were found to increase in going from the metallic compositions (R =11.9, 21.05) to the semiconducting state (R = 0.60). We also measured the the magnetic behavior using the Surface Magneto-Optical Kerr Effect (SMOKE) technique that detects change in incident light polarization with applied magnetic field. Shown in Fig. Fig. 4.8(c) are the relative Kerr intensities as a function of magnetic field measured at room temperature for the various compositions. These measurements also displayed

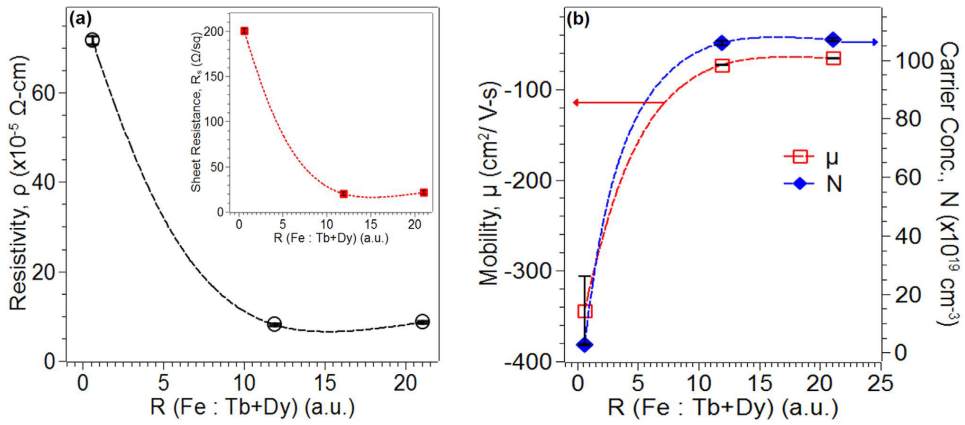


Figure 4.7: *Plot of (a) four-probe resistivity (black, filled circles) with inset showing four-probe sheet resistance (red, filled rectangles), and (b) hall mobility (empty, red squares), and carrier concentration (filled, green diamonds; right y-axis) as a function of R (Fe:Tb+Dy)*

hysteresis behavior with a saturation and coercivity similar to that measured using the PPMS [Fig. 4.8(a)] supporting the general observation that all the compositions investigated displayed soft ferromagnetism at room temperature.

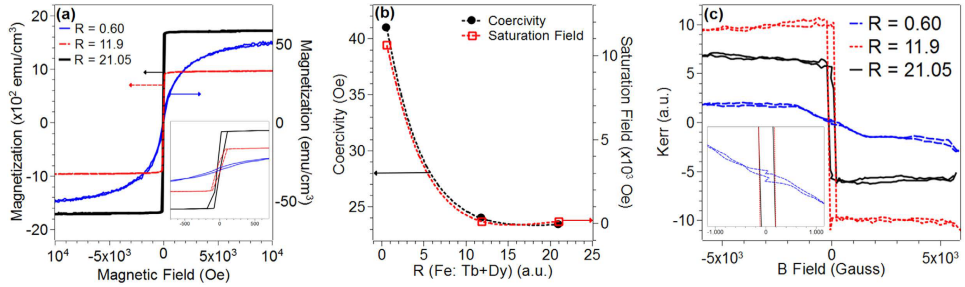


Figure 4.8: *(a) Magnetic hysteresis measurements at 300 K are plotted for all the compositions; inset shows a magnified view near the zero field to highlight the coercivity in each of the plots. (b) Plot of the coercivity (left y-axis) and saturation field (right y-axis) as a function of composition for all the samples (c) Plot of Kerr rotation for all three compositions using magnetic field of -6000 Gauss to 6000 Gauss. Inset of plot shows a magnified view of the plots near zero field to highlight the coercivity.*

4.4 Discussion and conclusion

From the XPS results, it was evident that the vacuum deposited metallic alloy film, for all the compositions investigated, was rapidly being oxidized upon exposure to air ambient at room temperature. This result was consistent with the recently reported observations that the the Terfenol-D composition (which has R ~ 1.94) also rapidly oxidizes upon air exposure to yield semiconducting films. From Fig. 4.4(c), it was evident that the oxidized metal made up ~50% or more of the total metal atoms and so we therefore one could call these films a highly oxidized film. In this context, the transition from the metal to semiconducting behavior with composition can be correlated with certain important changes. First, we analyzed the Fe^{3+}/Fe^{2+} ratio, and

this was found to decrease from 2.26 in R = 9 to 1.84 in R= 1, as demonstrated in Fig. 4.4(b). The value of 1.84 in R =1 is very close to the value typically reported in magnetite (Fe_3O_4) [127]. On the other hand, the binding energy of Fe^{3+} of 710.82 eV and 711.09 eV in samples 1 and 2 respectively can be assigned to the Fe $2p_{3/2}$value observed in γ-Fe_2O_3 (maghemite). Therefore, one important change in the film with decreasing R appears to be the change in the type of iron oxide, i.e. from predominantly γ-Fe_2O_3 to Fe_3O_4 (along with the simultaneous decrease in the amount of Fe^0 content in the film). However, neither of these forms of iron oxide are known to have the combination of low resistivity and high mobility values measured here. Fe_3O_4 is reported to have resistivity of the order of $10^{-3}\,\Omega - cm$ [31, 128] while it is of the order of $10^3\,\Omega - cm$ for γ-Fe_2O_3 [3]. A 41 nm thickness epitaxial magnetite film has been reported to have an effective hall mobility of about $0.07 cm^2/V - s$, with a maximum anomalous hall mobility of $35\,cm^2/V - s$ [129]. Although a hall mobility for a maghemite thin film was not available, the two oxides (magnetite and maghemite) are reported to have similar and low mobility values due to the narrowness of the d-bands [130]. Furthermore, there is little known about the electronic properties of these oxides in their amorphous state. In this context, it is tempting to assign the general behavior of these compositions as well as the transition from metallic to semiconducting state to the behavior of the lanthanide elements. With reference to Fig. 4.4(a) and (b), it was evident that the metal cations of both the lanthanide metals increased with decreasing R value. However, the Dy showed a dramatic change in the fraction of metallic to oxidized state, i.e. Dy^0/Dy^{3+}, dropped from >1.5 for R $\geq$ 11.9, to $\sim$0.7 for R = 0.60. Such a large drop was not seen in any of the other metal constituents. Since this change in the Dy cation composition was strongly correlated with the measured optical and electronic changes, we hypothesize that the among other possible factors, the oxidation of the Dy metal is one of the most important drivers for the appearance of the novel properties being evidenced in these materials.

In this study, thin films with varying composition atomic ratio of Fe:(Dy+Tb) (atomic percentages) were fabricated at room temperature. The films were found to be homogeneous in composition and had amorphous microstructure. Chemical analysis by XPS studies showed that while the metal cation fraction increased with decreasing atomic ratio Fe:(Dy+Tb), all the films had a large fraction of oxidized metal ($\geq$66%). Furthermore, XPS valence band edge analysis suggested that high iron compositions were metallic while the high lanthanide composition was semiconducting. These properties were supported by optical transmission and electrical resistivity measurements of the films. All the compositions were found to have ferromagnetism at room temperature. The finding of the composition-tunable metallic-semiconducting behavior, as well as the presence of room temperature ferromagnetism, optical transparency, and semiconducting behavior suggests the following: the combination of Fe with the lanthanides (Dy and Tb) can lead to a class of materials with a range of multifunctional applications in the amorphous phase.

4.5 Acknowledgments

This work was primarily supported by ARO grant W911NF-13-1-0428. Ms Taz was partly supported by NSF TNSCORE grant EPS-1004083 while SEM characterization was conducted through proposal CNMS2016-034 at the Center for Nanophase Materials Sciences, which is a DOE Office of Science User Facility. DK

acknowledges partial support by the National Science Foundation (NSF) through the Nebraska Materials Research Science and Engineering Center (MRSEC) grant No. DMR-1420645. RK and HT also acknowledge Jagjit Nanda at the Materials Science and Technology Division at Oak Ridge National Lab for use of AFM.

4.6 Author contributions statement

H.T. performed the materials synthesis and as well as optical and electrical characterization tasks. C.C. performed electrical characterization. T.S. and S.S. performed the XPS measurements and analysis. N.K.Y. and D.K. performed the PPMS magnetic characterization and analysis. All the authors were involved in analyzing the data and concluding the results. R.K. and H.T. designed the materials synthesis experiments and R.K. wrote the main manuscript text. All authors reviewed the manuscript.

Chapter 5

High conductivity and magnetism in $Fe_{21}Dy_{0.81}Tb_{0.19}$ oxide thin film from cyclic annealing and oxidation

5.1 Summary

The field of spintronics continues to progress in the quest for obtaining memory devices that can have higher information density while operating at a lower energy. New materials have been developed that combine high conductivity and room temperature ferromagnetism, such as the Heusler alloys and dilute magnetic semiconductors. While Fe_3O_4 is the oldest known naturally occurring ferromagnetic oxide, its application towards spintronic devices have been slow due to the deterioration of magnetism as a result of grain boundaries. Here we report the development of a stable phase of $Fe_{21}Dy_{0.81}Tb_{0.19}$ oxide by annealing the as-prepared films grown by electron-beam evaporation through 14 heating cycles from 300 K to 700 K in 5 mTorr environment. The post annealed oxide film was a stable semiconductor having very low resistivity of 0.34 mohm-cm, two orders of magnitude lower than that of Fe_3O_4 (~10 mohm-cm), and room temperature magnetism with magnetic moment of 380 emu/cc and coercivity of 200 Oe. Although the magnetic moment is lower than epitaxial Fe_3O_4, it is still better than polycrystalline Fe_3O_4 thin films. The results presented here could lead the pathway for new types of spintronic materials that are outside the family of Heusler alloys and dilute magnetic semiconductors, that are stable in ambient conditions,and that combine high conductivity and magnetism at room temperature.

5.2 Methods

Full details of film synthesis can be found in chapter 2 and in an earlier publication [17]. The film having R = Fe:(Tb+Dy) = 21 was used for this study. The details of cyclic annealing and characterization techniques can be found in chapter 2.

A second film of the same composition was annealed in a furnace (details in chapter 2) at 700 K in 10

mTorr for 18 hours. Optical transmission and sheet resistance measurements were performed on this film.

5.3 Results

Our studies were motivated by trying to understand the role of oxidation on the stability, transport, magnetic, and optical properties of FDTO films that have cation ratios different from the original Terfenol-D composition. For this study, an as-prepared film having ratio, R = Fe:(Tb+Dy) = 21 was selected because of its high Fe content. The hypothesis was that a mostly Fe-based film would allow better understanding of the role of the rare-earth (RE) elements since they can be considered as dopants based on their small amount in the film. In the study elaborated in chapter 4, a 40 nm thick film of R = 21 exhibited metallic behavior in the as-prepared state. For this study, a film of nearly 78 nm thickness with R = 21 was put through 14 annealing cycles from 300 K to 700 K in 5 mTorr pressure; no further annealing cycles were carried out because the resistivity of the film appeared to have stabilized. At each temperature, the resistivity of the film was measured *in-situ*, while both hall mobility and carrier concentration were also measured in addition to the resistivity for the 14^{th} cycle. Another film of the same composition was annealed inside a furnace at 700 K for 18 hours, to compare the change in properties of a one-step anneal against cyclic anneal. 18 hours were selected based on the total time the sample spent in the cyclic annealing process and approximating that the sample stayed at 700 K for ~30% of the time, based on the cyclic measurements. Magnetic and optical properties of the oxide film were measured. A cross-section of about 2 μm in length and ~80 nm in thickness was milled out using focused ion beam (FIB) for doing TEM analysis. (Details of electrical, optical, magnetic, TEM, and GIXRD measurements can be found in chapter 2).

The thickness of the film was confirmed in cross-sectional HR-TEM (high-resolution TEM) image shown in Fig. 5.1(a), where the R21-oxide film can be seen to have segregated into three separate regions as opposed to being in a homogeneous state. The microstructure of the three different layers were further investigated by doing FFT of the HR-TEM image in Fig. 5.1(b): FFT from the top 25 nm of the film showed amorphous rings (bottom right diffraction pattern in Fig. 5.1(b) taken from the area marked with the smaller yellow box), while that from the bottom 47 nm layer showed significant crystallinity (middle right diffraction pattern taken from the area marked with the larger yellow box). From the bright spots, the lattice parameter value was measured to be around 0.5 nm, which was close to that for Fe_3O_4, and so the conclusion can be drawn that the polycrystalline regions mostly belong to Fe_3O_4.From the HR-TEM image, the structure of the middle bright region seems to be a mix of amorphous and polycrystalline structure. Regardless, diffraction measurement shown in Fig. 5.1(d) was obtained from the bottom 47 nm film, with the particular region shown in Fig. 5.1(c).This confirmed the polycrystallinity of the bottom layer. In order to find out the origin of the amorphous rings in Fig. 5.1(d), diffraction pattern was obtained from the substrate SiO_2 only, and it was found to be amorphous, as shown in Fig. 5.1(e). The microstructure was independently probed by taking GIXRD measurements (black line in Fig. 5.1(g)), which showed some peaks that matched with the Ag metal peak positions (red lines in Fig. 5.1(g)) obtained from database. There was a small peak evident around 37 degrees, which was slightly above that obtained for epitaxial Fe_3O_4 (35.5) shown using dotted blue line in Fig.5.1(g) . This peak, combined with the information derived from the HRTEM image,

made the strong case that the film had a significant amount of polycrystalline Fe_3O_4. The diffraction peak for Fe_3O_4 in GIXRD might have shifted from the original position due to the different random orientation of the crystalline nano-clusters, the presence of Dy cations, and presence of some amorphous microstructure.

In order to check the homogeneity of the chemical composition of the R21-oxide film, EELS spectra were taken from three regions marked by green boxes in Fig. 5.2 (a), (b) and (c). In (a) and (b), Fe^{3+} cation was found everywhere, whereas the Dy^{3+} was seen to be concentrated right around the narrow, bright band seen in the HR-TEM image in the middle of the film. Fig. 5.2(c) shows the distribution of the Fe, O, and Dy along the depth of the film, demonstrating that there is a gradual decrease of oxygen from top to bottom, the Fe is distributed quite evenly except for a region in the middle, where the Dy distribution shows higher Dy concentration. In this EELS map too the Dy is seen to be present for about 20 nm below the dark band. The plot on the left-most inset of Fig. 5.2 shows the ratio Fe/O (on the x-axis) along the depth of the film. The plot shows that from the top of the film to about a depth of 55 nm, the Fe/O ratio is slightly lower than that of Fe_3O_4. Upon close inspection, it can be seen that in the regions between 33 nm to about 50 nm, the plot is pushed to lower values of Fe/O relative to the trend of the previous data points. This region corresponds exactly to where maximum Dy is found in the film, indicating that the region contains oxygen bonded not only to the Fe atoms but also to the Dy atoms. The values of Fe/O were not plotted beyond 66 nm because the software detected no oxygen in the last 10 nm of the film. This issue will be discussed shortly in this section. In the z-contrast images in (a), (b) and (c), the bright band from HR-TEM is seen as a dark band, which indicates that the middle region is has low Z value, and hence has more oxygen, than the top and bottom regions. The in-homogeneous distribution of the Dy^{3+} could be due to cation diffusion during the heating cycles. The z-contrast images also show the bottom 47 nm to be brighter than the top 25 nm, which could indicate a less oxidized system at the bottom than on the top. This is supported well by the oxygen map in Fig. 5.2(c).

The oxygen map also showed the bottom of the film to be completely deficient of oxygen. Since this could indicate a metallic state of Fe, the EELS spectrum from that region (marked by the red box in Fig. 5.2(c)) was inspected. From Fig. 5.2(d), it can be seen that while the major peak for O K-edge at 540 eV is visible, there is no signal for the pre-peak at 530 eV typically seen for iron oxides. In addition, it should be noted that no Tb was detected in any of the EELS spectra. Both of these results (i.e. the absence of oxygen pre-peak and the absence of Tb) could be due to the small signal intensity obtained at those energies due to the relatively high thickness of the FIB sample. Upon further inspecting the oxygen distribution in Fig. 5.2(c), the oxygen concentration is seen to drop right after the end of the dark band. This indicates that the dark band in the middle could be acting as a protective layer for the bottom 47 nm, which might explain the high-z values causing the region to appear brighter. The chemical composition of the surface of the film was investigated independently using XPS measurements. The XPS peaks for Fe 2p, and Tb and Dy 4d are shown in Fig. 5.2 (c) and (d) respectively. Both spectra confirmed the absence of metallic state of the elements. By quantification of the area under the peaks, the ratio of Fe^{3+}/Fe^{2+} was obtained to be 1.83, which is within 20% of that found in Fe_3O_4. In addition, it was evident from the Tb and Dy 4d spectrum that the film contained more Dy than Tb, with the Dy:Tb ratio found to be 8.1 from the quantification of the peaks. Therefore the top two layers can be described as $Fe_{3-x}O_4$ system interspersed with $Dy_{0.81}Tb_{0.19}$.

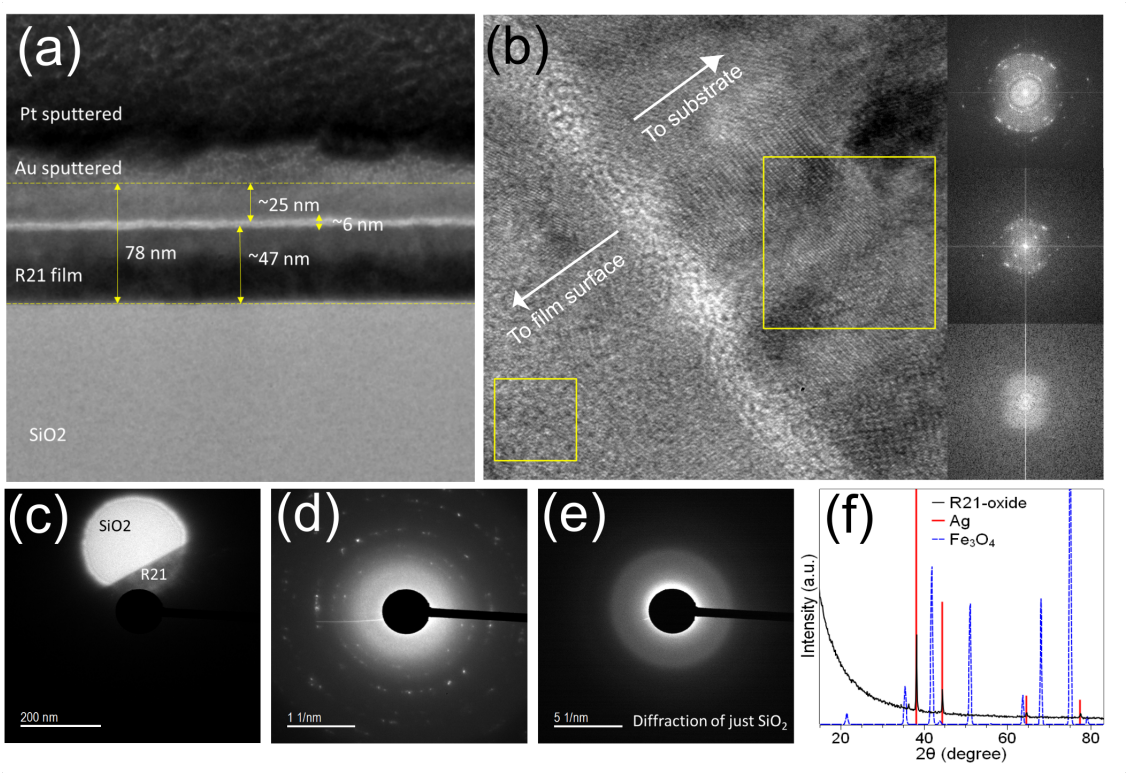


Figure 5.1: *(a) HR-TEM image showing cross-section of the R21-oxide film on top of the SiO_2/Si substrate. The top two layers show polycrystalline Pt and Ag sputtered (labeled) on top of the film to protect the film surface. The R21-oxide film has three distinct regions: a 25 nm top layer, a bright 6nm middle layer, and 47 nm bottom layer. (b) A zoomed-in HR-TEM image of just the R21-oxide film. The top surface of the film is on the left edge, and the bottom of the film is on the right. Yellow boxes mark regions where image FFT has been performed to get diffraction patterns; the top FFT image is taken for the entire sample, showing that the film has amorphous as well as polycrystalline regions. The second FFT image is from the bottom 47 nm of the film (area marked by the bigger yellow box) and shows polycrystallinity, while the third FFT image is from the top 25 nm of the film (area marked by smaller yellow box) and shows amorphous structure. (c) Z-contrast image of region containing bottom layer of R21-oxide and SiO_2 from where diffraction pattern in (d) has been obtained. The diffraction pattern shows polycrystalline features along with a diffused ring from amorphous structure. (e) Diffraction pattern of only SiO_2 layer to confirm that the amorphous ring in (d) was originating from SiO_2 layer. (f) GIXRD pattern obtained from the R21-oxide (black line) showing peaks, most of which overlap with Ag peaks (red lines) originating from the contact pads on the sample. There was a small peak around 37 degrees which corresponded closely to the 35.5 degree peak from Fe_3O_4.*

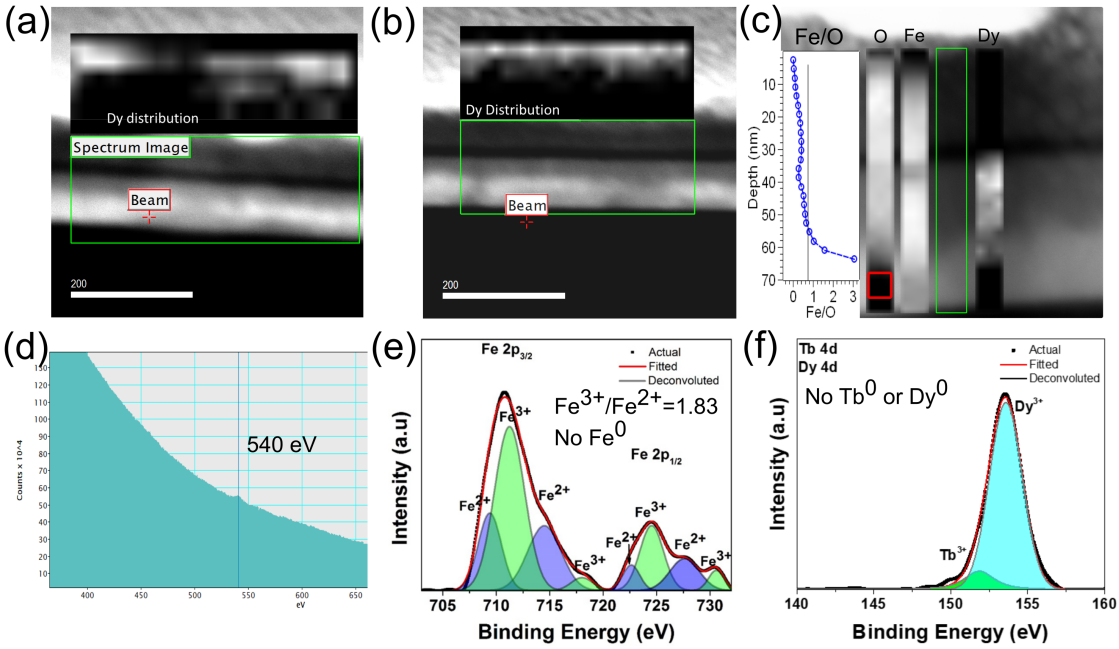


Figure 5.2: *(a)-(c) Z-contrast images of the R21-oxide film obtained by STEM detector. The green boxes mark regions from where EELS spectra were obtained. Insets for (a) and (b) show the Dy^{3+} distribution in the EELS region, while the insets for (c) show O^{2-}, Fe^{3+}, and Dy^{3+}distributions along the film depth. The left-most inset of (c) also shows plot of Fe/O along the depth of the film, where Fe/O is plotted on the x-axis and the depth values in nm are plotted along y-axis for ease of visual representation; the black line in the plot marks the Fe/O value of 0.75 found in Fe_3O_4. (d) EELS spectrum from the oxygen deficient region marked with red box in (c), showing the presence of the major O K-edge peak at 540 eV but not the pre-peak that is usually present for all iron oxides at 530 eV. (e), (f) XPS peaks for Fe 2p, and Tb and Dy 4d respectively, both showing the absence of the elements in their metallic state. Quantification of the Fe peak gave the Fe^{3+}/Fe^{2+} ratio as 1.83.*

Since this kind of phase segregation in the final oxide film was unexpected, it was important to investigate how the transport properties of the film evolved with each annealing cycle. Figure 5.3(a) shows the evolution of resistivity with each annealing cycle. In cycle 1, where the material was in the as-prepared state, the resistivity increased with increasing temperature up to 550 K indicating metallic behavior, and then started decreasing after 550 K exhibiting a more semiconducting behavior. This trend continued until the fifth heating cycle, with a metal to insulator transition (MIT) occurring at 550 K, i.e. the slope of the curve changed from positive to negative at around 550 K. However, the MIT occurred at a much higher temperature in cycle two - a behavior that was not repeated or observed in any other cycle. After the fifth cycle the resistivity decreased with increasing temperature for the entire temperature range, with three different slopes evolving in the plots. By the 13^{th} cycle, the plots had three distinct regimes - steep decrease in resistivity from 300 K to 350 K, followed by a flatter slope until 550 K, and then a steeper negative slope again. The transition points can be seen more clearly in the inset, which plots the derivative of the resistivity with respect to temperature. The possible explanation behind these three regimes will be discussed later in this section. Figure 5.3(b) shows the room temperature resistivity to have stabilized after 13 cycles

at a value which was almost ten times larger than that of the as-prepared state; however, even this final stable resistivity of 0.7 mohm-cm is still two orders of magnitude lower than that for epitaxial Fe_3O_4 (10 mohm-cm) [7, 32]. In contrary, a second R21 film that was annealed inside a furnace at 700 K in ~10 mTorr for 18 hours showed completely insulating behavior. This indicated that cyclic annealing in a lower partial pressure of oxygen produced very different films compared to one-step annealing at higher oxygen partial pressure (atmosphere) at the same maximum temperature for a long time period, i.e. if the film had been sitting at 700 K for 30% of the total time required for 14 heating and cooling cycles. Resistance measured at low temperature for the R21-oxide film from cyclic annealing displayed a minimum at around 120 K and hysteresis below that, as shown in Figure 5.3(c). The dip in resistivity is very similar to the Verwey transition [78] that takes place at around 125 K for Fe_3O_4, suggesting that the overall transport behavior of the film is close to that of Fe_3O_4. The observed hysteresis could be due to some form of phase transition occurring in the polycrystalline layer of the film. No such transition was seen in the as-prepared film where the resistivity at low temperature demonstrated the typical positive slope expected for a metallic film, as seen in the inset of Figure 5.3(c).

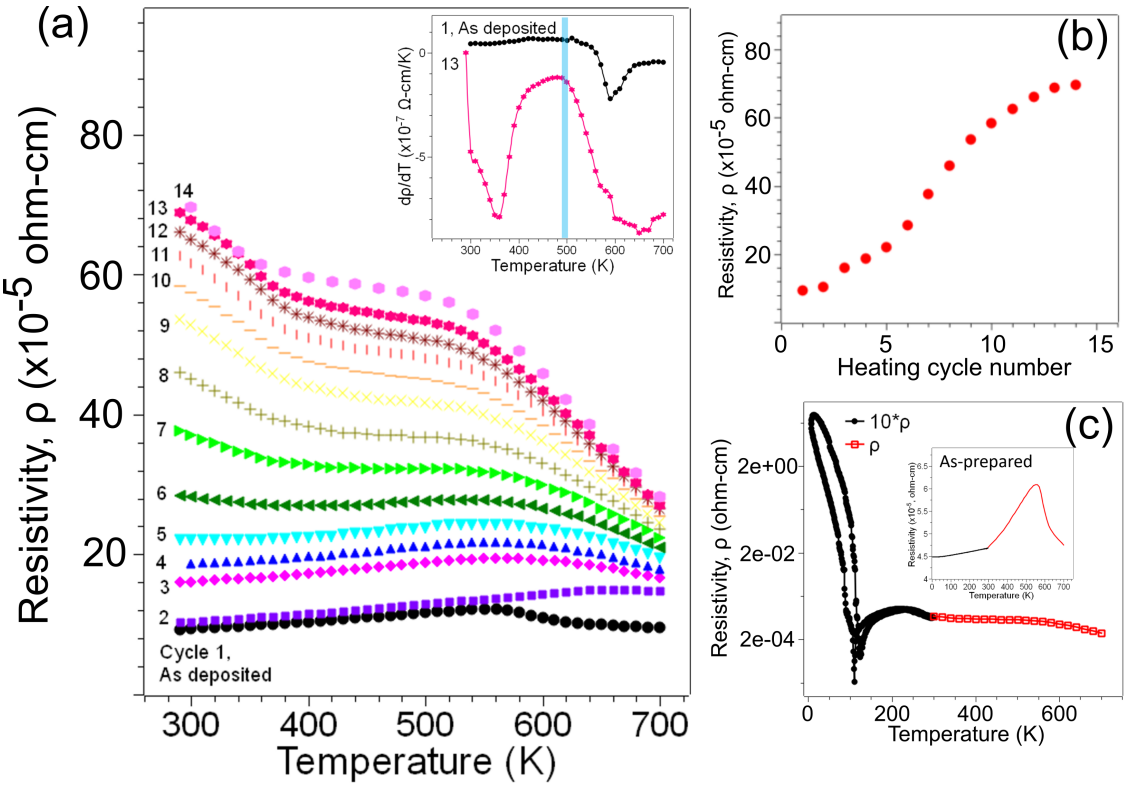


Figure 5.3: *(a) Evolution of resistivity with different annealing cycles for FDTO film with R = 21; (b) Room temperature resistivity, i. e. at the beginning of each cycle, vs number of heating cycles, showing a stabilization of resistivity of the film. (c) Resistivity of the post-annealed film from 10 K to 700 K, showing a sharp transition from semiconducting to metallic behavior around 100 K and back to semiconducting behavior around 250 K. There is also a hysteresis present below 100 K. Inset shows resistivity of the as-prepared film, showing metallic behavior from 3 K to about 550 K.*

The hall mobility and carrier concentration of the film were also measured *in-situ* as a function of

temperature for the 14th heating cycle. As seen in Figure 5.4(a), the mobility is p-type and the measured values are greater than 20 cm^2/V-s for the studied temperature regime. This is much higher than reported p-type hall mobilities in other oxide semiconductors [131, 132]. However, since the ratio of Fe^{3+}/Fe^{2+} and the dip in resistivity at 120 K hinted the film to be very close to Fe_3O_4, some magnetism might be present in the film. Therefore hall measurement (ex-situ) of the post annealed film at high magnetic fields was carried out to check for the presence of anomalous hall effect (AHE). The film was found to exhibit AHE, as shown in the inset of Figure 5.4 (a). From the plot of R_{xy} vs B field, the mobility due to anomalous hall effect (AHE) was calculated to be 25.1 cm^2/V-s while that due to ordinary hall effect (OHE) was found to be 1.72 cm^2/V-s.

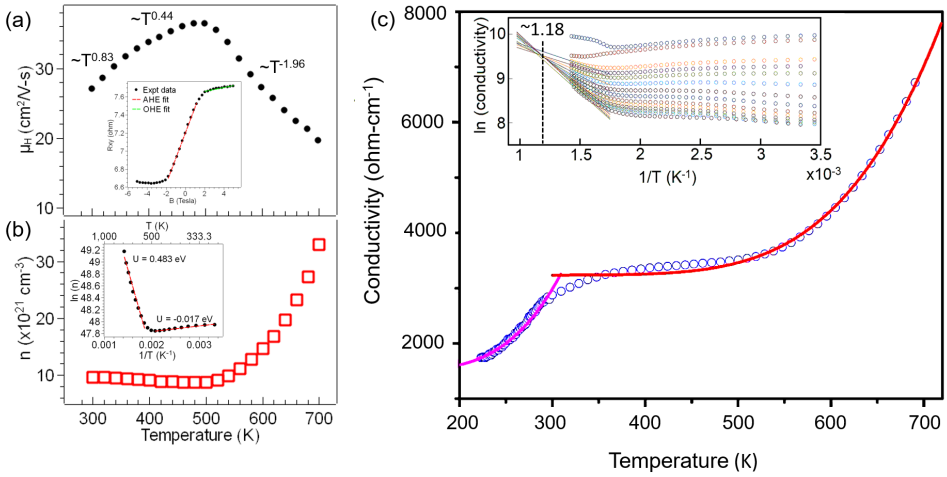


Figure 5.4: *(a) Hall mobility as a function of temperature with three different regimes following $T^{0.83}$, $T^{0.44}$, and $T^{-1.96}$; inset shows hall resistance (R_{xy}) vs magnetic field plot of the post-annealed film, demonstrating the presence of anomalous hall effect. (b) Carrier concentration as a function of temperature shows two distinct regimes; inset is a plot of ln n vs 1/T from where values of activation energies were obtained for the two regimes. (c) Plot of conductivity vs temperature for the low temperature (200 K-300 K) and high temperature (300 K-700 K) regimes, showing fits to different conduction models for each regime: the purple fit from 200-300 K shows variable range hopping while the red fit from 300-700 K shows conduction by delocalized states. Inset shows the plot of ln(conductivity) vs 1/T where the plots were extrapolated to obtain the focal temperature T_C.*

In the plot of log μ vs T for crystalline semiconductors, the first half of the mobility where the mobility increases as a function of temperature is dominated by ionized impurities and follows $T^{3/2}$. In this regime the electrons gain more velocity as temperature increases and so they are able to overcome the scattering due to ionized impurities. This leads to an increase in mobility with increasing temperature. However after a certain temperature, mobility starts to decrease with increasing temperature due to phonon contributions. The mobility follows $T^{-3/2}$ for acoustic phonons and $T^{-1/2}$ for optical phonons. In the case of the R21-oxide, the log μ vs log T plot in the inset of Fig. 5.4(a) shows three different regimes of temperature dependence: $T^{0.83}$, $T^{0.44}$ and $T^{-1.96}$ in that order. Although this is not the typical expected T dependence, the high temperature regime is similar to that observed for traditional semiconductors such as Si and Ge [133]. The increase in mobility was slower than what is observed in typical semiconductors and this could be due

to the mixed amorphous-polycrystalline nature of the material which contains more ionized impurities than normal. It was concluded that the maximum seen in the mobility vs temperature plot is not due to a magnetic transition such as the Curie temperature because the drop in the mobility value past 550 K would have been sharper as the mobility due to the much higher AHE contributions (15 times higher than the OHE) would have been suppressed.

Fig. 5.4 (b) shows the carrier concentration having two regimes as well: from RT to about 500 K the carrier concentration decreased very slightly while it rapidly increased after 500 K. According to [134] if a model of thermal activation of carriers from defect states to band states holds true then

$$n = n_0 e^{\frac{-U}{k_B T}} \tag{5.1}$$

where U is the activation energy related to the position of the acceptor level (in the case of p-type conduction) relative to the valence band edge[134]. A fit of ln(n) vs 1/T plot (inset of Fig. 5.4(b)) gives $U = 0.483$ eV for the high temperature regime and -0.017 eV for the low temperature regime.

To understand what is happening to the film with each heating cycle, we recall that for undoped n-type a-Si:H and p-type a-Ch, conduction at high temperature occurs in the conduction band extended states and valence band extended states respectively [135]. As explained by Singh and Shimakawa [135], this yields a temperature dependence of conductivity for electrons as $\sigma = \sigma_0 exp(-\Delta E/kT)$, where $\Delta E = E_C - E_F$, i.e. the activation energy given by the difference between the Fermi energy E_F and the mobility edge at the conduction band E_C. The pre-exponential factor correlates with the activation energy as $\sigma_0 = \sigma_{00} exp(\Delta E/E_{MN})$, where $\sigma_{00}$is a constant and E_{MN} is a characteristic Meyer-Nedel energy [135]. The Meyer-Neldel characteristic energy is interpreted as $T_C = E_{MN}/k$, where T_C is the focal point in temperature where σ approaches σ_{00} for all doping concentrations. The inset in Figure 5.4 (c) shows that a focal point in temperature can be derived upon extrapolating the conductivity plots for each heating cycle for the R21 film. In our case, the T_C value comes out to be 847 K, which corresponds to a Meyer-Neldel energy of 0.073 eV. Therefore with each heating cycle, the carrier concentration in the material is changing possibly due to continuous oxidation of the three metallic elements from the as-prepared state until a stable state is reached.

The conduction mechanism of the post cyclic-annealed film is hypothesized to be dominated by variable range hopping in the range of 200 K to 300 K, and by delocalized states for temperatures above 300 K. This can be seen from the fitting applied to the low and high temperature conductivity data in Figure 5.4(c). In the low temperature regime (200-300 K), the dominant transport mechanism can be assumed to be near the E_F and the DC conductivity can be modeled as $\sigma_{DC} = \frac{\sigma_0}{\sqrt{T}} exp[-(\frac{T_0}{T})^{\gamma}] + \sigma_{offset}$, where σ_0 is a constant, T_0 is a temperature related to the density of states at the Fermi surface, σ_{offset} is a conductivity offset due to the intrinsic resistivity of the contacts, and γ is related to the dimensionality of the localized states in the valence band. The model predicts a value of $T_0 \sim 2.0\,eV$ and $\gamma = 0.55$.

The high temperature conductivity (>300 K) is assumed to be dominated by delocalized states, which can be modeled as $\sigma_{DC} = \sigma_0 exp[-\frac{T_0}{T}] + \sigma_{offset}$,where T_0 corresponds to the activation energy of the system and $\sigma_0 = \sigma_{00} exp(\frac{T_0}{T_C})$. This T_c refers to temperature corresponding to the Meyer-Neldel energy as already found to be 847 K or 0.073 eV. Thus using that value of T_C and the delocalized states model, the T_0 is found to be 0.425 eV, which is in close agreement to the activation energy of 0.483 eV obtained from the carrier

concentration analysis.

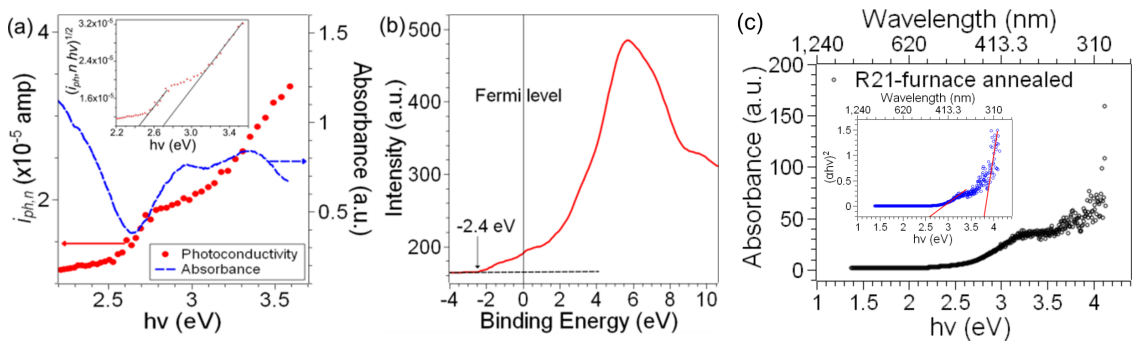


Figure 5.5: *(a) Plot of photoconductivity (red filled circles; left y-axis) and absorbance (blue dotted line; right y-axis) as a function of photon energy. Absorbance follows the photoconductivity after 2.5 eV, which is roughly the start of localized states. Onset of delocalized states start at 2.9 eV, confirmed by the Tauc plot analysis in the inset, where the bands are found to be parabolic (b) Valence band maximum analysis from XPS, showing non-zero intensity at the Fermi level, meaning the Fermi level is below the valence band. This confirms: (i) the film is a p-type semiconductor, with conduction happening within the valence band, (ii) there are degenerate states inside the valence band. (c) Optical absorbance of the R21 film that was furnace-annealed. Inset of Tauc plot shows two bandgaps - one around 2.6 eV and the second one around 3.8 eV.*

Since the R21-oxide films by cyclic annealing showed very low resistivity, while the film that was furnace annealed turned insulating, it was necessary to investigate their bandgaps. The photoconductivity and absorbance plots of the R21-oxide film by cyclic anneal is shown in Fig. 5.5(a). The inset shows Tauc plot analysis of the photoconductivity data, revealing that the localized states start at ~2.5 eV while the delocalized states begin at ~2.9 eV. This is consistent with the absorbance plot also showing an increase at around 2.5 eV, further confirming the localized states to be below the delocalized states, and giving a bandgap of 2.5 eV for the film. Upon comparing this to the absorbance of the furnace-annealed film shown in Fig. 5.5(c), it can be seen that both the films have a bandgap at around 2.5 eV, found from the Tauc plot in the inset, due to the localized states.

However, the furnace annealed film has an additional bandgap at 3.8 eV. Since the bandgap of Tb_2O_3 is 3.8 eV and that for Dy_2O_3 is 4.9 eV, this second bandgap might arise from the lanthanides. From this observation, it can be concluded that the distribution of the Lanthanide atoms in the iron oxide matrix play an important role in the final transport properties of the films. Valence band maximum (VBM) analysis from the XPS measurement was done to determine the position of the valence band edge relative to the Fermi level.From Fig. 5.5(b) it can be seen that the Fermi level is inside the valence band for the cyclic annealed film. This not only confirms that the final film is a p-type semiconductor, but also indicates that there are degenerate states present, which could lead to the high carrier concentration values in the order of 10^{21} for this film.

Because the R21-oxide film showed evidence of anomalous hall effect during transport measurement, it was important to fully characterize the film's magnetic properties. Fig. 5.6(a) shows the room temperature magnetic moment of the R21-oxide film with magnetic field applied both in-plane (IP; black filled circles)

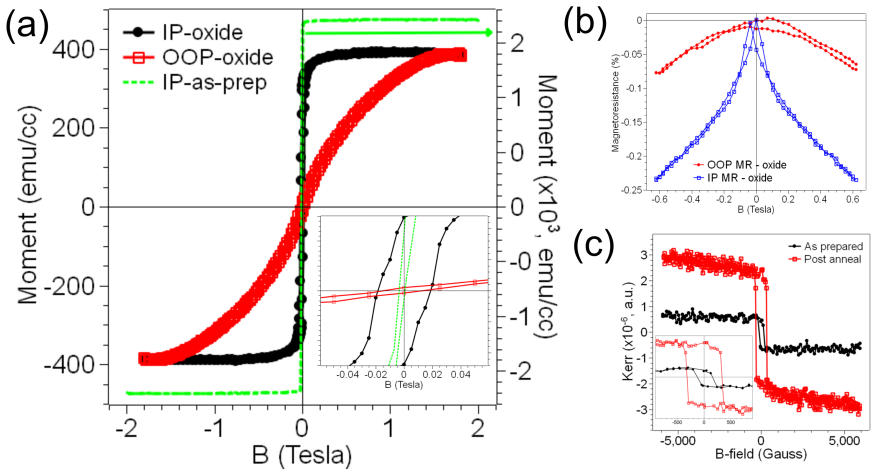


Figure 5.6: *(a) Plot of magnetic moment as a function of magnetic field for the oxide film (left y-axis; black filled circles – in-plane; red open squares – out-of-plane), and for as-prepared film (right y-axis; green dotted line – in-plane). The IP and OOP moment for the post-annealed film was about 380 emu/cc, much lower than that for the as-prepared film (~1700 emu/cc), but very close to that of epitaxial Fe_3O_4 (480 emu/cc). Coercivity for the post-annealed film (~200 Oe) was higher than that for the as-prepared film (~20 Oe) shown in the inset. (b) %MR for the oxide film showing IP MR (blue open squares) to be higher than OOP MR (red filled circles); however both are very small compared to that for epitaxial Fe_3O_4. (c)Plot of Kerr measurement as a function of magnetic field for the as-prepared (black filled circles) and R21-oxide (red open squares) films. Kerr data supports the magnetization data in that the coercivity of the oxide film was higher than that for the as-prepared film, as showing in the inset.*

and out-of-plane (OOP; red open squares). The saturation moment for both IP and OOP was about 380 emu/cc. This was significantly lower than the saturation moment of ~1700 emu/cc of the as-prepared film, shown as green dotted line (right y-axis) in Fig. 5.6(a). However, the final moment of the oxide film was very close to that for epitaxial Fe_3O_4 (470 emu/cc) [7, 32] and higher than polycrystalline Fe_3O_4 (280 emu/cc) [7]. The inset shows the coercivity of the oxide film (~200 Oe) to be higher than that for the as-prepared film (~20 Oe). Magnetoresistance (MR) for the oxide film was found to be less than -0.25% with magnetic field applied both parallel and perpendicular to the plane of the sample, as seen in Fig. 5.6(b); this value is much lower than that in Fe_3O_4 (approximately -6% at 285 K [7, 32]). The low %MR could be a result of the in-homogeneous distribution of the lanthanide cations in the film. Finally, Kerr measurements made on the as-prepared and oxide films, shown in Fig. 5.6(c) also confirmed the presence of room temperature magnetism in the oxide film.

5.4 Discussion and conclusion

There were several findings from this cyclic annealing study. First, the cyclic anneal resulted in a microstructure that had a gradient of crystallinity along the film depth, going from polycrystalline to amorphous state from the region in contact with the underlying amorphous SiO_2 substrate to the surface. In addition, there was a distinct band near the center of the film that had higher concentration of Dy^{3+} than anywhere else in

the film. This could suggest that with each anneal cycle, oxygen diffused from the surface downward while the Dy^{3+} cation diffused upward from the bottom of the film. This process slowed down once 700 K was reached and the film was cooled down to room temperature, causing the cations to be stationary in their positions. In the next anneal cycle, the same diffusion process repeated, with the cations starting off from where they were stationed at the end of the previous cycle. In this way, by 14 annealing cycles, the system stabilized to the state where (i) all the elements were completely in their oxide states, and (ii) most of the Dy cations migrated to a little above the center of the film. This diffusion of the Dy and oxygen atoms to the middle could have created a protective layer than prevented further oxidation on the bottom layer. Thus the stable state might be dictated by the formation of this protective highly-oxidized layer in the middle.

Second, this method of annealing was strikingly different from the furnace anneal where the film remained at 700 K for an extended period of time, thus maintaining the system at sufficient energy for the cations and oxygen to diffuse for a long period of time. This form of annealing might result in a more homogeneous microstructure and chemical composition, but certainly had undesirable transport properties of becoming an insulator. In addition, the absorbance of this furnace-annealed film revealed a second bandgap at 3.8 eV, which was absent in the cyclic annealed film. This could be the result of a different distribution of the lanthanide cations throughout the iron oxide matrix. Thus from these observations it can be concluded that the lanthanides play an important role in the final transport properties of the oxide films.

Perhaps the most important finding of this study, from an application perspective, is a new technique of annealing metallic films, which is capable of resulting in a completely oxidized system that is stable in ambient environment over time, is highly conductive and magnetic at room temperature. With an increased focus of the electronics industry to make memory and switching devices that are faster and more energy efficient, there is a constant need for new materials that are conducting and magnetic at room temperature. This particular Fe_{21} $Dy_{0.81}$ $Tb_{0.19}$ oxide could find application in spintronic devices, while the technique of cyclic annealing could be applied to other materials to obtain desirable functional properties.

5.5 Acknowledgments

This work was primarily supported by ARO grant W911NF-13-1-0428. H.T acknowledges Prof. Tatiana Allen at the University of Tennessee-Chattanooga for the cyclic anneal measurements, Dr. Gerd Duscher and Chenze Liu for the TEM imaging and EELS analysis, Dr. Tamil Sakthivel and Dr. Sudipta Seal at the University of Central Florida for the XPS measurements and analysis, Dr. Ashutosh Tiwari and Kun Tian at the University of Utah for the low temperature resistivity, magnetoresistance and magnetic hysteresis measurements, Dr. Hernando Garcia at the Southern Illinois University Edwardsville for the photoconductivity and absorbance measurement and analysis, and Dr. Rupam Mukherjee and Krishna Koirala at the University of Tennessee-Knoxville for the anomalous hall effect measurement.

Chapter 6

Effect of oxygen growth pressure on transport, magnetism, and optical properties of amorphous $Fe_{0.66}Dy_{0.24}Tb_{0.1}$-oxide

6.1 Summary

This chapter presents the study of the change in physical, chemical, transport, optical, and magnetic properties of thin films of $(Fe_{0.66}Dy_{0.24}Tb_{0.1})_2O_{3-x-y}$, where x = $Fe^{2+}/(Fe^{3+}+Fe^{2+})$ and y = $Tb^{3+}/(Tb^{3+}+Tb^{4+})$, deposited by PLD, as a function of varying oxygen pressure during growth. Upon characterizing the films, it was found that although all the films were in their completely oxidized states, the conductivity and magnetic moment of the films increased with decreasing oxygen pressure, such that at pressures higher than $1x10^{-5}$ Torr, the films were insulating and non-magnetic at room temperature. The direct optical bandgap increased from ~2.5 eV to about ~3.2 eV while the indirect bandgap increased from ~1.5 eV to ~2.9 eV with increasing oxygen pressure. The changes in the transport, magnetic, and optical properties can be correlated to an increase in the Fe^{2+}/Fe^{3+} ratio in the films as oxygen pressure decreases. This was accompanied by the presence of Tb_4O_7 in the films, indicating mixed valence states of Tb - an information that cannot be ignored since from the previous chapters it was seen that the lanthanides play a crucial role in the final transport properties of the film. The findings from this chapter can help determine growth parameters to be used when depositing FDTO films in order to achieve properties desired for spintronic applications.

6.2 Methods

Thin films (20-30 nm) of FDTO were deposited using pulsed laser deposition. A KrF excimer laser was used with wavelength of 248 nm, rep rate of 10Hz, and energy density of 1 J/cm^2. The target was commercially available metal alloy Terfenol-D (66%Fe, 24%Dy, 10%Tb), that was polished using a sandpaper prior to

mounting on the target holder. Quartz substrates were used to allow for transport, magnetic, and optical measurements on the films, as well as for GIXRD, XRR, TEM, and XPS. The substrates were cleaned by sonicating in acetone and IPA for ~7 minutes each, and then drying with N_2 gun. The substrates were mounted on the substrate holder using regular double-sided tape. After inserting both the substrates and the target inside the chamber, the chamber was pumped down to the desired deposition pressure. However, to make sure the environment inside the chamber is oxygen-rich, oxygen gas was leaked inside the chamber until the pressure inside the chamber was slightly higher than the final deposition pressure. Then using a combination of the gate valve the and the oxygen leak valve, the pressure inside the chamber was maintained at the desired deposition pressure. This ensured that the film growth would take place in an oxygen rich environment. Next, the target holder rotation was started and the target was pre-ablated (with the shutter covering the substrate) for one minute to remove any surface impurities. The shutter was then removed and timer started for deposition. After every 5 minutes, the target was moved slightly to allow deposition from a fresh area - this made sure the stoichiometry of the target surface was not changing and also any one particular region on the target was not getting more surface roughness than the rest. The entire process took place at room temperature as there was no substrate heating involved. Once deposition was done, the samples were promptly removed.

A wide range of oxygen pressures were used for this study: $5x10^{-7}$ Torr; 1.5, 2, 3, 4, $5x10^{-6}$ Torr; $1x10^{-5}$ Torr; $1x10^{-4}$ Torr; and $1x10^{-3}$ Torr. The following characterizations were done on the films (with more details provided in chapter 2):

- XRR: for density and thickness of the films
- TEM: microstructure and chemical composition
- XPS: chemical composition, valence band maximum, work function
- 4-probe sheet resistance
- Resistance vs Temperature from 3 K to 300 K
- SQUID for measuring magnetic moment
- Magnetoresistance (MR) and anisotropic MR (AMR)

6.3 Results

6.3.1 Chemical composition and microstructure

Following film deposition (~ 1 to 2 hours typically), the FDTO films were characterized using XRR to obtain the film thicknesses and the respective densities. Fig. 6.1 shows the thicknesses to typically lie between 20 to 30 nm with densities ranging between 5 to 5.8 g/cm^3. There is a slight trend of the densities decreasing and thickness values increasing as O_2 deposition pressure increases. Given that the deposition times were kept constant, the increase in the thicknesses was attributed to increasing volume with increasing O_2 pressures as a result of higher oxygen incorporation.

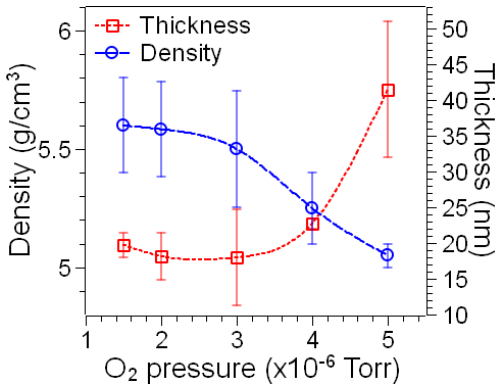


Figure 6.1: *Plot of density (blue open circles; left y-axis) and film thickness (red open squares; right y-axis) as a function of O_2 pressure. The lines are meant as a guide for the eye. Density values stayed ranged from 5 to -5.8 g/cm^3 while thickness values stayed ranged between 20 to 30 nm.*

Next, TEM measurements were performed on the film deposited at 1.5x10^{-6} Torr since that had the highest density. One of the main concerns with the FDTO films was the presence of metallic nanoclusters at low O_2 pressure: for this purpose the 1.5x10^{-6} Torr film was appropriate too. The HR-TEM image of this film in Fig. 6.3(a) shows an amorphous FDTO layer and polycrystalline Au layer on top. The amorphous microstructure of the FDTO layer was confirmed by the diffused rings seen in the nano-diffraction pattern (lower left inset) from the area marked by yellow circle in the FDTO layer. EELS spectra were taken from the region marked by the green rectangle, and the spectra were analyzed according to peak positions described in chapter 3 to get the distribution of the three metal cations. Some regions near the film surface were identified with higher iron than throughout the bulk of the film. However, no metallic iron was observed in those regions. Because the TEM sample was made using FIB, it was inconclusive whether the contrast near the surface of the FDTO film seen in the HR-TEM image was a result of ion bombardment from the FIB or if it was there in the original as-prepared film too. The lack of metallic states of any of the three elements confirmed that any transport and magnetic properties of the FDTO films would arise from an oxide material free of any metallic nanoclusters. Independent XPS studies were performed on all the films to look at their chemical compositions at the surface. The peaks obtained from Fe 2p, Tb and Dy 4d, and O 1s for all the samples are show in Fig. 6.2. It should be noted that no metallic peaks were seen from Fe, Tb, and Dy - a Tb metal peak causes a double peak to appear around 151 eV, which was absent in all the spectra. Given the susceptibility of Dy to oxidize, fitting done without Dy metal peaks had good fit to the experimental data. The absence of metal also supported the chemical compositions obtained from the EELS analysis. Although the Fe^{2+} and Fe^{3+} peaks could be decoupled during fitting, it was more difficult to segregate the different cation states for the lanthanides. However, the peak positions that best fit the 4d spectra were at 151.6±0.2 eV from Tb_4O_7 (a mixed phase of Tb^{3+} and Tb^{4+}) and at 154.7±0.1 eV from Dy_2O_3. These peak positions were obtained from the standard XPS database [136].Quantification of the cation peaks were carried out and the cation percentages were calculated as follows and then plotted as a function of O_2 pressure in Fig.6.3(b):

$$\%Fe^{2+} = \frac{Area\,under\,Fe^{2+}\,peak}{Total\,area\,under\,Fe\,2p\,peaks} * 100;\ \%Fe^{3+} = 100 - \%Fe^{2+} \tag{6.1}$$

$$\%Dy^{3+} = \frac{Area\,under\,Dy^{3+}\,peak}{Total\,area\,under\,Tb\,and\,Dy\,4d\,peaks} * 100;\ \%(Tb^{3+}, Tb^{4+}) = 100 - \%Dy^{3+} \qquad (6.2)$$

Fig. 6.3(b) shows the Fe^{2+} decreasing and Fe^{3+} increasing with increasing oxygen pressure - this is reasonable since more oxygen in the environment leads to more oxidation of the Fe. In addition, the %Tb was found to decrease and %Dy found to increase with increasing oxygen pressure. To further analyze this, the ratio of Fe^{3+}/Fe^{2+}, and $Dy^{3+}/(Tb^{3+},Tb^{4+})$ was plotted as a function of O_2 pressure in Fig.6.3(c). While Fe^{3+}/Fe^{2+} is seen to increase with increasing O_2 pressure, the more important aspect to note are the values - all the films are richer in Fe^{2+} compared to in Fe_3O_4, where the ratio of Fe^{3+}/Fe^{2+} is 2. In addition, the $Dy^{3+}/(Tb^{3+},Tb^{4+})$ was lower than the stoichiometry of Terfenol-D target (i.e. 2.4) for all the deposited films. However, the PLD deposition maintains stoichiometry, so the different value of Dy/Tb obtained from XPS must either be a surface effect or an artifact of data analysis and measurement.

6.3.2 Transport and magnetism

Once it was confirmed that the films were completely oxidized, transport and magnetic properties of the film were probed since those are two most important parameters for spintronic device applications. Fig. 6.5(a) shows plots of magnetic moment (left y-axis) and resistivity (right y-axis) of the films as a function of temperature. The magnetic moments were obtained from magnetic hysteresis loops taken at room temperature and shown in Fig. 6.4(a). The moment was seen to decrease in the FDTO films while the resistivity was seen to increase with increasing O_2 pressure. The inset of Fig. 6.5(a) shows that after $1x10^{-5}$ Torr, the films become insulating (shown as data points corresponding to the maximum measurement limit of the instrument) and non-magnetic (such that magnetic hysteresis loops in SQUID could not be measured). Both of these could be result of increasing amount of Fe^{3+} in the films. Moreover, the higher oxygen incorporation could also change the ratio of Tb^{3+} and Tb^{4+} in the films, which could not be decoupled from the XPS peak analysis. Given the high magnetic moment carried by the Tb cations, this could also cause the changes in the magnetism. The coercive field was also seen to increase with increasing O_2 pressure as seen in the inset of Fig. 6.4(a); this is consistent with magnetoresistance data in Fig. 6.4(b), where the coercive field is higher for the FDTO film deposited at $4x10^{-6}$ Torr compared to that at $2x10^{-6}$ Torr. The %MR was seen to be positive in these films (~1%), and the magnitude was lower than that reported for Fe_3O_4 (6%). To independently eliminate the possibility of Fe metal atoms being the origin of magnetism, XMCD measurements were performed on the film deposited at $2x10^{-6}$ Torr. The split peak appearing in the XAS data in the top panel of Fig. 6.5(b) showed the presence of Fe^{3+} in the film. The XMCD measurement shown in the bottom panel of the same figure showed the XMCD signal also appearing at the same energy as the Fe^{3+} peak in XAS, thus correlating the origin of magnetic to be Fe^{3+} and not Fe^0.

To check if the FDTO films were metallic or semiconducting, and also to investigate at what O_2 pressure they become semiconducting if any of the low pressure films were metallic, temperature dependent resistance measurements were done from 3 K to 300 K, starting with the film that was deposited at $5x10^{-6}$ Torr. The resistance vs temperature curve for this, shown in Fig. 6.5(c) displayed semiconducting behavior with resistance decreasing with increasing temperature. The same behavior was observed for the film de-

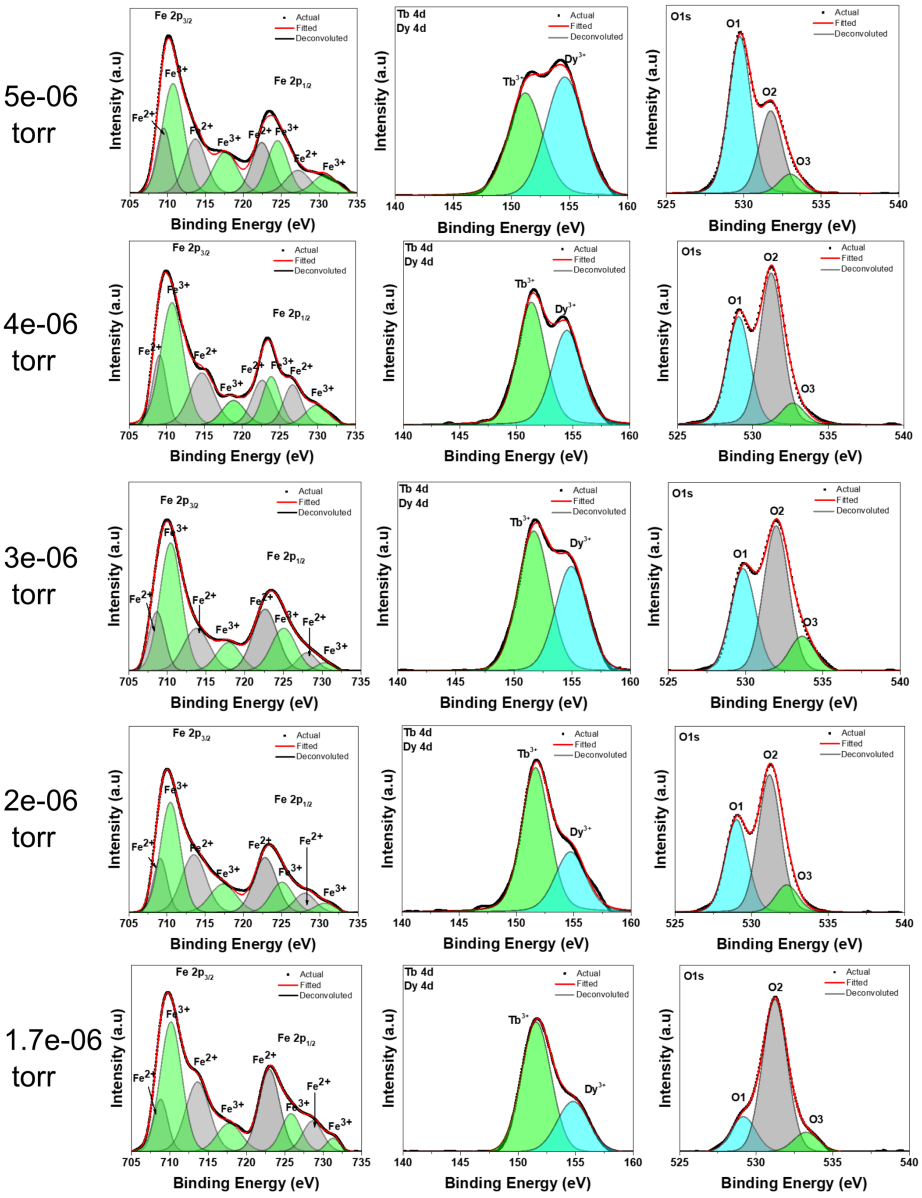


Figure 6.2: *Figure panel showing XPS peaks obtained from FDTO films deposited at pressures from 5x10^{-6} Torr to 1.5x10^{-6} Torr. The columns represent Fe 2p, Tb and Dy 4d, and O 1s from left to right respectively, while the rows represent different oxygen pressures (labeled) from 5x10^{-6} Torr to 1.5x10^{-6} Torr from top to bottom.*

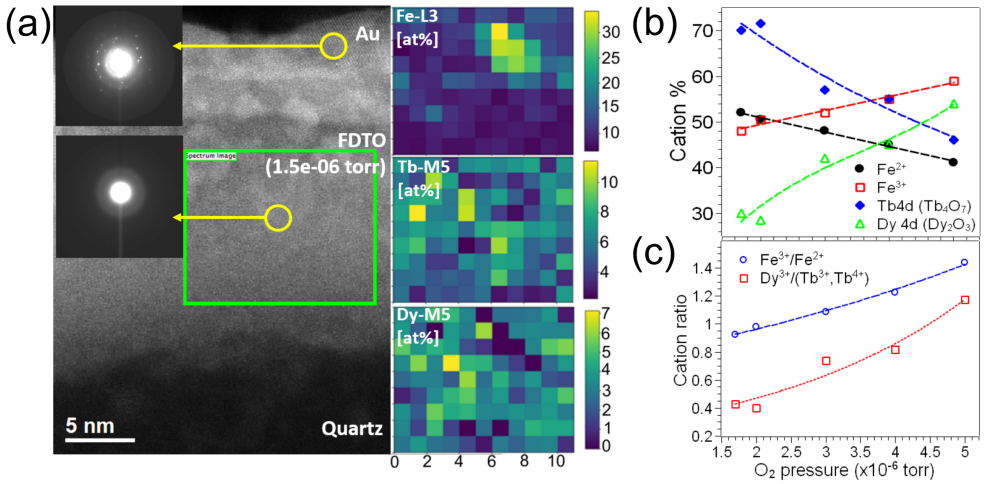


Figure 6.3: *(a) HR-TEM cross-section image showing FDTO layers deposited at 1.5x10^{-6} Torr on quartz substrate. Thin layer of Au was sputtered to protect the surface of FDTO film. The yellow circles show the areas from where the nano-diffraction patterns were obtained (left insets) showing polycrystallinity in Au and amorphous rings in FDTO. Panels on the right of the TEM image show the elemental distribution of Fe, Tb, and Dy, obtained from EELS spectrum of the area inside the green box. EELS also confirmed the absence of any metallic Fe. (b) Relative percentage of the different cation peaks obtained from XPS: %Fe^{2+} and %Tb^{3+} from Tb_4O_7 increase with decreasing O_2 pressure. (c) Plot of the ratios Fe^{3+}/Fe^{2+} (blue open circles) and $Dy^{3+}/(Tb^{3+},Tb^{4+})$ (red open squares) as a function of O_2 pressure. Fe^{3+}/Fe^{2+} is seen to increase with increasing O_2 pressure, however, the ratio is smaller than that in Fe_3O_4 (i.e. 2), indicating that the FDTO system is more rich in Fe^{2+} than the Fe_3O_4 system for the O_2 pressure in the 10^{-6} Torr regime. $Dy^{3+}/(Tb^{3+},Tb^{4+})$ increases with increasing O_2 pressure, which is an artifact of analysis.*

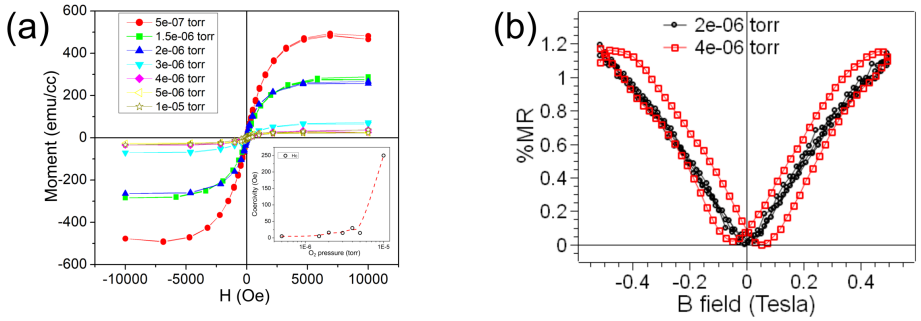


Figure 6.4: *(a) Plot of magnetic hysteresis loops for FDTO films deposited at different oxygen pressures; inset plots the coercive field as a function of O_2 pressure, showing the coercivity to increase with increasing O_2 pressure. (b) Magnetoresistance (%) plotted for FDTO films deposited at 2x10^{-6} Torr (black open circles) and at 4x10^{-6} Torr (red open squares). The %MR also indicates an increase in the coercive field as O_2 pressure is increased.*

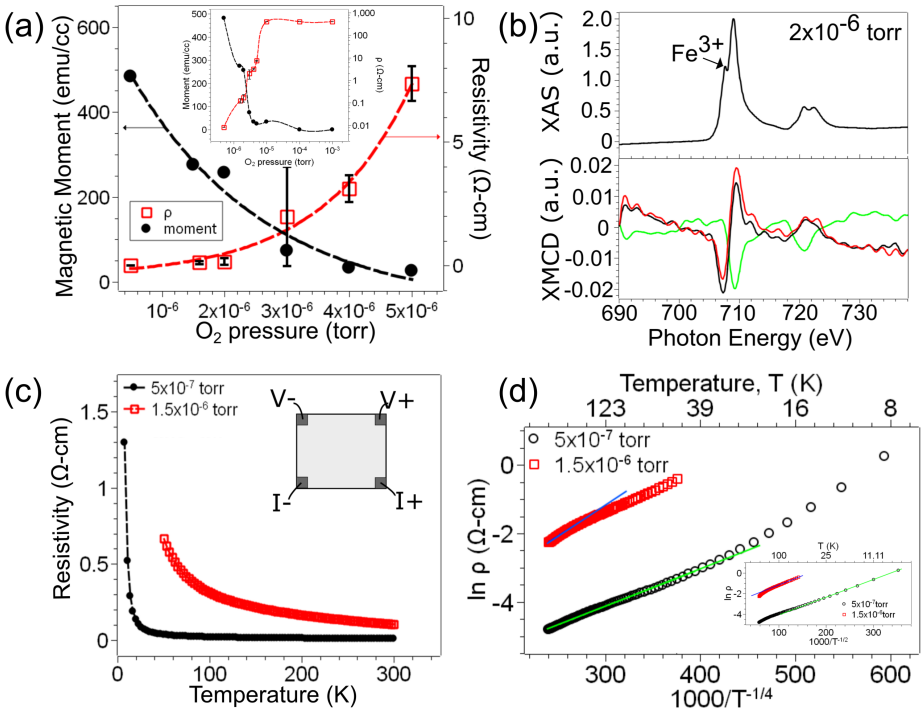


Figure 6.5: *(a) Plot of magnetic moment (black filled circles, left y-axis) and resistivity (red open squares, right y-axis) of FDTO thin films on quartz as a function of O_2 pressure; inset plots the same for wider pressure range showing that after 1x10^{-5} Torr the films become non-magnetic and insulating. (b) X-ray absorption spectroscopy (XAS, top plot) of FDTO showing split peak as evidence of Fe^{3+} , and XMCD (bottom plot) confirming Fe^{3+} (and not Fe^0)to be the source of magnetism (c) Resistivity vs temperature (from 8 K to 300 K) for FDTO films deposited at 5x10^{-7} Torr (black filled circles) and 1.5x10^{-5} Torr (red open squares) showing both films to be semiconducting; inset shows Van der Pauw configuration used for the measurement. (d) Plot of variable resistance hopping (VRH) fits to the data in (c), showing 3D-VRH conduction mechanism above ~100 K; inset shows fits to 1D-VRH conduction below 100 K.*

posited at 1.5x10^{-6} Torr. From this data, it could be concluded that since the films deposited at two lowest O_2 pressures exhibited semiconducting behavior, the more oxidized states deposited at higher O_2 pressures must also be semiconducting. The conduction mechanism in many disordered systems can be explained by either variable range hopping (VRH) or small polaron hopping (SPH) [54, 137, 138]. However, since the conductivity values observed in the FDTO system is much higher than those typically observed for systems with SPH conduction, VRH seemed the appropriate model to fit the resistivity data to. In 3-D VRH, the DC conductivity, σ, is related to the temperature by the following equation [54]:

$$\sigma_{DC} = \sigma_0 \exp[(-T_0/T)^{1/4}] \tag{6.3}$$

where

$$\sigma_0 = e^2 \nu_{ph} [N(E_F) a / 32\pi kT]^{1/2} \tag{6.4}$$

where e is the charge on an electron, $\nu_{ph}$is the phonon frequency, $N(E_F)$is the density of states (DOS) at the

Fermi level, a is the inverse of the tunneling probability, and k is the Boltzmann constant. However, it is also stated that a more generalized form of Eq. 6.3 is

$$\sigma_{DC} = \sigma_0' \exp[(-T_0/T)^{\gamma}] \tag{6.5}$$

where γ is $\frac{1}{d+1}$, with d being the space dimension of the system [54, 137] and 1/4<γ<1.0. The value of γ is largely determined by the localized DOS near the Fermi level, as explained by Singh and Shimakawa in their book [54]. In case of a constant DOS, $\gamma = 1/2$ is obtained; however, the value of γ can be less than unity in the case of modified VRH if the fractal nature of the system is taken into account [54, 139]. Therefore selecting the correct model to apply is not trivial. In the case of FDTO, the most typical fit of 3-D VRH was applied to the low temperature resistance data for both the films. As Fig. 6.5(d) shows, the experimental data fit very well with 3-D VRH (with $T^{-1/4}$) down to 100 K, below which a 1-D VRH ($T^{-1/2}$) fit the experimental data best. The transition from 3D-VRH to 1D-VRH could be a result of coulomb interactions playing a greater role at low temperature where the kinetic energy of the electrons are also low.

6.3.3 Optical properties and bandgap

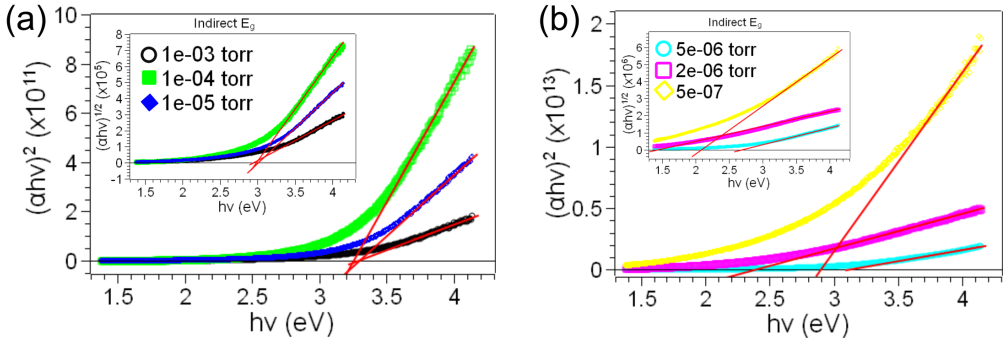


Figure 6.6: *(a), (b) Tauc plot for direct bandgap for FDTO films deposited at (a) 1x10^{-3} Torr (black open circle), 1x10^{-4} Torr (green filled square), and 1x10^{-5} Torr (blue filled diamond), and (b) 5x10^{-6} Torr (cyan open circle), 2x10^{-6} Torr (magenta open square), and 5x10^{-5} Torr (yellow open diamond). Inset for both plots show the Tauc plot for indirect bandgap. Red lines represent the fits to the linear region of the plots, and the x-intercept of the red line determine the band gap value.*

Finally optical transmission measurements were performed on all the FDTO films to calculate their bandgap. Fig. 6.7(a) shows the optical transmission increasing for the FDTO films deposited at higher O_2 pressures. Tauc plots for both direct and indirect bandgaps were created from the transmission data, as shown in Fig. 6.6(a) and (b). From the x-intercept of the fits to the linear region of the Tauc plots, the bandgap value can be determined. The direct and indirect bandgap values are plotted as a function of O_2 pressure in Fig. 6.7(b), where both the bandgaps are seen to increase till 1x10^{-6} Torr and then stabilize around that value for the higher O_2 pressures. The direct bandgap values were seen to start around 2.5 eV for the low pressure samples and increase up to around 3.3 eV for the higher pressure samples. Given that the bandgap value of Fe_2O_3, FeO, Tb_2O_3, and Dy_2O_3 are 2.2 eV[79, 80], 3.5 eV [140], 3.8 eV [86], and 4.9 eV [86], it can be concluded that the lanthanide oxides play an important role in determining the bandgap

of the films as well. However, the work function of two FDTO films, one deposited at $5x10^{-6}$ Torr and another at $1x10^{-6}$ Torr, were the same value of 4.4 eV, as shown in Fig.6.7(c). In contrast, their valence band maximum (VBM) edges were at different positions as shown in Fig.6.7(d). The Fermi level was found to lie 0.25 eV inside the valence band for the lower pressure film, while it was 0.34 eV above the valence band for the higher pressure film. This not only confirmed that both films were p-type semiconductors, but that at lower pressures, there was evidence for degenerate states. This could be the reason for the flatter shapes of the transmission curves observed in Fig. 6.7(a) for the lower pressure films when compared to the higher pressure films.

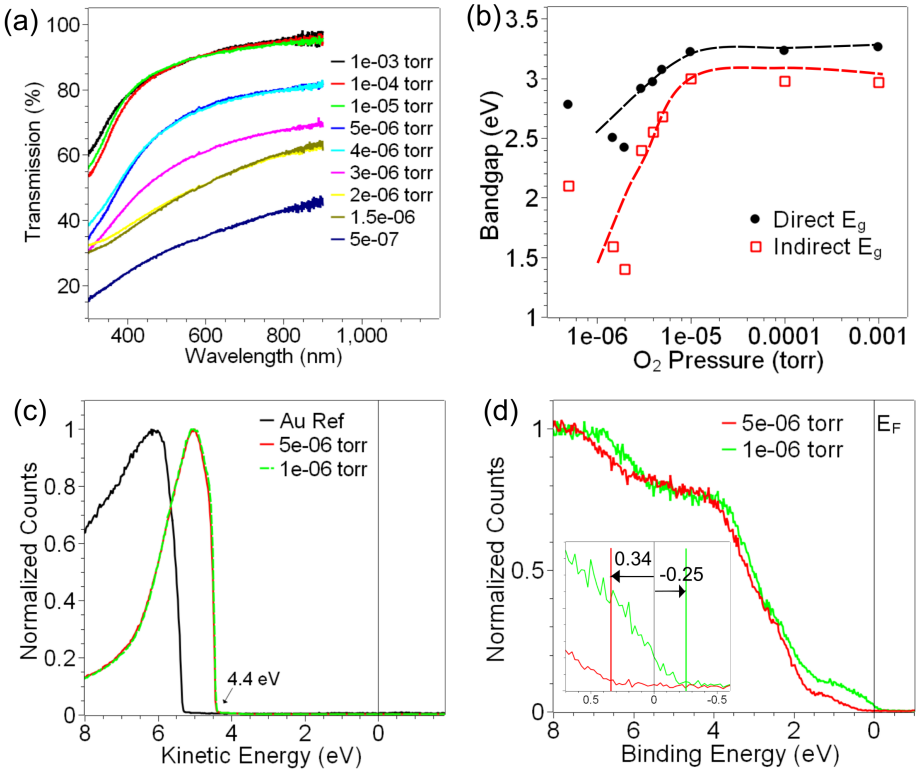


Figure 6.7: *(a)Plot of optical transmission (%) for all FDTO films deposited at different O_2 pressures, showing decrease in % transmission as O_2 pressure decreases. (b) Plot of direct (black filled circles) and indirect bandgap (red open squares) obtained from Tauc plots as a function of O_2 pressure; both bandgaps increase upto $1x10^{-5}$ Torr, after which they stay consistent. The dotted lines are simply guide for the eyes (c) Plot showing work function of FDTO films deposited at $5x10^{-6}$ Torr (red line) and at $1x10^{-6}$ Torr (green line); both films have the same work function of about 4.4 eV. (d) Valence band maximum edge obtained through XPS measurement of FDTO films deposited at $5x10^{-6}$ Torr (red line) and at $1x10^{-6}$ Torr (black line). The Fermi level is inside the valence band for the $1x10^{-6}$ Torr film, indicating degenerate states, while for the $5x10^{-6}$ Torr, it is 0.34 eV higher than the valence band edge. This indicates the films to be p-type semiconductors.*

6.4 Discussion and conclusion

Oxygen incorporation is a well-known technique for controlling transport properties of semiconductors since oxygen vacancies are very common. In chapter 5 of this thesis, it was seen that the way in which oxygen is introduced to a system can also significantly alter the properties of the final film. From the results of this chapter, the effect of introducing oxygen during film growth on the final transport properties of the films allowed better understanding of the FDTO films in general. The chemical composition analysis from TEM and XPS revealed the films to be of the form Me_2O_{3-x-y}, where Me = $Fe_{0.66}Dy_{0.24}Tb_{0.1}$, x=$Fe^{2+}/(Fe^{2+}+Fe^{3+})$ and y=$Tb^{3+}/(Tb^{3+}+Tb^{4+})$, indicating that this is an oxygen deficient system. Not only was it verified that the films are magnetic and conductive at room temperature, but the origin of magnetism was also identified as the Fe cation state instead of metallic Fe. Several studies have been done by the dilute magnetic semiconductor (DMS) community to synthesize materials that are conducting and magnetic at room temperature [68]. To achieve this, typical semiconductors such as GaAs are doped with magnetic atoms such as Mn. Over the course of years, although the Curie temperature of these materials have increased, it has still not reached room temperature [33, 68]. The ones that have been reported to show room temperature magnetism were found to have clusters of magnetic atoms inhomogeneously distributed across the film [68]. In addition, magnetic oxides have been synthesized by doping transparent conducting oxides with magnetic cations [33, 35]. Although the Curie temperature in these systems have been observed to be above 300 K, these materials have not demonstrated any correlation between the charge carriers and the ones carrying magnetic moment [33]. FDTO films are the first conducting oxides that are also magnetic at room temperature, and that have displayed correlation between the charge carriers and the origin of magnetism (such as through XMCD and MR data). The magnetism in this system could possibly be arising from the ratio of Fe^{2+}/Fe^{3+}, and also from some exchange coupling originating from the lanthanide oxides. Tb^{3+} ion is known to carry a large magnetic moment [89, 141], and in a study where the multiferroic material bismuth ferrite (BFO) was doped with Tb^{3+} [89], enhanced magnetic properties were observed in the doped films. The same was observed for terbium doped ferrite films [141]. Therefore the Tb ions could play a crucial role in the magnetic properties of the FDTO films. The conductivity in the films might be more dependent on the Fe cations since the Tb doped ferrite films [89, 141] have conductivity much lower than that observed in the FDTO films. In addition, the most promising films displaying magnetic and semiconducting behaviors are crystalline [33, 68]. In that regard, FDTO appears to be an exceptional and new material system that is amorphous, semiconducting, and magnetic at room temperature.

The most important finding from this chapter from an application perspective is the ability to control deposition parameters in order to obtain films with a combination of high conductivity and magnetism necessary for spintronic devices. The next chapter utilizes this understanding to optimize FDTO film growth to apply it towards magneto-electric coupling with BFO for memory devices.

6.5 Acknowledgments

This work was primarily supported by ARO grant W911NF-13-1-0428 and stipend from University of California-Berkeley for seven months. H.T. acknowledges the groups of Dr. Ramamoorthy Ramesh and

Dr. Lane Martin at University of California-Berkeley for use of PLD deposition facilities; and for XMCD, XAS, magnetic hysteresis and magneto-transport measurements. H. T. also acknowledges Dr. Tamil Sakthivel and Dr. Sudipta Seal at University of Central Florida for XPS measurements and analysis, Mark Hettick at University of California-Berkeley for work function and VBM measurement, Dr. Gerd Duscher and Chenze Liu at University of Tennessee-Knoxville for TEM and EELS measurements, and Dr. Rupam Mukherjee at University of Tennessee-Knoxville for help with magnetic hysteresis measurements. H. T. acknowledges Dr. David Geohagen at CNMS for use of their STEM instrument.

Chapter 7

Magneto-electric coupling of FDTO/BFO heterostructures for memory device applications

7.1 Summary

This chapter shows evidence of magneto-electric coupling between FDTO and bismuth ferrite ($BiFeO_3$; BFO) films. Thin films of FDTO grown by PLD on top of BFO/SRO/STO substrates at room temperature and in the presence of a magnetic field showed magnetic coupling with the underlying BFO by showing enhanced coercivity in the magnetic hysteresis loop. Ferroelectric hysteresis and fatigue measurements of FDTO/BFO capacitors proved FDTO to be a robust top electrode for BFO, showing less than 50% loss in polarization after 10^8 switching cycles. Giant-magnetoresistance (GMR) heterostructures fabricated on the FDTO/BFO films showed electric-field modulation of GMR at room temperature, making FDTO the first amorphous oxide that showed evidence of room-temperature ME coupling in addition to being a robust top electrode for BFO.

7.2 Methods

The first step was to select deposition parameters for FDTO and optimize its growth on BFO for repeatable evidence of magnetic coupling between the two layers. From the results of chapter 6, it was found that FDTO films grown between $3x10^{-6}$ Torr and $5x10^{-7}$ Torr exhibit low resistivity and high magnetic moment at room temperature. For the device studies, $3x10^{-6}$ Torr was selected as the preferred deposition pressure due to its practical combination of synthesis time and properties. The initial FDTO films showed no sign of coupling with BFO, and so the idea of using a magnetic field during the FDTO growth on BFO was introduced. This was practically feasible since FDTO deposition was done at room temperature and hence a permanent magnet would not be demagnetized. BFO/SRO/STO and quartz substrates were first cleaned in acetone and IPA and dried using a nitrogen gun. They were then mounted, using double sided tape,

on top of a small permanent magnet, which was mounted on the substrate holder also using double sided tape. The Terfenol-D target was then polished using sandpaper to remove any ablation marks from previous depositions, and then mounted on the target carousel that has the ability to rotate. The rest of the deposition was carried out according to the process described in chapter 6. Because the magnetic coupling happens at the FDTO/BFO interface, very thin films of FDTO were deposited (~3 to 10 nm).

The FDTO/BFO/SRO/STO (which will be referred to as FDTO/BFO from this point onwards) and FDTO/quartz samples were first characterized by SQUID to check for enhanced coercivity of FDTO on the BFO as compared to on quartz. Once that was accomplished, the capacitors were fabricated on the FDTO/BFO samples according to the process described in chapter 2. On a second piece of FDTO/BFO sample that showed magnetic coupling in SQUID, GMR device structures were fabricated according to the process described in chapter 2.

7.3 Results

7.3.1 Evidence of magnetic coupling

The very first measurement needed to determine whether the FDTO/BFO sample is worth pursuing further is the magnetic hysteresis loop that demonstrates magnetic coupling by showing higher coercivity for films on BFO than on any other regular substrate. For FDTO, coercive field was compared between FDTO grown on BFO and on quartz. Fig. 7.1(a) shows evidence of magnetic coupling between 4.6 nm FDTO and 50 nm BFO, where the inset highlights that the coercive field of FDTO on BFO was about 380 Oe while that on quartz was only about 20 Oe.

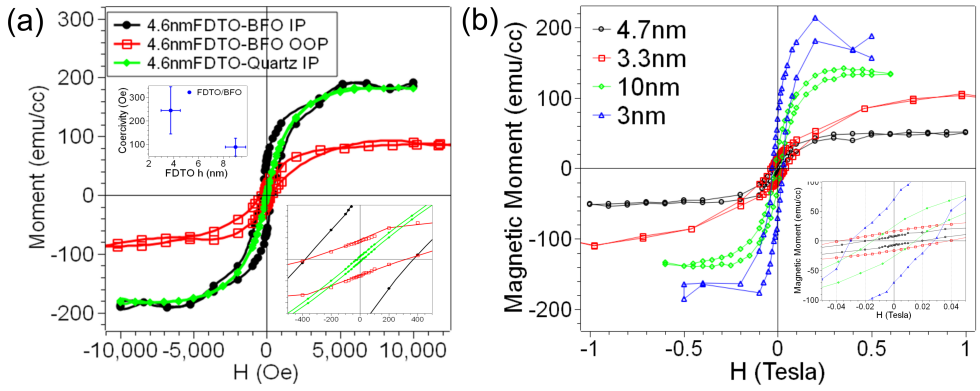
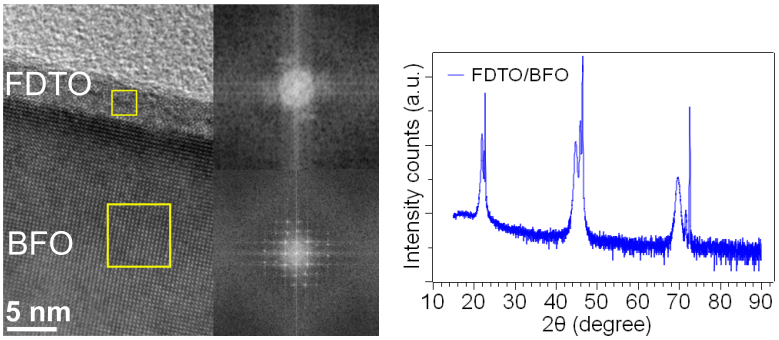


Figure 7.1: *(a) Room temperature magnetic hysteresis of 4.6 nm FDTO on BFO (black, filled circles-IP, and red, open squares - OOP) and on quartz (green filled triangles). Bottom-right inset shows enhancement of coercive field of FDTO on BFO than on quartz, indicating magnetic coupling between FDTO and BFO. Top left inset shows coercivity drops as FDTO thickness is increased, confirming exchange interaction between FDTO and BFO. (b) Magnetic hysteresis loops taken at room temperature with IP magnetic field for FDTO films on BFO for different thicknesses. Inset shows coercive field enhancement for all films, but higher coercivity for films between 3 - 4.7 nm than for that at 10 nm.*

This result was repeatable as can be seen in Fig. 7.1(b) inset from the high coercive fields obtained for

three other FDTO films in the thickness range of 3 to 4.7nm on BFO. It can be also seen from the inset in Fig. 7.1(b) that while coercivity of 10 nm FDTO on BFO was still higher than what is typically seen on quartz (~20-40 Oe), it was still lower than the coercive fields obtained for the thinner FDTO films. This finding is summarized in the top left inset of Fig. 7.1(a). This was evidence of exchange interaction between FDTO and BFO, where the coercive field decreases with increasing thickness of the top ferromagnetic layer. Since exchange interaction is an interface phenomenon, it was important to check the FDTO/BFO interface in TEM, as well as to double check the crystalline phase of BFO in these samples by XRD. Fig. 7.2(a) shows the HRTEM image of the FDTO/BFO interface to be clean without any inter-mixing of the two layers. FFT images (on the right of the TEM image) taken from the regions marked in yellow boxes show the FDTO layer to be amorphous and the BFO layer to be crystalline. In addition, XRD pattern of the FDTO/BFO film shown in Fig. 7.2(b) shows correct crystalline phases of BFO in the film [142, 143]. This concluded that the FDTO layer was not deteriorating the microstructure of BFO by introducing any kind of strain.



(a) (b)

Figure 7.2: *(a)HRTEM image of as-prepared FDTO/BFO layers showing a clean interface; yellow boxes outline regions from where diffraction patterns were obtained, confirming amorphous and crystalline microstructures of FDTO (top) and BFO (bottom) respectively. (b) XRD signal from FDTO/BFO film showing clean peaks from BFO.*

7.3.2 Ferroelectric hysteresis and fatigue of FDTO/BFO capacitors

The next step was to ascertain that FDTO was not affecting the ferroelectric properties of the BFO film. To achieve this, ferroelectric hysteresis loops were measured on FDTO/BFO capacitors of diameter 16 μm, as shown in Fig. 7.3(a). The plot shows data taken from three different capacitors on the sample with bias voltage being applied in both directions. The hysteresis loops were observed to have shifted to the left, which is a typical phenomenon whenever the top and bottom electrodes are made of different materials: in this case the top electrode was FDTO and the bottom electrode was SRO. The schematic of the capacitor is shown as an inset in Fig. 7.3(b). Results of the ferroelectric fatigue measurement on the same capacitor is shown in Fig. 7.3(b) where the polarization drop in both the positive polarization and the negative polarization was found to be less than 50% up to 10^8cumulative switching cycles. The positive polarization value (red and black data points) can be seen to increase from the first cycle to the 10^5cycle - this can happen if the polarization is not saturated in that direction, which might be a valid case for this capacitor since the

ferroelectric loop was shifted towards the negative field.

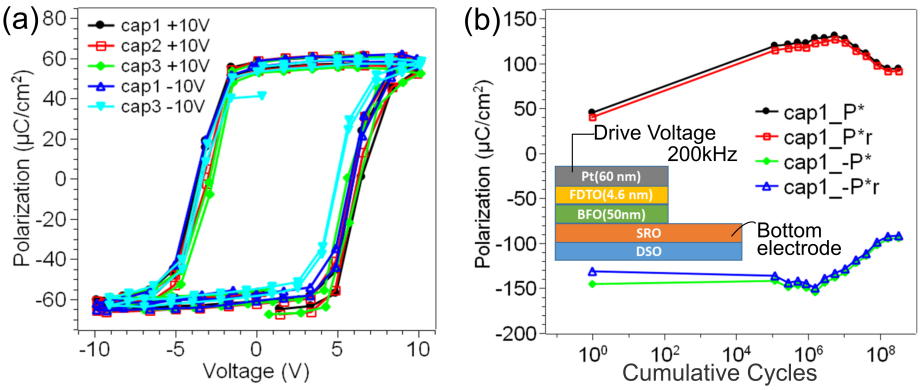


Figure 7.3: *(a) Ferroelectric hysteresis and (b) fatigue test obtained from FDTO/BFO capacitors (device schematic shown as inset of (c)) demonstrating FDTO is a stable ferromagnetic electrode for BFO.*

7.3.3 Magneto-electric (ME) coupling in GMR heterostructure

The final step of the study was to see evidence of magneto-electric coupling by means of creating GMR heterostructures. Magnetic hysteresis of a GMR stack typically shows a step in the loop corresponding coercivity of the more ferromagnetic layer with higher coercive field. Fig. 7.4(a) shows that in the hysteresis loop for the GMR structure (schematic shown in inset of Fig. 7.4(b)) on the FDTO/BFO layer, represented by blue open circles, the hysteresis widens or opens up starting around 300 Oe, while it gets very narrow at around 20 Oe. The widening around 300 Oe corresponds to the bottom CoFe layer that coupled to the FDTO/BFO layers. This correlated well with the magnetic hysteresis loop for the 3.3 nm film in Fig. 7.1(b), where the coercivity was around 380 Oe, since that was the sample on which the GMR structures were made. The pinching of the loop around 20 Oe corresponds to the top CoFe layer. Although the hysteresis loop for this GMR stack did not resemble sharp steps expected from traditional GMR devices [144], it is still reflective of the coupling of the bottom CoFe layer to the BFO layer through FDTO. Similar data was also seen in LSMO/SSMO stacks for spin filter tunnel junction devices (supplementary material from Prasad et al. [145]). Upon application of a bias electric field of +10 V in the positive direction, the GMR signal overlaps with that for no bias applied (red and black data points in Fig. 7.4(b)). This indicated that the BFO was already in the positive polarization in the as-prepared state. However, when a negative bias field of -8 V was applied, the %GMR signal was observed to change, as shown by the blue data points, the coercive field was seen to slightly increase along with the %GMR value. This was evidence of magneto-electric coupling at room temperature because the change in the bias voltage caused the polarization in BFO to switch, which in turn caused the spins in FDTO layer, and hence the bottom CoFe layer, to switch, leading to an increase in the coercive field because a higher field is necessary to switch back the spins that were affected by the BFO layer. Fig. 7.4(c) shows the HR-TEM image of the GMR structure after it underwent some switching voltages. From the diffraction patterns obtained from the areas marked in yellow boxes, it could be confirmed that the microstructure of the individual layers did not change, i.e., the CoFe layer

remained polycrystalline, the FDTO remained amorphous, and the BFO remained crystalline. However, some bismuth diffusion was observed from the BFO layer to the FDTO layer, marked by the red square. It was inconclusive whether this diffusion occurred during the anneal step at 90 ºC required for device fabrication, or if it was due to the application of bias voltage for multiple times.

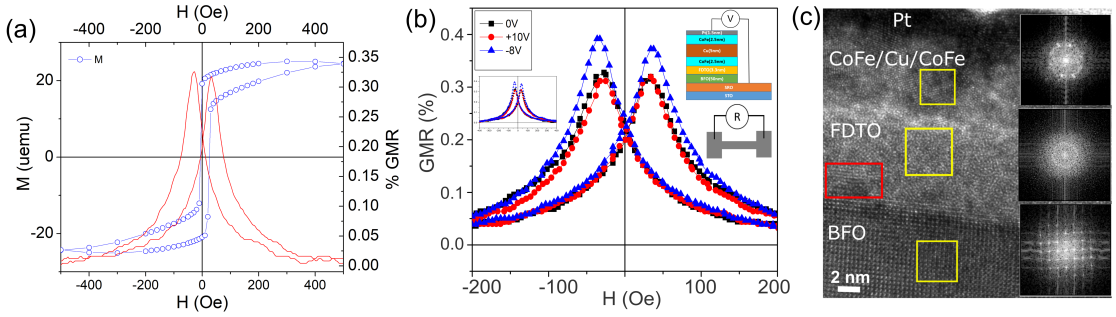


Figure 7.4: *(a) Plot showing magnetic hysteresis (left y-axis, blue open circles) and %GMR signal (right y-axis, red line) of the Pt/CoFe/Cu/CoFe/FDTO/BFO/SRO/STO GMR heterostructure, shown in the top-right inset of (b); bottom-right inset of (b) shows the top view of the device. The broadening of the hysteresis loop starting around 300 Oe is from the coercivity of the bottom CoFe layer coupled to the FDTO/BFO, while the narrowing of the loop around 20 Oe is from the coercivity of the top CoFe layer. This overlaps with the %GMR signal where the resistance starts to increase at around 300 Oe and reaches a maximum at around 20 Oe before dropping rapidly. (b) Plot of the %GMR signal of the heterostructure upon application of bias 0 V (black filled square), +10 V (red filled circle), and -8 V (blue filled triangle).The coercivity of the GMR signal is seen to increase with the application of the negative electric field bias, indicating that the polarization switch in BFO caused the coercive field of FDTO to increase, which was seen in the GMR signal. (c) HRTEM image of the cross-section of the GMR heterostructure. The diffraction patterns on the right panels are taken from the regions marked with yellow boxes. The red box shows bismuth atoms diffusing into the FDTO layer.*

7.4 Discussion and conclusion

Magneto-electric coupling is a much sought-after phenomenon for the purpose of making spintronic devices. Although some studies have showed evidence of room temperature ME coupling between bilayers [146, 147], they have not reported a functional device. Room temperature ME coupling, with the demonstration of a working GMR device, of CoFe with BFO has been reported in a study [101] where the anisotropic magnetoresistance signal from the CoFe/BFO layers was seen to completely switch upon the application of a bias voltage. However, the interface of CoFe and BFO was not proved to be very robust as the study reported the device performance degrading after only about 3 switching cycles. In contrast, FDTO is a much more robust electrode on BFO, sustaining ferroelectric switching of BFO till about 10^8 switching cycles. An equally appealing aspect of FDTO is its amorphous microstructure that allows for very easy growth by PLD without having the need for substrate heating at high temperature. Very low %GMR was observed for this system, which could be explained using the following hypothesis. GMR signal is a result of the opposite spin directions of the bottom ferromagnetic layer and the top ferromagnetic layer. In this case, the bottom

ferromagnetic layer is CoFe coupled to FDTO which, in turn, is coupled to BFO. It typically takes upto 1 Tesla or higher for FDTO magnetization to saturate in MH loops (indicating that all spins are aligned). This is evident in the MH loops for the GMR device as well. It might be possible that all the spins in FDTO are not completely being flipped in the GMR measurement, and while that causes the resistance to change, it is relatively small compared to when all the spins are flipped. Regardless, there is evidence of ME coupling in the device. Through this room temperature ME coupling, FDTO has proved to be a very attractive material with huge potential for application in spintronic devices.

7.5 Acknowledgments

This work was primarily supported by ARO grant W911NF-13-1-0428 and stipend from University of California-Berkeley for seven months. H.T. acknowledges the groups of Dr. Ramamoorthy Ramesh and Dr. Lane Martin at University of California-Berkeley for help with all film deposition, device fabrication, and measurements presented in this chapter. H.T. also acknowledges Dr. Bhagwati Prasad as an equal contributor to the results presented in this chapter.

Chapter 8

Conclusions and future work

In this chapter we summarize the key findings of this thesis and will discuss potential future applications of FDTO.

8.1 Conclusions

- *Chapter 3*: We have summarized discovery of novel amorphous oxide system, $(Fe_{0.66}Dy_{0.24}Tb_{0.1})_2O_{3-x}$ (FDTO) by depositing thin films of the material by PLD using the Terfenol-D metal alloy target. The resulting films were transparent, with the highest transparency reaching >90% for a 9 nm film. In addition, the films exhibited the combination of high conductivity and high mobility, far exceeding that of any of the constituent oxides. This discovery, summarized in Fig. 8.1, could lead to understanding of new materials physics and the option to design and synthesize new materials with desirable multifunctional properties.

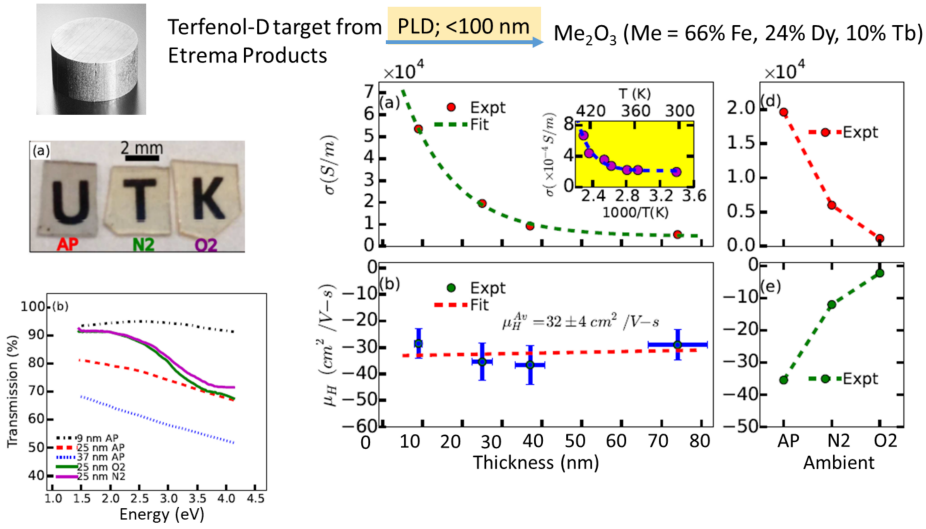


Figure 8.1: *Figure showing extraordinary optical and electrical properties of FDTO*

- *Chapter 4*: We have described the effects of changing cation stoichiometry on the properties of FDTO

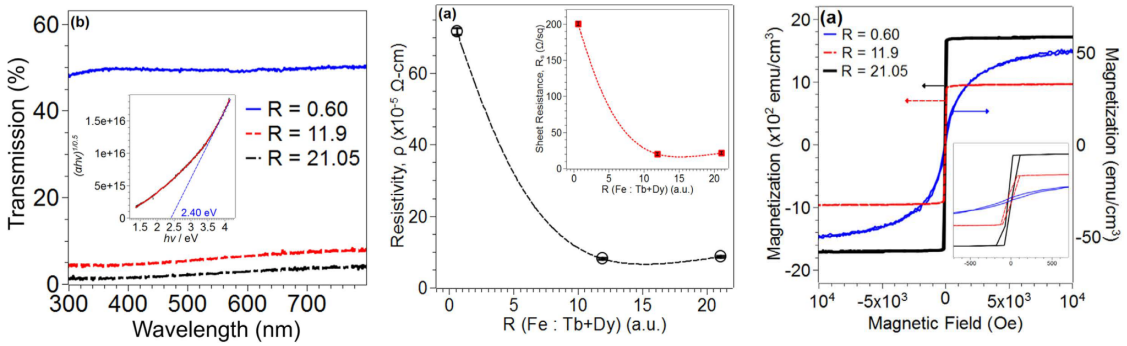


Figure 8.2: *Figure showing high conductivity and magnetism in FDTO films of different cation stoichiometry*

by synthesizing and characterizing films of three different Fe:(Tb+Dy) ratios. The results showed a transition from metallic to semiconductor behavior in the as-prepared films going up in Fe amount. All the films demonstrated high conductivity and magnetism showing in Fig. 8.2 , the two properties desirable for spintronic applications.

- *Chapter 5*: We have investigated the effects of cyclic annealing on the properties of an iron rich FDTO film with Fe:(Tb+Dy) of 21. With each annealing cycle the film got more an more oxidized, similar to the case of a semiconductor whose doping is being changed. The final oxide state was stable in ambient conditions, had high conductivity and magnetism, although the microstructure showed some phase segregation and a mix of amorphous and polycrystalline regions. The results are shown in Fig. 8.3. This could help design annealing processing steps in order to modify the transport and magnetic properties of materials.

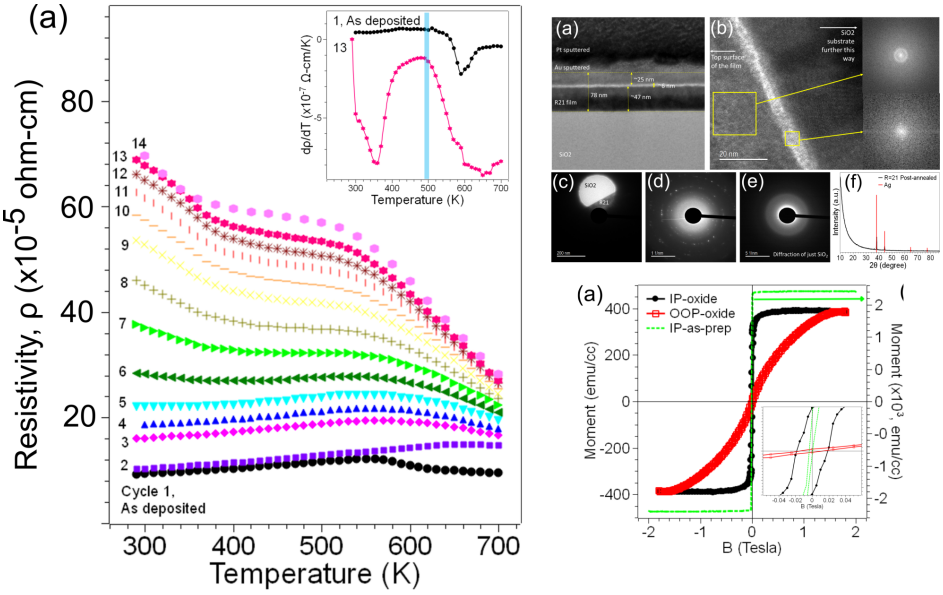


Figure 8.3: *Figure showing the effect of cyclic anneal on the resistivity, microstructure, and magnetic property of iron-rich FDTO film.*

- *Chapter* 6: We have described the effects of changing oxygen content in thin films of FDTO deposited by PLD. Given how excess oxygen can create acceptor states and oxygen vacancies can create donor states in the band structure, the changing oxygen pressure gave insights into the origin of magnetism and conduction. The films were all amorphous, and p-type according to valence band maximum analysis. We found that reducing oxygen pressure decreased the band-gap and resistivity of the films, while the magnetic moment increased, as shown in Fig. 8.4. The conduction, therefore could be happening by increasing number of donor states from oxygen vacancy that gives a very high carrier density near the VB. The source of magnetism could either be the Fe^{2+} cation, or Tb^{3+} cation since both are used as dopants to introduce /enhance magnetism in non-magnetic films. Regardless, the findings from this study could help control deposition parameters for FDTO to obtain films having application-targeted properties.

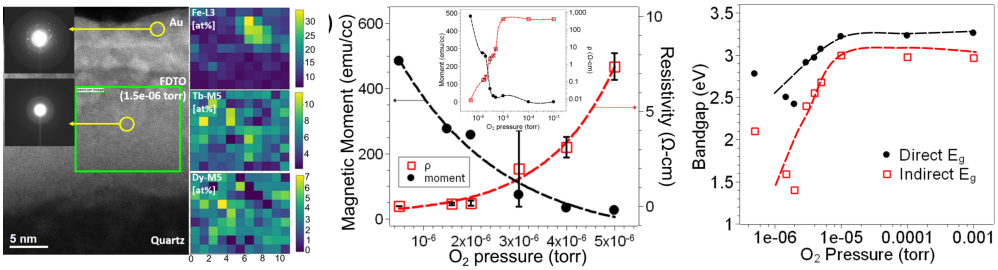


Figure 8.4: *Figure showing microstructure and chemical composition, resistivity and magnetism, and bandgap (from left to right respectively) of FDTO films deposited as a function of O_2 pressure.*

- *Chapter* 7: We optimized the deposition of FDTO on BFO to obtain repeated magnetic coupling in the two films. Capacitor devices from FDTO/BFO samples showed FDTO as a robust top electrode for BFO. A GMR device was fabricated to look for evidence of ME coupling, and upon electric-field application, the GMR signal was seen to change, indicating ME coupling at room temperature. The results are summarized in Fig. 8.5. This is the first observation of ME coupling at room temperature using an amorphous ferromagnet. Further optimization of this system could lead to practical applications in memory devices.

8.2 Future work

Since FDTO is such a promising system for applications in the spintronics industry, some more work is necessary to fully understand this amorphous system and optimize deposition parameters for applications in devices. Some of the key studies for the future are listed below:

- X-ray fine absorption spectroscopy to look at the atomic arrangement in FDTO. This information, coupled with pair distribution function analysis of TEM diffraction pattern, could help identify the presence (if any) of short range order in the system.

- Studying the properties of ternary systems with varying metal composition as well as the binary

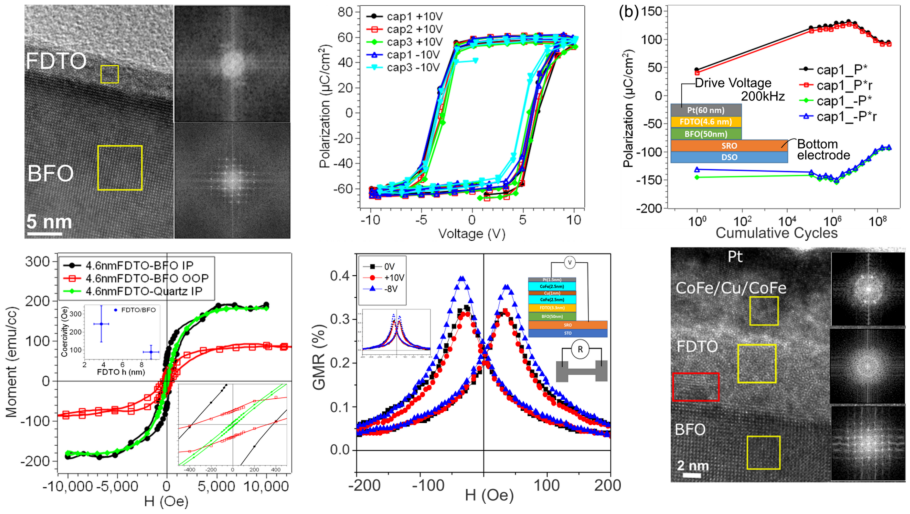


Figure 8.5: *From top-left corner in clockwise direction: TEM image of clean FDTO/BFO interface, good ferroelectric hysteresis, and robust fatigue test for FDTO/BFO capacitors. TEM image of GMR device structure, room temperature ME coupling in GMR device, magnetic hysteresis showing magnetic coupling between FDTO/BFO films.*

systems, such as FeTb or FeDy to gain better understanding of the interaction of the iron cations with the lanthanides.

- PLD growth of films with different cation stoichiometry, especially iron-rich ones, could produce films that are even better for ME coupling.
- Finding the Curie temperature of FDTO via Mossbauer spectroscopy.

Bibliography

[1] A. Malasi, H. Taz, A. Farah, M. Patel, B. Lawrie, R. Pooser, A. Baddorf, G. Duscher, and R. Kalyanaraman, "Novel iron-based ternary amorphous oxide semiconductor with very high transparency, electronic conductivity, and mobility.," *Scientific reports*, vol. 5, pp. 18157–18157, 2015.

[2] M. Hasegawa, H. Yanagihara, Y. Toyoda, E. Kita, and L. Ranno, "Electrical and magnetic properties of -fe2o3 epitaxial films," *Journal of Magnetism and Magnetic Materials*, vol. 310, pp. 2283–2285, Mar. 2007.

[3] H. Yanagihara, M. Hasegawa, E. Kita, Y. Wakabayashi, H. Sawa, and K. Siratori, "Iron vacancy ordered γ-fe2o3(001) epitaxial films: The crystal structure and electrical resistivity," *Journal of the Physical Society of Japan*, vol. 75, May 2006.

[4] J. Engel and H. L. Tuller, "The electrical conductivity of thin film donor doped hematite: from insulator to semiconductor by defect modulation," *Phys. Chem. Chem. Phys.*, vol. 16, pp. 11374–11380, 2014.

[5] P. Liao, M. C. Toroker, and E. A. Carter, "Electron transport in pure and doped hematite," *Nano Lett.*, vol. 11, pp. 1775–1781, 2011.

[6] B. Zhao, T. C. Kaspar, T. C. Droubay, J. McCloy, M. E. Bowden, V. Shutthanandan, S. M. Heald, and S. A. Chambers, "Electrical transport properties of Ti-doped Fe_2O_3(0001) epitaxial films," *Phys. Rev. B*, vol. 84, p. 245325, 2011.

[7] X. W. Li, A. Gupta, G. Xiao, and G. Q. Gong, "Transport and magnetic properties of epitaxial and polycrystalline magnetite thin films," *Journal of Applied Physics*, vol. 83, pp. 7049–7051, June 1998.

[8] R. Prakash, R. J. Choudhary, L. S. S. Chandra, N. Lakshmi, and D. M. Phase, "Electrical and magnetic transport properties of fe 3 o 4 thin films on a gaas(100) substrate," *Journal of Physics: Condensed Matter*, vol. 19, no. 48, p. 486212, 2007.

[9] N. W. Gray, M. C. Prestgard, and A. Tiwari, "Tb2o3 thin films: An alternative candidate for high-k dielectric applications," *Applied Physics Letters*, vol. 105, no. 22, 2014.

[10] D. Basler, *High Temperature Oxidation of Gadolinium and Dysprosium under Controlled Oxygen Partial Pressure*. PhD thesis, Jan 1972.

[11] J. Robertson and B. Falabretti, *Electronic Structure of Transparent Conducting Oxides*. 2010.

[12] J. Robertson, R. Gillen, and S. J. Clark, "Advances in understanding of transparent conducting oxides," *Thin Solid Films*, vol. 520, no. 10, pp. 3714–3720, 2012.

[13] T. Kamiya and H. Hosono, "Material characteristics and applications of transparent amorphous oxide semiconductors," *NPG Asia Mater.*, vol. 2, pp. 15–22, 2010.

[14] H. Hosono, N. Kikuchi, N. Ueda, and H. Kawazoe, "Working hypothesis to explore novel wide band gap electrically conducting amorphous oxides and examples," *J. Non-Crys. Solids*, vol. 198-200, pp. 165–169, 1996. Proceedings of the Sixteenth International Conference on Amorphous Semiconductors - Science and Technology.

[15] H. Hosono, J. Kim, Y. Toda, T. Kamiya, and S. Watanabe, "Transparent amorphous oxide semiconductors for organic electronics: Application to inverted oleds," *Proceedings of the National Academy of Sciences*, vol. 114, no. 2, pp. 233–238, 2017.

[16] K. Nomura, T. Kamiya, H. Ohta, T. Uruga, M. Hirano, and H. Hosono, "Local coordination structure and electronic structure of the large electron mobility amorphous oxide semiconductor in-ga-zn-o: Experiment and ab initio calculations," *Physical Review B*, vol. 75, no. 3, 2007.

[17] H. Taz, T. Sakthivel, N. Yamoah, C. Carr, D. Kumar, S. Seal, and R. Kalyanaraman, "Transparent ferromagnetic and semiconducting behavior in fe-dy-tb based amorphous oxide films," *Scientific reports*, vol. 6, 2016.

[18] K. Ellmer, "Past achievements and future challenges in the development of optically transparent electrodes," *Nature Photonics*, vol. 6, no. 12, pp. 808–816, 2012.

[19] S. K. Park, J. I. Han, W. K. Kim, and M. G. Kwak, "Deposition of indium-tin-oxide films on polymer substrates for application in plastic-based flat panel displays," *Thin Solid Films*, vol. 397, no. 1-2, pp. 49 – 55, 2001.

[20] K. Nomura, H. Ohta, A. Takagi, T. Kamiya, M. Hirano, and H. Hosono, "Room-temperature fabrication of transparent flexible thin-film transistors using amorphous oxide semiconductors," *Nature*, vol. 432, pp. 488–492, 2004.

[21] A. Haghiri-Gosnet, T. Arnal, R. Soulimane, M. Koubaa, and J. Renard, "Spintronics: perspectives for the half-metallic oxides," *physica status solidi (a)*, vol. 201, no. 7, pp. 1392–1397, 2004.

[22] S. J. Pearton, D. P. Norton, R. Frazier, S. Y. Han, C. R. Abernathy, and J. M. Zavada, "Spintronics device concepts," *IEE Proceedings - Circuits, Devices and Systems*, vol. 152, pp. 312–322, Aug 2005.

[23] S. A. Wolf, D. D. Awschalom, R. A. Buhrman, J. M. Daughton, S. von Molnár, M. L. Roukes, A. Y. Chtchelkanova, and D. M. Treger, "Spintronics: A spin-based electronics vision for the future," *Science*, vol. 294, no. 5546, pp. 1488–1495, 2001.

[24] K. Dagenais, M. Chamberlain, and C. Constantin, "Energy band gap behavior as a function of optical electronegativity for semiconducting and insulating binary oxides." Powerpoint presentation.

[25] Z. A. Weinberg, G. W. Rubloff, and E. Bassous, "Transmission, photoconductivity, and the experimental band gap of thermally grown sio$_2$ films," *Phys. Rev. B*, vol. 19, pp. 3107–3117, Mar 1979.

[26] G. LincotD., Hodes, ed., *Chemical Solution Deposition of Semiconducting and Non-Metallic Films: Proceedings of the International Symposium*. The Electrochemical Society, 2006.

[27] M. V. Srinivasan, M. Ito, P. Kumar, K. Abhirami, N. Tsuda, J. Yamada, P.-K. Shin, and S. Ochiai, "Performance evaluation of an organic thin-film solar cell of ptb7:pc71bm with an alcohol-soluble polyelectrolyte interlayer prepared using the spray-coating method," *Industrial & Engineering Chemistry Research*, vol. 54, no. 1, pp. 181–187, 2015.

[28] V. Teixeira, H. Cui, L. Meng, E. Fortunato, and R. Martins, "Amorphous ito thin films prepared by dc sputtering for electrochromic applications," *Thin Solid Films*, vol. 420-421, pp. 70 – 75, 2002. Proceedings of the 29th International Conference on Metallurgic Coatings and Thin Films.

[29] H. Yumoto, T. Inoue, S. Li, T. Sako, and K. Nishiyama, "Application of {ITO} films to photocatalysis," *Thin Solid Films*, vol. 345, no. 1, pp. 38 – 41, 1999.

[30] E. K.-H. Yu, S. Jun, D. H. Kim, and J. Kanicki, "Density of states of amorphous in-ga-zn-o from electrical and optical characterization," *Journal of Applied Physics*, vol. 116, October 2014.

[31] J. S. Y. Feng, R. D. Pashleyz, and M. A. Nicolet, "Magnetoelectric properties of magnetite thin films," *J. Phys. C: Solid State Phys.*, vol. 8, pp. 1010–1022, 1975.

[32] G. Q. Gong, A. Gupta, G. Xiao, W. Qian, and V. P. Dravid, "Magnetoresistance and magnetic properties of epitaxial magnetite thin films," *Phys. Rev. B*, vol. 56, pp. 5096–5099, Sep 1997.

[33] J. Coey, "Dilute magnetic oxides," *Current Opinion in Solid State and Materials Science*, vol. 10, no. 2, pp. 83 – 92, 2006.

[34] T. Dietl, H. Ohno, F. Matsukura, J. Cibert, and D. Ferrand, "Zener model description of ferromagnetism in zinc-blende magnetic semiconductors," *Science*, vol. 287, no. 5455, pp. 1019–1022, 2000.

[35] S. J. Pearton, W. H. Heo, M. Ivill, D. P. Norton, and T. Steiner, "Dilute magnetic semiconducting oxides," *Semiconductor Science and Technology*, vol. 19, no. 10, p. R59, 2004.

[36] J. D. Wei, I. Knittel, U. Hartmann, Y. Zhou, S. Murphy, I. V. Shvets, and F. T. Parker, "Influence of the antiphase domain distribution on the magnetic structure of magnetite thin films," *Applied Physics Letters*, vol. 89, no. 12, p. 122517, 2006.

[37] H.-K. Liao, J.-C. Chou, W.-Y. Chung, T.-P. Sun, and S.-K. Hsiung, "Study of amorphous tin oxide thin films for isfet applications," *Sensors and Actuators B: Chemical*, vol. 50, no. 2, pp. 104 – 109, 1998.

[38] E. Llobet, G. Molas, P. Molinàs, J. Calderer, X. Vilanova, J. Brezmes, J. E. Sueiras, and X. Correig, "Fabrication of highly selective tungsten oxide ammonia sensors," *Journal of The Electrochemical Society*, vol. 147, no. 2, pp. 776–779, 2000.

[39] C. W. Chu, M. J. Deen, and R. H. Hill, "Sensors for detecting sub-ppm no2 using photochemically produced amorphous tungsten oxide," *Journal of The Electrochemical Society*, vol. 145, no. 12, pp. 4219–4225, 1998.

[40] Y.-C. Chen, T.-C. Chang, H.-W. Li, W.-F. Chung, C.-P. Wu, S.-C. Chen, J. Lu, Y.-H. Chen, and Y.-H. Tai, "High-stability oxygen sensor based on amorphous zinc tin oxide thin film transistor," *Applied Physics Letters*, vol. 100, no. 26, 2012.

[41] H. Zhao, H. Tu, F. Wei, Z. Shi, Y. Xiong, Y. Zhang, and J. Du, "High mechanical endurance rram based on amorphous gadolinium oxide for flexible nonvolatile memory application," *Journal of Physics D: Applied Physics*, vol. 48, no. 20, p. 205104, 2015.

[42] J.-S. Huang, W.-C. Yen, S.-M. Lin, C.-Y. Lee, J. Wu, Z. M. Wang, T.-S. Chin, and Y.-L. Chueh, "Amorphous zinc-doped silicon oxide (szo) resistive switching memory: manipulated bias control from selector to memristor," *J. Mater. Chem. C*, vol. 2, pp. 4401–4405, 2014.

[43] X. Li, L. Zhang, H. Dong, T. Xia, and Z. Huang, "Bismuth oxide coated amorphous manganese dioxide for electrochemical capacitors," *Solid State Sciences*, vol. 43, pp. 46 – 52, 2015.

[44] D. Yang, "Pulsed laser deposition of vanadium-doped manganese oxide thin films for supercapacitor applications," *Journal of Power Sources*, vol. 228, pp. 89 – 96, 2013.

[45] J. F. Wager, B. Yeh, R. L. Hoffman, and D. A. Keszler, "An amorphous oxide semiconductor thin-film transistor route to oxide electronics," *Current Opinion in Solid State and Materials Science*, vol. 18, no. 2, pp. 53 – 61, 2014.

[46] F. Pincella, K. Isozaki, and K. Miki, "A visible light-driven plasmonic photocatalyst," *Light Sci Appl*, vol. 3, p. e133, Jan. 2014.

[47] Z. Li, C. Kong, and G. Lu, "Visible photocatalytic water splitting and photocatalytic two-electron oxygen formation over cu- and fe-doped g-c3n4," *The Journal of Physical Chemistry C*, vol. 120, no. 1, pp. 56–63, 2016.

[48] M. Chiku, H. Takeda, S. Matsumura, E. Higuchi, and H. Inoue, "Amorphous vanadium oxide/carbon composite positive electrode for rechargeable aluminum battery," *ACS Applied Materials & Interfaces*, vol. 7, no. 44, pp. 24385–24389, 2015. PMID: 26489385.

[49] Y. Idota, T. Kubota, A. Matsufuji, Y. Maekawa, and T. Miyasaka, "Tin-based amorphous oxide: A high-capacity lithium-ion-storage material," *Science*, vol. 276, no. 5317, pp. 1395–1397, 1997.

[50] N. Zhou, D. B. Buchholz, G. Zhu, X. Yu, H. Lin, A. Facchetti, T. J. Marks, and R. P. H. Chang, "Ultraflexible polymer solar cells using amorphous zinc-indium-tin oxide transparent electrodes," *Advanced Materials*, vol. 26, no. 7, pp. 1098–1104, 2014.

[51] M. Liu, O. Obi, J. Lou, Y. Chen, Z. Cai, S. Stoute, M. Espanol, M. Lew, X. Situ, K. S. Ziemer, V. G. Harris, and N. X. Sun, "Giant electric field tuning of magnetic properties in multiferroic ferrite/ferroelectric heterostructures," *Advanced Functional Materials*, vol. 19, no. 11, pp. 1826–1831, 2009.

[52] R. Geng, H. M. Luong, T. T. Daugherty, L. Hornak, and T. D. Nguyen, "A review on organic spintronic materials and devices: Ii. magnetoresistance in organic spin valves and spin organic light emitting diodes," *Journal of Science: Advanced Materials and Devices*, vol. 1, no. 3, pp. 256 – 272, 2016.

[53] K. Shrestha, "Electrical conduction mechanisms in the disordered material system p-type hydrogenated amorphous silicon," 2014.

[54] J. Singh, "Advances in amorphous semiconductors," 2003.

[55] P. W. Anderson, "Absence of diffusion in certain random lattices," *Phys. Rev.*, vol. 109, pp. 1492–1505, Mar 1958.

[56] N. F. Mott, "Conduction in non-crystalline materials," *The Philosophical Magazine: A Journal of Theoretical Experimental and Applied Physics*, vol. 19, no. 160, pp. 835–852, 1969.

[57] N. F. Mott, "Conduction in non-crystalline systems," *The Philosophical Magazine: A Journal of Theoretical Experimental and Applied Physics*, vol. 22, no. 175, pp. 7–29, 1970.

[58] N. Mott and E. Davis, *Electronic process in non-crystalline materials*. Oxford University Press, 2nd ed., 1979.

[59] H. Hosono, "Ionic amorphous oxide semiconductors: Material design, carrier transport, and device application," *Journal of Non-Crystalline Solids*, vol. 352, no. 9-20, pp. 851 – 858, 2006. Amorphous and Nanocrystalline Semiconductors - Science and TechnologyProceedings of the 21st International Conference on Amorphous and Nanocrystalline Semiconductors - Science and Technology21st International Conference on Amorphous and Nanocrystalline Semiconductors.

[60] G. Hautier, A. Miglio, D. Waroquiers, G.-M. Rignanese, and X. Gonze, "How does chemistry influence electron effective mass in oxides? a high-throughput computational analysis," *Chemistry of Materials*, vol. 26, no. 19, pp. 5447–5458, 2014.

[61] U. Betz, M. K. Olsson, J. Marthy, M. Escola, and F. Atamny, "Thin films engineering of indium tin oxide: Large area flat panel displays application," *Surface and Coatings Technology*, vol. 200, no. 20-21, pp. 5751 – 5759, 2006.

[62] T. Minami, "Present status of transparent conducting oxide thin-film development for indium-tin-oxide (ito) substitutes," *Thin Solid Films*, vol. 516, no. 17, pp. 5822 – 5828, 2008. 5th International Symposium on Transparent Oxide Thin Films for Electronics and Optics.

[63] A. Andersson, N. Johansson, P. Broms, N. Yu, D. Lupo, W. R. Salaneck, *et al.*, "Fluorine tin oxide as an alternative to indium tin oxide in polymer leds," *Advanced Materials*, vol. 10, no. 11, pp. 859–863, 1998.

[64] B. Sang, K. Dairiki, A. Yamada, and M. Konagai, "High-efficiency amorphous silicon solar cells with zno as front contact," *Japanese Journal of Applied Physics*, vol. 38, no. 9R, p. 4983, 1999.

[65] Cmglee and SA, "Wikipedia."

[66] T. Kamiya, K. Nomura, M. Hirano, and H. Hosono, "Electronic structure of oxygen deficient amorphous oxide semiconductor aingazno 4x : Optical analyses and firstprinciple calculations," *physica status solidi (c)*, vol. 5, pp. 3098–3100, July 2008.

[67] C. Chen, K.-C. Cheng, E. Chagarov, and J. Kanicki, "Crystalline in-ga-zn-o density of states and energy band structure calculation using density function theory," *Japanese Journal of Applied Physics*, vol. 50, September 2011.

[68] T. Dietl, "A ten-year perspective on dilute magnetic semiconductors and oxides," *Nat Mater*, vol. 9, pp. 965–974, Dec. 2010.

[69] Y. Fukuma, H. Asada, S. Senba, and T. Koyanagi, "Epitaxial growth of diluted magnetic semiconductor ge1-xcrxte with high cr composition," *Applied Physics Letters*, February 2016.

[70] T. Fukumura, H. Toyosaki, and Y. Yamada, "Magnetic oxide semiconductors," *Semiconductor Science and Technology*, vol. 20, no. 4, p. S103, 2005.

[71] R. Levy and R. Hasegawa, *Amorphous Magnetism II*. 1977.

[72] H. Hooper and A. de Graaf, *Amorphous Magnetism : Proceedings of the International Symposium on Amorphous Magnetism*. 1973.

[73] T. Story, R. R. Galazka, R. B. Frankel, and P. A. Wolff, "Carrier-concentration -induced ferromagnetism in pbsnmnte," *Phys. Rev. Lett.*, vol. 56, pp. 777–779, Feb 1986.

[74] H. Ohno, H. Munekata, T. Penney, S. von Molnár, and L. L. Chang, "Magnetotransport properties of p -type (in,mn)as diluted magnetic iii-v semiconductors," *Phys. Rev. Lett.*, vol. 68, pp. 2664–2667, Apr 1992.

[75] S. Riester, I. Stolichnov, H. Trodahl, N. Setter, A. Rushforth, K. Edmonds, R. Campion, C. Foxon, B. Gallagher, and T. Jungwirth, "Toward a low-voltage multiferroic transistor: Magnetic (ga, mn) as under ferroelectric control," *Applied Physics Letters*, vol. 94, no. 6, p. 063504, 2009.

[76] Y. F. Lee, F. Wu, R. Kumar, F. Hunte, J. Schwartz, and J. Narayan, "Epitaxial integration of dilute magnetic semiconductor sr3sno with si (001)," *Applied Physics Letters*, vol. 103, no. 11, 2013.

[77] C. C. Wang, B. Y. Man, M. Liu, C. S. Chen, S. Z. Jiang, S. Y. Yang, S. C. Xu, X. G. Gao, and B. Hu, "The intrinsic room-temperature ferromagnetism in zno:co thin films deposited by pld," *Advances in Condensed Matter Physics*, vol. 2012, 2012.

[78] G. S. Parkinson, "Iron oxide surfaces," *Surface Science Reports*, vol. 71, no. 1, pp. 272 – 365, 2016.

[79] B. Klahr, S. Gimenez, F. Fabregat-Santiago, J. Bisquert, and T. W. Hamann, "Electrochemical and photoelectrochemical investigation of water oxidation with hematite electrodes," *ENERGY & ENVIRONMENTAL SCIENCE*, vol. 5, pp. 7626–7636, JUN 2012.

[80] K. Sivula, F. Le Formal, and M. Gratzel, "Solar water splitting: progress using hematite alpha-fe2o3 photoelectrodes," *ChemSusChem*, vol. 4, no. 4, pp. 432–449, 2011.

[81] K. M. Rosso, D. M. A. Smith, and M. Dupuis, "An ab initio model of electron transport in hematite (α-Fe_2O_3) basal planes," *The Journal of Chemical Physics*, vol. 118, pp. 6455–6466, 2003.

[82] D. Beydoun, R. Amal, G. Low, and S. McEvoy, "Occurrence and prevention of photodissolution at the phase junction of magnetite and titanium dioxide," *Journal of Molecular Catalysis A: Chemical*, vol. 180, no. 1, pp. 193 – 200, 2002.

[83] Y. Mei, Z. J. Zhou, and H. L. Luo, "Electrical resistivity of rf sputtered iron oxide thin films," *Journal of Applied Physics*, vol. 61, pp. 4388–4389, April 1987.

[84] M. Fonin, Y. S. Dedkov, R. Pentcheva, U. Rüdiger, and G. Güntherodt, "Magnetite: a search for the half-metallic state," *Journal of Physics: Condensed Matter*, vol. 19, August 2007.

[85] D. Reisinger, P. Majewski, M. Opel, L. Alff, and R. Gross, "Hall effect, magnetization, and conductivity of fe3o4 epitaxial thin films," *Applied Physics Letters*, vol. 85, no. 21, pp. 4980–4982, 2004.

[86] G. Scarel and A. Svane, *Scientific and Technological Issues Related to Rare Earth Oxides: An Introduction*, vol. 106 of *Topics in Applied Physics*. Berlin, Heidelberg: Springer Berlin Heidelberg, 2007.

[87] D. Flood, "High-field magnetization of dy 2o 3," *Physics Letters A*, vol. 49, no. 1, pp. 59–60, 1974.

[88] M. A. Khan, M. Islam, M. Ishaque, and I. Rahman, "Effect of tb substitution on structural, magnetic and electrical properties of magnesium ferrites," *Ceramics International*, vol. 37, no. 7, pp. 2519 – 2526, 2011.

[89] V. Koval, I. Skorvanek, J. Durisin, G. Viola, A. Kovalcikova, P. Svec, K. Saksl, and H. Yan, "Terbium-induced phase transitions and weak ferromagnetism in multiferroic bismuth ferrite ceramics," *Journal of Materials Chemistry C*, vol. 5, pp. 2669–2685, March 2017.

[90] M. M. Waldrop, "The chips are down for moore's law," *Nature*, vol. 530, February 2016.

[91] G. Moore, "Cramming more components onto integrated circuits," *Proceedings of the IEEE*, vol. 86, pp. 82–85, January 1998.

[92] S. Kumar, "Fundamental limits to moore's law," November 2015.

[93] P. Li, C. Xia, Z. Zhu, Y. Wen, Q. Zhang, H. N. Alshareef, and X.-X. Zhang, "Ultrathin epitaxial ferromagnetic ?-fe2o3 layer as high efficiency spin filtering materials for spintronics device based on semiconductors," *Advanced Functional Materials*, vol. 26, no. 31, pp. 5679–5689, 2016.

[94] R. Ramesh and N. A. Spaldin, "Multiferroics: progress and prospects in thin films," *Nature materials*, vol. 6, no. 1, pp. 21–29, 2007.

[95] M. Fiebig, "Condensed-matter physics: Multitasking materials from atomic templates," *Nature*, vol. 537, 22 2016.

[96] N. A. Hill, "Why are there so few magnetic ferroelectrics?," *The Journal of Physical Chemistry B*, vol. 104, no. 29, pp. 6694–6709, 2000.

[97] D. Khomskii, "Trend: Classifying multiferroics: Mechanisms and effects," *Physics*, vol. 2, p. 20, 2009.

[98] M. Etier, C. Schmitz-Antoniak, S. Salamon, H. Trivedi, Y. Gao, A. Nazrabi, J. Landers, D. Gautam, M. Winterer, D. Schmitz, H. Wende, V. V. Shvartsman, and D. C. Lupascu, "Magnetoelectric coupling on multiferroic cobalt ferrite-barium titanate ceramic composites with different connectivity schemes," *Acta Materialia*, vol. 90, pp. 1 – 9, 2015.

[99] Y. Zhou, D. Deng, Z. Feng, S. Yuan, S. Cao, and J. Zhang, "Multiferroicity and magnetoelectric coupling in ferrite-ferroelectric particulate ceramics," in *2011 International Symposium on Applications of Ferroelectrics (ISAF/PFM) and 2011 International Symposium on Piezoresponse Force Microscopy and Nanoscale Phenomena in Polar Materials*, pp. 1–4, July 2011.

[100] A. Sundararaj, G. Chandrasekaran, H. A. Therese, and K. Annamalai, "Room temperature magnetoelectric coupling in bati1?xcrxo3 multiferroic thin films," *Journal of Applied Physics*, vol. 119, no. 2, p. 024107, 2016.

[101] J. T. Heron, J. L. Bosse, Q. He, Y. Gao, M. Trassin, L. Ye, J. D. Clarkson, C. Wang, J. Liu, S. Salahuddin, D. C. Ralph, D. G. Schlom, J. Íñiguez, B. D. Huey, and R. Ramesh, "Deterministic switching of ferromagnetism at room temperature using an electric field," *Nature*, vol. 516, December 2014.

[102] K. Liang, P. Zhou, Z. Ma, Y. Qi, Z. Mei, and T. Zhang, "Multiferroic magnetoelectric coupling effect of bilayer la1.2sr1.8mn2o7/pbzr0.3ti0.7o3 complex thin film," *Physics Letters A*, vol. 381, no. 17, pp. 1504 – 1509, 2017.

[103] H. M. Christen and G. Eres, "Recent advances in pulsed-laser deposition of complex oxides," *Journal of Physics: Condensed Matter*, vol. 20, no. 26, p. 264005, 2008.

[104] I. W. Boyd, "Thin film growth by pulsed laser deposition," *Ceramics International*, vol. 22, no. 5, pp. 429 – 434, 1996.

[105] http://neocera.com/products/large-area-pulsed-laser-deposition systems/, 2018.

[106] http://www.etrema.com/terfenol d/.

[107] https://angstromengineering.com/tech/electron-beam evaporation/.

[108] Z. Wang and Z. Zhang, *Electron Beam Evaporation Deposition*, pp. 33–58. Wiley-VCH Verlag GmbH & Co. KGaA, 2016.

[109] C. Platt, A. Berkowitz, D. J. Smith, and M. McCartney, "Correlation of coercivity and microstructure of thin cofe films," *Journal of Applied Physics*, vol. 88, August 2000.

[110] N. Shirato, *Morphology-properties studies in laser synthesized nanostructured materials*. PhD thesis, University of Tennessee Knoxville, 2012.

[111] E. Quandt, B. Gerlach, and K. Seemann, "Preparation and applications of magnetostrictive thin-films," *J. Appl. Phys.*, vol. 76, pp. 7000–7002, 1994.

[112] R. B. Vandover, E. M. Gyorgy, R. P. Frankenthal, M. Hong, and D. J. Siconolfi, "Effect of oxidation on the magnetic-properties of unprotected tbfe thin-films," *J. Appl. Phys.*, vol. 59, pp. 1291–1296, 1986.

[113] H. B. Lal and K. Gaur, "Electrical conduction in non-metallic rare-earth solids," *Journal of Materials Science*, vol. 23, no. 3, pp. 919–923, 1988.

[114] R.-S. Chen, C.-C. Tang, W.-C. Shen, and Y.-S. Huang, "Thickness-dependent electrical conductivities and ohmic contacts in transition metal dichalcogenides multilayers," *Nanotechnology*, vol. 25, no. 41, p. 415706, 2014.

[115] R. Khanal, D. B. Buchholz, R. P. H. Chang, and J. E. Medvedeva, "Composition-dependent structural and transport properties of amorphous transparent conducting oxides," *Physical Review B*, vol. 91, no. 20, p. 205203, 2015.

[116] F. J. Morin, "Electrical properties of (alpha-Fe_2O_3)," *Phys. Rev.*, vol. 93, pp. 1195–1199, 1954.

[117] R. Gillen, S. J. Clark, and J. Robertson, "Nature of the electronic band gap in lanthanide oxides," *Phys. Rev. B*, vol. 87, p. 125116, 2013.

[118] P. Cox, *Transition Metal Oxides: An Introduction to Their Electronic Structure and Properties*. The International series of monographs on chemistry, OUP Oxford, 2010.

[119] C. Wu, X. Li, J. Lu, Z. Ye, J. Zhang, T. Zhou, R. Sun, L. Chen, B. Lu, and X. Pan, "Characterization of amorphous si-zn-sn-o thin films and applications in thin-film transistors," *Applied Physics Letters*, vol. 103, no. 8, 2013.

[120] D. B. Buchholz, Q. Ma, D. Alducin, A. Ponce, M. Jose-Yacaman, R. Khanal, J. E. Medvedeva, and R. P. H. Chang, "The structure and properties of amorphous indium oxide," *Chemistry of Materials*, vol. 26, no. 18, pp. 5401–5411, 2014.

[121] http://www.sigmaplot.co.uk/products/peakfit/peakfit.php.

[122] A. P. Grosvenor, B. A. Kobe, M. C. Biesinger, and N. S. McIntyre, "Investigation of multiplet splitting of fe 2p xps spectra and bonding in iron compounds," *Surface and Interface Analysis*, vol. 36, no. 12, pp. 1564–1574, 2004.

[123] J. E. Castle, "The composition of metal surfaces after atmospheric exposure: An historical perspective," *The Journal of Adhesion*, vol. 84, no. 4, pp. 368–388, 2008.

[124] P. Liu, X. Liu, L. Lyu, H. Xie, H. Zhang, D. Niu, H. Huang, C. Bi, Z. Xiao, J. Huang, and Y. Gao, "Interfacial electronic structure at the ch3nh3pbi3/moox interface," *Applied Physics Letters*, vol. 106, no. 19, p. 193903, 2015.

[125] V. Nemoshkalenko, V. Uvarov, and S. Borisenko, "X-ray emission and photoelectron spectroscopy study and the electronic structure of dy1-xtbxfe2 (x = 0.0, 0.5, 1.0)," *Journal of Electron Spectroscopy and Related Phenomena*, vol. 76, pp. 641 – 646, 1995. Proceedings of the Sixth International Conference on Electron Spectroscopy.

[126] A. Y. A. Zoubi, "Determination of hall mobility of metals using a microwave resonator," *Measurement Science and Technology*, vol. 2, no. 12, p. 1165, 1991.

[127] T. Yamashita and P. Hayes, "Analysis of xps spectra of fe2+ and fe3+ ions in oxide materials," *Applied Surface Science*, vol. 254, no. 8, pp. 2441 – 2449, 2008.

[128] Y. Ogawa, D. Ando, Y. Sutou, and J. Koike, "The electrical and optical properties of fe–o–n thin films deposited by rf magnetron sputtering," *MATERIALS TRANSACTIONS*, vol. 54, no. 10, pp. 2055–2058, 2013.

[129] A. Fernandez-Pacheco, *Studies of Nanoconstrictions, Nanowires and FeO Thin Films: Electrical Conduction and Magnetic Properties. Fabrication by Focused Electron/Ion Beam*, ch. Magnetotransport Properties of Epitaxial Fe3O4 Thin Films, pp. 51–82. Berlin, Heidelberg: Springer Berlin Heidelberg, 2011.

[130] T. D. Waite, *Reviews in Mineralogy*, vol. 23. Washington, DC: Mineralogical Society of America, 1990.

[131] H. Kawazoe, M. Yasukawa, H. Hyodo, M. Kurita, *et al.*, "p-type electrical conduction in transparent thin films of cuaio2," *Nature*, vol. 389, no. 6654, p. 939, 1997.

[132] F. Xiu, Z. Yang, L. Mandalapu, D. Zhao, J. Liu, and W. Beyermann, "High-mobility sb-doped p-type zno by molecular-beam epitaxy," *Applied Physics Letters*, vol. 87, no. 15, p. 152101, 2005.

[133] B. Zeghbroeck, *Semiconductor Fundamentals*. 2011.

[134] J. Tate, H. Ju, J. Moon, A. Zakutayev, A. Richard, J. Russell, and D. McIntyre, "Origin of p-type conduction in single-crystal cualo 2," *Physical review B*, vol. 80, no. 16, p. 165206, 2009.

[135] J. Singh and K. Shimakawa, *Advances in Amorphous Semiconductors*. Advances in Condensed Matter Science, CRC Press, 2003.

[136] A. Naumkin, A. Kraut-Vass, S. Gaarenstroom, and C. Powell, "Nist standard reference database 20, version 4.1," 2012.

[137] B. I. Shklovskii, *Electronic Properties of Doped Semiconductors*. Springer Series in Solid-State Sciences, 45, 1984.

[138] N. Kishimoto and K. Morigaki, "Optical absorption and infrared photoconductivity in amorphous si–au system," *Journal of the Physical Society of Japan*, vol. 46, no. 2, pp. 497–504, 1979.

[139] van Der Putten D, Moonen, Brom, Brokken-Zijp, and Michels, "Evidence for superlocalization on a fractal network in conductive carbon-black-polymer composites," *Physical review letters*, vol. 69, July 1992.

[140] W. H. Strehlow and E. L. Cook, "Compilation of energy band gaps in elemental and binary compound semiconductors and insulators," *Journal of Physical and Chemical Reference Data*, vol. 2, no. 1, pp. 163–200, 1973.

[141] Y. Cao, M. Xiang, W. Zhao, G. Wang, Z. Feng, B. Kang, A. Stroppa, J. Zhang, W. Ren, and S. Cao, "Magnetic phase transition and giant anisotropic magnetic entropy change in tbfeo3 single crystal," *Journal of Applied Physics*, vol. 119, February 2016.

[142] L. R. Dedon, S. Saremi, Z. Chen, A. R. Damodaran, B. A. Apgar, R. Gao, and L. W. Martin, "Non-stoichiometry, structure, and properties of bifeo3 films," *Chemistry of Materials*, vol. 28, no. 16, pp. 5952–5961, 2016.

[143] N. D. Scarisoreanu, F. Craciun, R. Birjega, V. Ion, V. S. Teodorescu, C. Ghica, R. Negrea, and M. Dinescu, "Joining chemical pressure and epitaxial strain to yield y-doped bifeo thin films with high dielectric response," *Scientific Reports*, vol. 6, no. 1, pp. 25535–25535, 2016.

[144] J.-W. Yoo, H. Jang, V. Prigodin, C. Kao, C. Eom, and A. Epstein, "Tunneling vs. giant magnetoresistance in organic spin valve," *Synthetic Metals*, vol. 160, no. 3, pp. 216 – 222, 2010. Spins in Organic Semiconductors 2009, Salt Lake City, Utah, February 4-7.

[145] B. Prasad, W. Zhang, J. Jian, H. Wang, and M. G. Blamire, "Strongly bias?dependent tunnel magnetoresistance in manganite spin filter tunnel junctions," *Advanced Materials*, vol. 27, pp. 3079–3084, May 2015.

[146] A. Sundararaj, G. Chandrasekaran, H. A. Therese, and K. Annamalai, "Charge mediated room temperature magnetoelectric coupling in zn 1? x sm x o/batio 3 bilayer thin film," *Nanotechnology*, vol. 26, August 2015.

[147] Z. Ning, Y. Xiao-Ming, W. Miao, S. T., and S. G., "Magnetoelectric coupling in bilayers of pb(zr, ti)o 3 epoxy and hot pressed manganite perovskite," *Chinese Physics Letters*, vol. 23, no. 2, p. 463, 2006.

Vita

Humaira Taz was born in Sirajganj, Bangladesh, on August 5th, 1990, the daughter of Mrs. Shadhina Khatun and Mr. Nurtaz Ali. She received degree for Bachelor of Arts in Applied Mathematical Sciences from Wesleyan College, Macon, GA USA in the year 2013. In the Fall of 2013, she joined the doctoral program in Bredesen Center at University of Tennessee Knoxville. She pursued her PhD under the supervision of Dr. Ramki Kalyanaraman.